MICRO FUEL CELLS AND NANOSCALE COLLOIDAL SEPARATION SYSTEMS: DESIGN, FABRICATION, AND CHARACTERIZATION

BY

EAKKACHAI PENGWANG

DISSERTATION

Submitted in partial fulfillment of the requirements
for the degree of Doctor of Philosophy in Mechanical Engineering
in the Graduate College of the
University of Illinois at Urbana-Champaign, 2011

Urbana, Illinois

Doctoral Committee:

Professor Narayana R. Aluru, Chair
Professor Mark A. Shannon, Director of Research
Professor Placid M. Ferreira
Assistant Professor David Saintillan
Assistant Professor Gang Logan Li

ABSTRACT

This thesis presents different types of membranes fabricated by microfabrication processes for applications on micro fuel cell, proton exchange membrane, and removal process of nanoscale colloids. First, the development of a millimeter-scale fuel cell with on-board fuel is enabled by implementing a passive control mechanism and porous silicon for residual filtration. The regulating membrane can control a delivery of water into a chamber of chemical hydride by the internal pressure in the hydride chamber. Consequently, the generated hydrogen exits to the Nafion-based Membrane Electrode Assembly (MEA) through the porous silicon membrane at the bottom of the hydride chamber. Within a total volume of 9 μL, which makes it the smallest fully integrated fuel cell reported in the literature, these devices deliver an energy density of ~250 Wh/L. Tentative applications for this device are microelectronics, microsystems, and micro robots. Another membrane development in this study is a silicon-based Proton Exchange Membrane (PEM) with self-assembly molecules. After anodization processes of a 20 μm thick silicon membrane in a hydrofluoric (HF) solution, techniques for self-assembly of molecules with sulfonate (SO_3H) functional groups within extremely high aspect ratio silicon nanopores are examined. The set up was used to continuously extract solvent to functionalize a porous membrane with pore sizes of ~5-10 nm. The assembled molecule is 3-mercaptopropyl-trimethoxysilane (MPTMS). Then, the thiol end group of the MPTMS molecule was subsequently oxidized to sulfonate group to enhance proton transport through the pores. Penetration of the MPTMS molecules down to the bottom of the pores was verified through characterizing the membrane thickness by using Time of Flight-Secondary Ion Mass Spectroscopy (ToF-SIMS) and X-ray

Photoemission Spectroscopy (XPS), as well as the water desorption isotherm technique. These porous silicon membranes can influence developments of proton exchange membrane, self-assembled layer deposition, and micro fuel cells. Last, the possibility of Electrokinetics-based device with alternating current (AC) traveling waveform membrane is validated for the applications of water purification and colloidal removal. The development of the membrane is simulated by engineering software. The membrane is nanostructured with embedded electrodes that are connected with different spatial phase of AC voltage supplies. The testing of fabricated membranes shows a concentration of colloids with ~25% removal efficiency of 93 nm fluorescent latex colloids across the membrane. With a possibility of pumping particles into another chamber, this traveling wave membrane can be an alternative for a colloidal separation in microfluidic systems.

To my family, my advisor, and friends

ACKNOWLEDGMENTS

This project would not have been possible without the support of many people. First of all, I would like to sincerely thank my advisor, Prof. Mark. A. Shannon for his advice, generous discussion, and support throughout my study at the University of Illinois at Urbana-Champaign (UIUC). Special thanks are also due to Assistant Prof. Saeed Moghaddam (recently at University of Florida) for supervising my projects during his post-doc position at the University of Illinois. I am also appreciated help from Prof. Narayana R. ALuru and Prof. Richard I. Masel for valuable discussions and support through my research study. I also gratefully acknowledge Dr. Glennys Mensing and Dr. Bruce Flachsbart for their assistance, suggestion, and help especially for microfabrication processes.

I am appreciated financial supports for this micro power system research funded by the Defense Advanced Research Projects Agency (DARPA) under grant DST 2007-0299513-000-1. Another financial support for an alternating current electrokinetic-based device was partially supported by the Center of Advanced Materials for the Purification of Water with Systems (WaterCAMPWS) under the National Science Foundation and the US Army Research, Development, and Engineering Command Acquisition Center (RDECOM ACQ CTR) through award number W911NF-09-C-0079. Also, part of these projects was carried out in the Frederick Seitz Materials Research Laboratory Central Facilities, University of Illinois, which are partially supported by the U.S. Department of Energy under grants DE-FG02-07ER46453 and DE-FG02- 07ER46471.

I also would like to thank all of my friends at the Department of Mechanical Science and Engineering for their helps, suggestions, and friendship during my study. Thanks all of my friends and labmates for discussions and helps during my study, especially to Vikhram Vilasur Swaminathan, Dr. Junghoon Yeom, Andrea Vozar, Dr. Likun Zhu, Dr. Byunghoon Bae, Ki Sung Lee, Adam Sawyer, Yaofeng Chen, Miki Takagi, Huan Hu, Ahmad Qadi, Shama Farabi, Mayank Behl, Dr. Yan Wu, Demana Agonafer, Ali Ashraf, Cody Jensen, and Xiaozhong Jin. I wish them a success in school, career and life. I also would like to thank all of my friends in Champaign and Urbana for their encouragement, helps, and friendship. Thanks to Thai Student Organization (TSA) at UIUC for giving me a great opportunity to meet their members and become friends with those who share similar goals. Thanks for all my friends who bring good food, games, and fun to my life. It is too long to list your name here, but I will not get this far without you. Thanks. I would like to thank my friends in Thailand, especially my old friends from Bunyawat Witthayalai School in Lampang. Special thanks for all of my best friends from Thai Scholar'43 program and the University of Wisconsin-Madison. Even it is hard to keep in touch with them, I am always appreciated their love and encouragement throughout the time that I am growing up.

Finally, I would like to take this opportunity to express my deepest gratitude's to my parents, my younger sister, and the rest of my extended family for their understanding, inspiration, love, encouragement, and support since I was born. Their attitudes towards life are always valuable for me. Thank you very much. Thanks everybody to be a part of my Ph.D. study. Thank you for everything.

TABLE OF CONTENTS

Page

CHAPTER 1:

INTRODUCTION

1.1. Membrane Technologies

1.1.1. Membranes

A membrane is a layer of material that can serve as a semipermeable barrier for certain substances. Some particles are impermeable through the thin membrane, while the other can pass through. Examples of processes related to synthetic membranes are reverse osmosis, dehydrogenation, water purification, gas purification, and removal of microorganisms. Membranes can be fabricated from organic, inorganic, and biological materials. They can also be categorized into several classifications based on structure, production method, chemistry, functionality, driving force, flow configuration, pore size, pore geometry, cost, and lifetime. Relationships between common membrane separation processes, pore diameter, and size of permeates are listed in Figure 1.1.

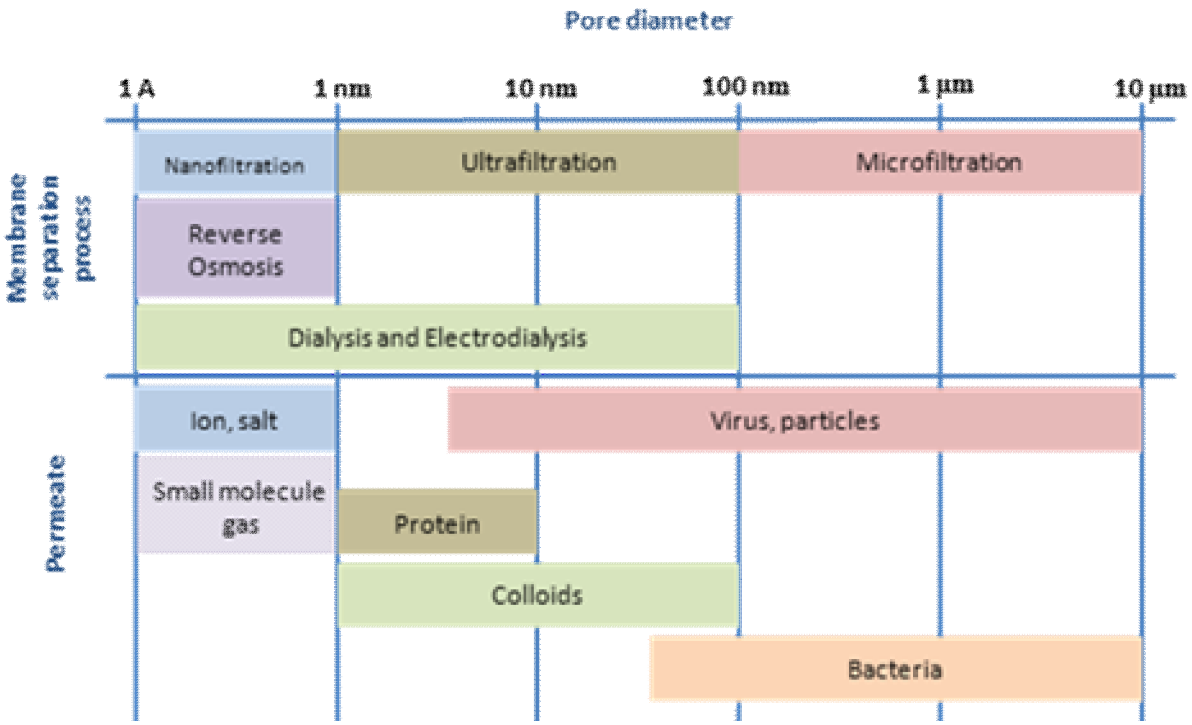

Figure 1.1. Figure of merit shows relationships between pore size of the membrane, membrane separation process, and their applications

1.1.2. Objective

The main overall purpose of this project is to implement micro- and nanofabrication to develop membranes used for Microelectromechanical systems (MEMS). Even length scales of permeates are different, this study focuses on membranes for energy and water applications. First, the membranes for a passive water delivery system and membrane for filter small molecule residuals from the hydride reaction that can enhance a development of millimeter-scale fuel cells are studied. Moreover, the proton exchange membranes were investigated from a porous silicon material and sulfonate functional group. This type of inorganic and organic membrane can be alternative for recent commercial polymeric membrane because it has an outstanding mechanical property to resist to deformation. Last, a

design of water purification membrane with an alternating current electrodialysis (ACED) membrane was examined. The membrane is constructed by multiple electrodes that are supplied with different phase of AC voltage. Simulations are also implemented to design traveling waveform schemes and to anticipate some testing results. This type of membranes is aimed for facilitation of nanoscale colloidal separation in microfluidic devices. These membranes are widely different for certain applications, in term of their development, functionality, mechanism, and science. Therefore, detailed fabrications and discussions are provided separately.

1.2. Micro Fuel Cells

1.2.1. Overview

Energy consumption has increased dramatically during the past decades in order to functionalize electrical appliances, provide heat sources, generate light sources, and communicate in daily routine. With breakthroughs in technological developments, these electrical needs are intensified. Researches and study aimed to reduce energy consumption, generate alternative renewable energy, and plan for recent reserved energy sources are diversified over variety ranges. One of the most interesting prospective of energy generation is to generate electrical energy from a chemical energy in a fuel.

1.2.2. Fuel Cells

Initiated in 1839, Sir William Grove invented the first electro chemical cells that can convert this chemical energy to electrical energy. Followed by this experiment, several researches have focused on developing fuel cells for better performance, higher efficiencies,

lower cost, and more environmental friendliness. Several advantages of fuel cell are claimed as follows;

1) More efficiency than combustion engines
2) No moving parts
3) Quite operation
4) Highly reliable
5) Long-lasting systems
6) No particular NO_x and SO_x emission

1.2.3. Fuel Energy Density

Several fuels can be used directly and indirectly for fuel cell technologies. The direct fuel cells are the cells that a fuel is directly contact the membrane to produce energy. The indirect fuel cells are the cells that implement a reformer to convert a chemical component into simple elements before feeding into the membrane. Compared to hydrocarbon fuels and recent batteries, common fuels that can be used in the fuel cell are listed in the following table.

Table 1.1. Fuel energy density (not including external components)

Storage Type	Specific energy density [W h/L]
Natural gas	10.1
Hydrogen, liquid	2500
Hydrogen, gas at 700 bar	1555.1
Gasoline	9497.3
Methanol	4332.1
Ethanol	6664.8
Lead acid battery	80
Nickel metal hydride	200
Zinc-air battery	260
Lithium ion battery	100 – 800
Lithium Borohydride	11663.4

1.2.4. Applications for Fuel Cells

As an alternation for power generation, fuel cells are studies for different applications. The applications of power sources depend on size, power density, and energy density of fuel cells. For instance, the applications for fuel cells are stationary power generator, portable power sources (such as cell phones and notebooks), medical devices, military applications, micro devices, and microsystems.

1.2.5. Fuel Cells Components

An ideal reaction of fuel cells and batteries are similar. However, many researches differentiate batteries from fuel cells in a sense that both reactants on cathode and anode reaction are packed together in batteries, while fuel cells can use external sources, for example, replaceable hydrogen gas tanks. Also, a partial component of oxygen in air can be used in H_2-O_2 fuel cells.

A schematic design of a simple fuel cell consists of a conducting electrolyte membrane and two electrodes for electrochemical half reaction of oxidation and reduction. In a majority of operations, catalysts are implemented to both electrodes to enhance a cell reaction. An example of H_2-O_2 fuel cells consists of two platinum electrodes dipped into sulfuric acid (an aqueous acid electrolyte). When hydrogen is introduced across an electrode, it is split into protons (H^+) and electrons. This reaction is referred to as a hydrogen oxidation which occurs at the anode side where electrons are removed from a specie. Consequently, the protons can flow through the electrolyte which allows only protons to pass, and the electrons flow into the external electrical circuit through a piece of wire that connects to the opposite electrode. When an electron is at the other electrode, it is combined with protons and

supplied oxygen to generate a product of water. This chemical reaction is called oxygen reduction at the cathode side where electrons are added to a specie. The schematic diagram for common fuel cell is shown in Figure 1.2.

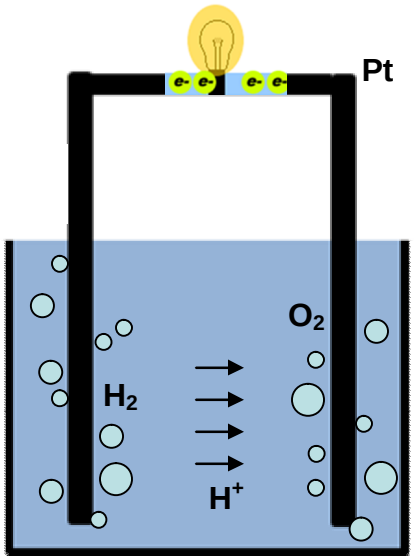

Figure 1.2. Schematics diagram for fuel cell

Many categories of fuel cells are characterized based on their electrolytes, fuel sources, temperature ranges, and flow types. However, the most straightforward divisions differentiate them by considering their electrolytes and charge carriers. This can separate fuel cells into five major groups: phosphoric acid fuel cell (PAFC), polymer electrolyte membrane fuel cell (PEMFC), alkaline fuel cell (AFC), molten carbonate fuel cell (MCFC), and solid-oxide fuel cell (SOFC).

1.2.6. Proton Exchange Membranes Fuel Cells

Proton exchange membrane fuel cells (PEMFCs) are attractive for many applications because they operate at low temperatures, compared to the other type of fuel cells. The

operating temperature of PEMFCs can be widely ranged from room temperature to a few hundred degrees Celsius. A common electrolyte for PEMFCs is a thin polymer membrane that can transport proton as an ionic charge carrier. The thickness of the membranes is in the range of a few microns and a few hundreds microns. The common materials for proton exchange membranes are sulfulnated polymers that will selectively allow only proton to pass through. While the electrons are emitted and collected at the current collectors, it is passed to electrical circuit to external loads and collected again on the other side of the membrane.

Catalysts are always implemented to improve the performance of typical PEMFCs within choices of precious materials, for example, platinum (Pt), ruthenium (Ru), Palladium (Pd). Moreover, gas diffusion layers (GDLs) are implemented to provide a uniform distribution of fuel to a contact of the catalysts. The schematics for proton exchange membrane fuel cells (PEMFCs) are shown in Figure 1.3.

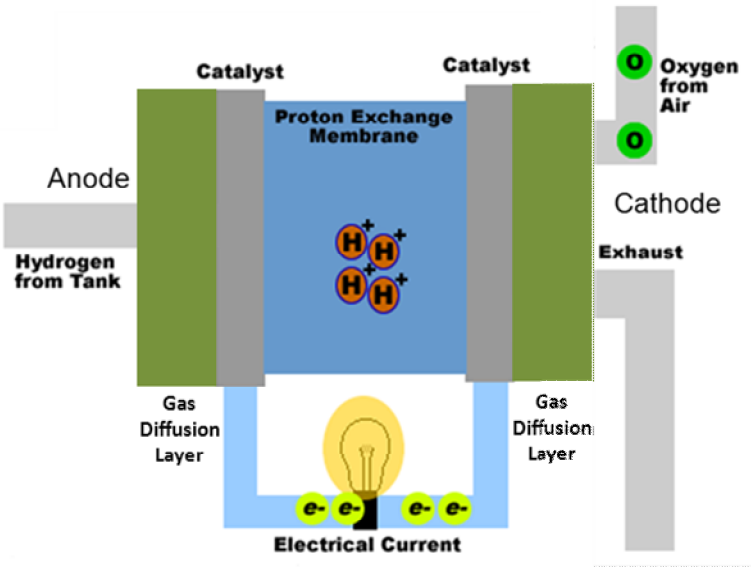

Figure 1.3. Schematics of proton exchange membrane fuel cells (PEMFCs)

1.2.7. PEMFC Developments

Many researchers study the development of the proton exchange membranes and the membrane electrode assembly (MEAs) to improve the efficiency and power density of the fuel cells. The common methods include modifying of the membranes, optimizing the parameters for operations, discovering new membranes, etc. The parameters in operations are temperatures, humidity, catalyst loading, catalyst preparations, shapes of gas diffusion layers, cathode backing pressure, operating voltages, fuel types, membrane thickness, membrane preparation, etc. The main goal is to perform better at required conditions for different applications.

1.2.8. Performance Characterizations

Generally, the cell performances of fuel cells involve four major losses in electrochemical reaction; reactant transport, electrochemical reaction, ionic and electronic conduction, and product removal. An actual current output of a fuel cell is measured by applying a load into the system. A typical current-voltage relationship is a curve that starts at the open cell voltage (OCV) when a potential of the cell is maximum and the current is zero or no current is drawn to external circuit. The values of current are then increased when electrons are allowed to pass through the circuit when the voltage is reduced. Typically, a fuel cell encounters a mass transport limit at the maximum value of the current and the potential difference between the two electrodes is reduced to zero. These components of voltage drop from ideal (thermodynamic) fuel cell voltage are resulted from various components: activation loss due to electrochemical reaction, ohmic loss due to ionic and electronic conduction in the membrane, and concentration limit due to mass transport. In this

characterization, a Solartron SI 1287 potentiostat was commonly used to conduct the performance tests. With a linear sweep voltammetry, the testing components were installed in a test stand with anode and cathode electrodes connected to the potentiostat. The potentiostat will record amounts of voltage at different drawing currents. Moreover, the lifetime test of the fuel cells can be examined using this configuration.

1.2.9. Scope of the Study

In this document, recent developments focused on micro fuel cells that the membrane electrode assembly has a size of a millimeter scale (less than 5 millimeter) are investigated. Readers will find this document useful for a progressive and concise report on development of micro fuel cells to replace a battery in many aspects. In Chapter 1, readers will acquire with general information on fuel cells chemistry, components, reactions, especially for proton exchange membrane fuel cells. In Chapter 2 and 3, previous researches on micro fuel cells are mentioned to discuss main challenges, potential applications, scopes of this research, and this approaches. The developments in micro fuel cells for this project are reported for a millimeter-scale micro fuel cell with onboard hydrogen sources and controllable operation. The schematic and parametric study of each component is studied from generation to generation.

In Chapter 4, a nanoporous silicon proton conducting membrane is characterized for a H_2-O_2 fuel cell. A method of fabrication and functionalization of a nanoporous silicon membrane is investigated for alternative of proton exchange membranes (PEMs). This membrane development can provide mechanically and thermally stable PEMs. The approach is also to covalently bond molecules with functional groups inside silicon nanopores.

Through the assembly of functional groups within a porous solid structure, this membrane technology can enable development of the next generation membrane electrode assembly (MEAs) with enhanced performance, lifetime, and reliability. With these nanoporous channels and atomic layer deposition of metals, as a result, high level performance of a H_2-O_2 fuel cells are demonstrated for various humidity conditions.

1.3. Colloidal Separation

1.3.1. Overview

A colloidal system consists of a dispersed phase and a continuous phase. In this study, we focused on a solid phase in liquid. The size of colloids can range from 10 nm to 500 nm in general. The concentrations of colloids are various depended on water sources. Typically, membrane technology is also used in filtration and water purification process, for example, microfiltration, reverse osmosis, and electrodialysis as shown in Figure 1.1. Examples of these membranes include microfiltration membrane, ultrafiltration membrane, nanofiltration membrane, and reverse osmosis membrane. The principle of these membranes is porous structure that can filter residuals and provide clean water. However, a crucial challenge is an irreversible fouling of the membrane during operation period. With a collection of colloids in the filtration system, caking and blocking of water path can result to lower efficiency and high energy cost as well.

In this study, microfluidic devices with a traveling electrode membrane are developed for a purpose of colloidal separations with a particle size in nanoscale. An alternating current (AC) electrokinetic technique is implemented to create non-uniform electric field with spatial phase variation to manipulate colloidal transportation. The range of colloids that we are interested for our preliminary testing is ~100 nanometers in diameter in water medium.

Engineering design rules and simulation tools are implemented in this project to forecast separation of colloids using a traveling waveform on dielectric and charged particles. Development of membrane and fabrication processes will be discussed in this study.

1.3.2. Particle Transportations

The mathematic model for charged particles transport involves a set of equations governing ionic transport, electric potential, fluid flow, and particle motions. The total flux of the i^{th} species (ion) is given by the following expression, where F is the Faraday's constant, z_i is the valence, D_i is the diffusion coefficient, Ω_i is the ionic mobility, $\mathbf{\Gamma}_i$ is the flux, c_i is the concentration of the ith species, $\mathbf{u}$ is the velocity vector of the fluid flow, and Φ is the electrical potential. The three terms on the right-hand side of Equation 1 define the fluxes due to diffusion, electromigration, and convection, respectively. The Nernst-Planck (NP) equation describes the transfer of each dissolved species and is given by Equation 2.

$$\mathbf{\Gamma}_i = -D_i \nabla c_i - \Omega_i z_i F c_i \nabla \Phi + c_i \mathbf{u} \tag{1}$$

$$\frac{\partial c_i}{\partial t} = -\nabla \cdot \mathbf{\Gamma}_i \tag{2}$$

The electrical potential distribution is governed by the Poisson equation as shown in Equation 3, where ε_0 is the permittivity of vacuum, ε_r is the relative permittivity.

$$\nabla \bullet (\varepsilon_r \nabla \Phi) = -\frac{F \sum z_i c_i}{\varepsilon_0} \tag{3}$$

1.3.3. Preliminary Results

The first generation of the device is based on microchannel devices with embedded planar electrodes. From observations, there was no significant particle transport that shows in testing. While it was established that asymmetric biasing could preferentially move surface charged particles, based on the fact that the momentum transfer in one direction under the

electric field is greater than in the reverse as we switch pulses. The colloids in the bulk of the microchannel experienced only a mild electric field. Owing to the aspect ratio of deep channels, the electric field was focused largely in-plane and did not act upon colloids that are suspended in the out-of-plane region.

In the second efforts, we are developing a separation scheme that attracts charged colloids, and transports them using traveling wave electric fields using a membrane/electrode stacks. The state-of-art to prove a concept of travelling wave electric fields was tested on an assembly of metal mesh and filter membrane. The metal mesh was stainless steel is 100 um in thickness and 35 um in pore size. The polycarbonate track etching (PCTE) membrane was 10 um in thickness and 3 um in pore size. The chamber and the test-set-up are presented in Figure 1.4.

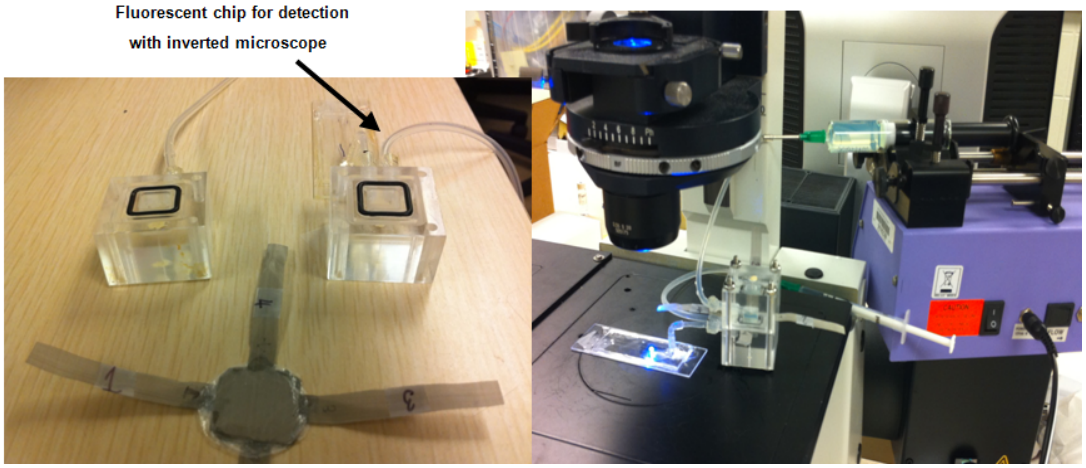

(a) (b)

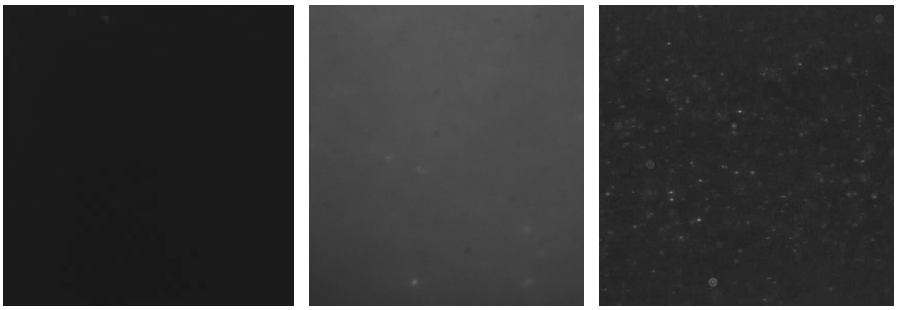

(c) (d) (e)

Figure 1.4. Chamber for holding multi-electrode (a), the test set-up (b), a fluorescent image of the clean stream before supplying voltages (c), after supplying voltages (d), and fluorescent image of the feed stream (e).

The assembly was tested with different frequencies with feed stream of 93 nm polystyrene particles of 500 ppm concentration on one side of the chamber and the clean stream on the other side. According to the test, a colloid was observed at the clean stream when the traveling waveform was supplied to each electrode. However, there was no difference in the stream of the clean stream as output when we changed the frequency as the

theories predicted. Also, after turning off the voltage supply, the fluorescent colloidal particles were still observed in the fluorescent chip.

1.3.4. Scope of the Study

In order to gain benefits from a smaller scale and prevent a leakage from the previous design, we further study the transportation of colloid in the MEMS-based-travelling membrane. Details of development and fabrication are discussed in Chapter 5. With a path of fluidic channels across traveling electrode arrays, spatial phase variation is able to induce a motion of colloids from a feed stream to a clean stream. To summarize a scope of alternating current-based device for nanoscale colloidal separation, there are three main masks to be completed as follows;

- Device fabrication work will focus on assembling test devices along with fluorescent detection chips. Further work would entail beginning preliminary colloid transport tests.
- Computational work will study the particles behavior at different excitation signals and refine the model to account for other effects within and close to a nanopore.

CHAPTER 2:

MICRO FUEL CELLS WITH ON-BOARD HYDROGEN SOURCE AND SELF-REGULATING CONTROL

2.1. Introduction

The need for better energy storage has been widely recognized in applications not only for large scale systems but also micro-devices [1-3]. Developments of a viable high energy density millimeter-scale fuel cell can enhance the portable electronics technology and enable next-generation MEMS devices (e.g., sensors and actuators) with integrated power sources. As better and/or faster devices, new technologies are being introduced with limitations of the existing power sources [4]. Although in some applications increasing functionality has been met by improvements in battery technology or reasonable reduction in time between charges, there are emerging applications (e.g. intelligent insect-sized robots, cognitive arthropods, and smart dust) [5-9] that demand far more powerful and smaller (microliterscale) energy sources than those that exist today. Moreover, micro fuel cell (MFC) technology that has been under development for some time [10-15] has the potential to bridge this power gap. The energy density of fuels (as shown in Table 2.1) used in MFCs can exceed that of batteries by an order of magnitude. Choices of fuels for metal hydrides for micro fuel cells, compared to recent batteries are also shown in Figure 2.1.

The content in this chapter is adapted from the published articles as follows;

- S. Moghaddam, E. Pengwang, K. Lin, R.I. Masel, and M.A. Shannon, "Millimeter-scale Fuel Cell with On-Board Fuel and Passive Control System," *Journal of Microelectromechanical Systems (JMEMS)*, vol. 17(6), pp. 1388-1395, 2008.
- S. Moghaddam, E. Pengwang, R.I. Masel, and M.A. Shannon, "A Self-Regulating Hydrogen Generator for Micro Fuel Cells," *Journal of Power Sources*, vol. 185, pp. 445-450, 2008.

Table 2.1: Energy density of different fuels.

Fuel	Energy density (kWh/kg)
$LiAlH_4+4H_2O$	2.4
Methanol	5.5
Most liquid hydrocarbons	~12.4
Hydrogen gas	33.2

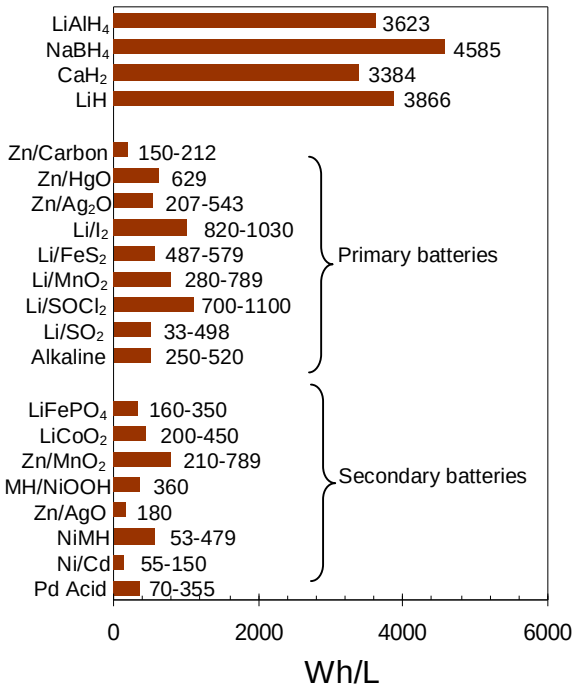

Figure 2.1. Comparison of the energy density of metal hydrides (operation voltage of 0.7 V is assumed in calculations) with different batteries.

2.2. Literature Reviews

The increasing demand for high energy density power sources driven by advancements in portable electronics and MEMS devices has generated significant interest in development of micro fuel cells and batteries [12, 16]. Micro fuel cells, however, can potentially outperform the batteries only if their fuel to device volume ratio can be maximized and the power consumption of their auxiliary systems to regulate fuel delivery and power output is significantly reduced. The micro fuel cell architectures proposed in the literature [17-20] are the scaled-downed versions of large-scale systems with numerous auxiliary components. Although microfabrication of these components (e.g., microvalves [21-36], micropumps [37-45], sensors, distribution components, power supply, and control electronics for these components) has been reported in the literature, their integration into a millimeter-scale device has remained a major challenge [46-51]. While this might be somewhat feasible in centimeter-scale fuel cells, fitting all the auxiliary components within a few cubic millimeters volume is quite a challenge.

Auxiliary components for micro fuel cells operation normally require numerous microfabrication steps and have integration difficulties that can result in higher production costs and added complexity. Examples of fuel delivery and control systems can be found in [52-57]. Sarata et al. [52] proposed a pressure-based control system for a hydrogen generator comprising of a hydride reactor and water for hydrolysis. The hydrogen generation rate is controlled by monitoring the reactor pressure and then stopping the pumping of water to the hydride chamber when the hydride chamber pressure increases above a reference value. The pressure sensor, pump, valve, and electronics to conduct this control operation occupy significant space, which directly translate to lower energy density and high cost for micro

fuel cells. In another approach [57], the pressure increase in a macro-scale hydride chamber was used to automatically push the water out of a conduit that connected the water reservoir to the hydride reactor (as shown in Figure 2.2). This results in an increase in the diffusion length between the water front and the hydride and consequently a reduction of the hydrogen generation rate. This passive approach may be more suitable for miniaturization (e.g. fabrication of a microchannel between the water and hydride reservoirs and so on) but, unfortunately, since water diffusion and thereby hydrogen generation is not completely stopped, pressure continues to rise such that failure can occur. Furthermore, the movements of the water front inside the microchannel (i.e. dynamics of the advancing and receding contact lines) and the pressure of the excess hydrogen inside the device that pushes against the water front can be complicated to predict and control.

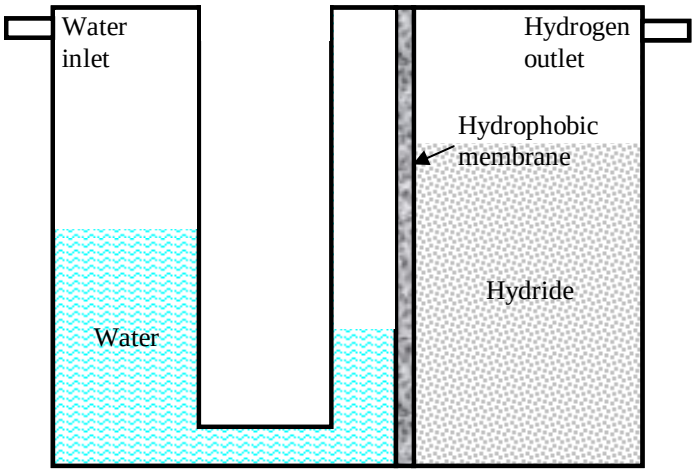

Figure 2.2. Schematic diagram of an existing control scheme. Hydrogen pressure buildup forces water away from the hydrophobic membrane and reduces water vapor diffusion into hydride chamber.

Although numerous studies have been conducted on the development of micro fuel cells, there are still a whole host of technical challenges that must be overcome to make millimeter-scale fuel cells a reality. At the heart of these issues is the architectural complexity of the MFC's that has lead to fabrication, operation, reliability, size, and cost issues.

In summary, typical auxiliary components in a micro fuel cell normally require numerous microfabrication steps, have integration difficulties, and require external electronics. These components result in high production costs and complexity of operation. Due to their relative size to membrane electrode assembly, the overall device energy density is greatly reduced. In addition, the auxiliary components can consume some of the generated power by the device, which for a millimeter-scale device can be a great portion of the entire device power. Developing a new means of fuel delivery and control that can be scaled downed and consume little to no power opens an opportunity for fabricating millimeter-scale fuel cells and realizing new devices that are tied to the existence of such power sources.

To enable development of viable millimeter-scale fuel cells, the following fundamental approaches should be taken.

1) An on-board supply for hydrogen generator is investigated in millimeter-scale.

2) Alternative and scalable means for micro-fuel-cell control should be introduced.

3) Power consumption of the auxiliary components must be minimized.

4) Microfabrication steps, complexity, and production costs should be reduced.

2.3. Selections of Hydrogen Sources

In the following sections, adequacy of the three hydrogen sources mentioned earlier for the millimeter-scale fuel cell of this study is discussed.

A. Hydrogen Storage Medium

The two main means of storing hydrogen currently being researched in literature are storage in carbon nanotubes and metallic and intermetallic compounds (as shown in Table 2.2). The storage capacity and the release temperature and pressure of different hydrogen storage media are the main factors limiting their application. Many experimental studies on different carbon nanotubes [58-64] and nanostructured carbon samples [65] have suggested a hydrogen storage capacity of up to 1.5 mass% (a review of these studies can be found in [66]). Züttel et al. [67] have suggested that charging carbon nanotubes (with hydrogen at liquid nitrogen temperature or cathodically at ambient conditions) is limited to 2 mass%, since the amount of adsorbed hydrogen is proportional to the specific surface area of the carbon nanotube.

Table 2.2: Hydrogen content of different storage means.

Hydrogen source	Weight % of hydrogen
Carbon nanotube	< 2
$PdH_{0.6}$	0.56
Mg_2NiH_4	3.59
$LiNH_2BH_3$	10.6
CH_4	25
C_4H_{10}	17.2
C_8H_{18}	15.8
CaH_2	9.6
$NaBH_4$	21.3
$LiAlH_4$	21.2
$LiBH_4$	37.0

The second approach is the use of condensed-phase hydride materials. Many elemental metals form hydrides (e.g., $PdH_{0.6}$), but none at an attractive temperature and pressure range for MEMS applications. Fortunately, the discovery of hydrogen sorption by intermetallic compounds at reasonable temperatures and pressures has created great hope for hydrogen storage close to ambient conditions (a list of these compounds can be found in [68]). Some of these compounds also release unwanted by-products during dehydrogenation process. In a recent study, Xiong et al. [69] showed that more than 10% of hydrogen desorbs from lithium amidoborane ($LiNH_2BH_3$) at a temperature of around 90°C (without the by-product borazine typical of dehydrogenation process of ammonia borane, NH_3BH_3, compounds).

B. Fuel Reformers

Hydrocarbon fuel and organic solvents are also rich sources of hydrogen. However, unfortunately, hydrogen extraction from them is quite energy and process intensive. The reforming process is often involved in relatively high operation temperatures (in the range of 300°C–700°C). In a millimeter scale silicon-based device, isolating the heat source from the rest of the device (particularly the MEA) is quite a challenge. More importantly, the heating system and other necessary auxiliary elements often required in a typical reformer (pump, sensors, distribution components, control system, power source/conditioning for heater, and means for separating hydrogen from other reaction products) are challenging to fit into a millimeter-scale device without significant sacrifices in fuel volume.

C. Decomposable Hydrides

Hydrogen generation through hydrolysis of a metal hydride (such as LiH, $LiBH_4$, $LiAlH_4$, and CaH_2) is a rather simple process that generates clean hydrogen. An example of this type of reaction is $LiAlH_4$ reaction with water as follows;

$$H_2O + 0.25\ LiAlH_4 \rightarrow 0.25\ LiOH + 0.25\ Al(OH)_3 + H_2$$

These hydrides are great sources of hydrogen. For example, in the above reaction, 1 mole of hydrogen is generated for every 1.25 moles of reactants. Hydrogen production by hydrolysis of hydrides is advantageous with respect to operation at low temperature and pressure. Provided a means for water delivery to the hydride, the hydrogen generation rate and its delivery to the MEA could be readily controlled. Moreover, these hydrides have a high rate of reaction with water vapor, which has been the key factor in designing a passive control technique for hydrogen generation, as discussed in the following section.

Proton Exchange Membrane Fuel Cells (PEMFCs) require relatively pure hydrogen to operate. Hydrogen can be supplied by a hydrogen storage medium, a reformer that converts hydrocarbon fuels or organic solvents to hydrogen, or decomposable hydrides (i.e., metal hydrides and chemical hydrides) that release hydrogen by hydrolysis reactions. For a non-rechargeable micro fuel cell, as presented here, selections of hydrogen generation depend on the following factors:

1) hydrogen storage capacity;

2) temperature and pressure of the hydrogen storage and release processes;

3) complexity of the dehydrogenation process and its impact on the micro-fuel-cell architecture;

4) power consumption of the auxiliary system for dehydrogenation and controlled delivery of hydrogen to the membrane electrode assembly (MEA);

5) microfabrication issues.

2.4. Main Approach

The overall device consists of four layers, including as follows: 1) water reservoir; 2) membrane; 3) hydride reactor; and 4) membrane electrode assembly (MEA) as shown in a 3D schematic cross section in Figure 2.3. The no-power, self-regulating hydrogen generator is developed using a regulating valve separating between a hydride reactor and a water reservoir. The regulating valve consists of a port and a membrane with holes in it. Water flows through the port towards the hydride chamber, but stops within the membrane via holes due to capillary forces. Water vapor then diffuses into the hydride chamber resulting in

hydrogen generation (metal hydrides such as LiH, $LiAlH_4$, and CaH_2 react with water vapor to produce H_2 [70]). When the rate of hydrogen consumption by the fuel cell is lower than generation rate, gas pressure builds up inside the hydride reactor and deflects the membrane towards the water port, blocking the port and ceasing the water flow to the hydride after the water evaporates. This regulation action, however, assumes that the membrane deflects under a smaller pressure than needed to break into the liquid meniscus formed inside the membrane via holes. Under such conditions, complete isolation of the hydride reactor from the water reservoir can occur. When hydrogen consumption by the fuel cell is faster than the generation rate, the reverse happens, opening the membrane to allow water to diffuse into the hydride reactor, increasing the hydrogen generation. Essentially, the control mechanism is a passive valve that automatically regulates hydrogen production based on the hydride reactor pressure. Details of the valve operation and testing are discussed in the following sections.

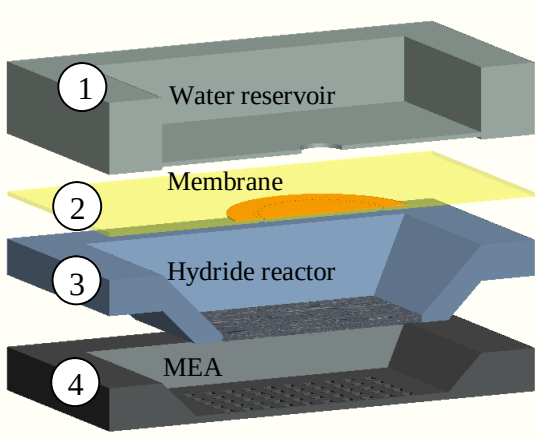

Figure 2.3. 3D schematic of the fully integrated device architecture.

2.5. Operating Principle

During the device operation (as shown in Figure 2.4), water enters the narrow space between the bottom of the reservoir and the membrane through a port at the bottom of the water reservoir. Capillary forces within the membrane holes keep the water from flowing into the hydride reactor. Water vapor diffuses into the hydride reactor (as shown in Figure 2.5) and hydrogen is consequently generated when water vapor reacts with the hydride. The generated hydrogen then leaves the hydride reactor through a porous wall at the bottom of the reactor and reaches the MEA. If hydrogen is not used by the MEA (i.e., open-circuit mode), pressure builds up inside the hydride reactor. The membrane is designed to deflect at a pressure (about 200 Pa) less than the capillary forces within the membrane holes. The deflection of the membrane plugs the water port and stops the flow of water from the reservoir. This control mechanism is essentially a passive valve that automatically closes when hydrogen is not consumed. Microfabrication of the device is described in the following section.

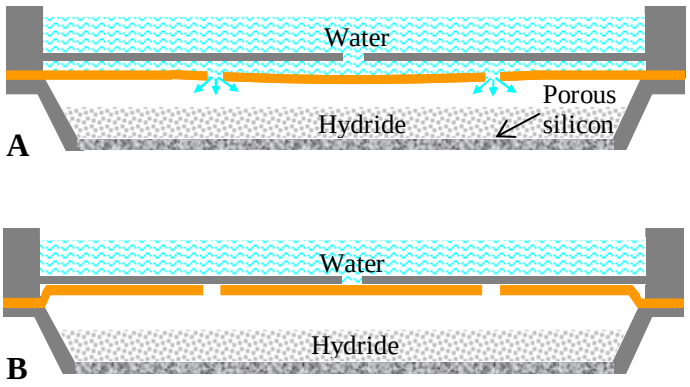

Figure 2.4. Schematic cross section of the self-regulating hydrogen generator and its operation principle. **A)** Membrane in release mode: water exits the reservoir and diffuses into the hydride reactor through the membrane holes. **B)** Membrane in closed mode: small pressure buildup in the hydride reactor, when hydrogen is not used, bends the membrane and closes the water gate.

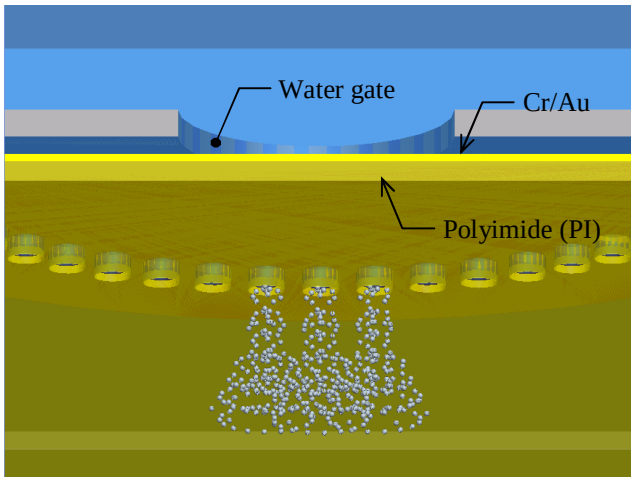

Figure 2.5. A 3D schematic showing vapor release when valve is open (i.e. membrane is in release mode).

2.6. Valve Fabrication

A 400-μm-thick <100> p-doped silicon wafer was used to fabricate the water reservoir. Figure 2.6(a-b) shows the microfabrication sequence of the water reservoir. A 300μm-diameter, 25μm deep hole was patterned and etched on one side of the wafer using the Bosch process. The wafer was then patterned and etched over a 2.4 × 2.4-mm^2 square area on both sides. The etched depth was 3 um on the side of the 300μm hole and 380μm on the opposite side of the wafer. The device was then hydroxylated in SC-1 solution (a mixture of 10:2:1 ratio of H_2O:H_2O_2:NH_4OH) to make the surface hydrophilic. Figure 2.6(c-e) also shows the microfabrication sequence of the membrane. Prior to spinning the polyimide (PI) layer, the glass wafer was coated with a layer of a releasing agent [a mixture of water, Poly(aspartic acid)-PAA, and sodium hydroxide] that was later dissolved in water, in order to release the membrane from the glass substrate. The membrane was then made through spin coating of polyimide PI-5878 (from HD MicroSystems, Wilmington, DE) on a glass substrate and then baking in a nitrogen oven at 200°C for 1 h and then 375°C for 2 h. The final thickness of the membrane was 5μm. The PI layer was then sputter coated with a 0.2μm-thick Au layer. A 150-Å Cr adhesion layer was used beneath the Au layer. In order to fabricate a circular array of 30μm-diameter holes through the PI membrane, the Cr/Au layer was patterned with photoresist and then etched. The PI layer was then etched using a reactive ion etching (RIE) process. The Cr/Au layer acted as a mask to protect the rest of the PI layer while being etched using a reactive ion etching (RIE) process. Finally, a circular area of 1.3mm-diameter at the center of the PI membrane was protected with photoresist, while the rest of the Cr/Au layer was etched away. Assembly process of the PI membrane to the water reservoir is shown in Figure 2.6(f-h). The PI membrane, while supported by the glass

substrate, was bonded to the water reservoir by using a MEMS adhesive layer [71] with the component shown in Table 2.3. The assembly was immersed in water for 4–6 days to release from the glass substrate. Figure 2.7-2.10 shows the images of the water reservoir, polyimide membrane before assembly, and the water reservoir and membrane assembly respectively.

Table 2.3: Content of the adhesion composition.

Material	Weight %
Novalac-modified resin [DER 672]	12
Curing agent [DEH 87]	5
2-methoxyethanol solvent	29
Anisole solvent	47
Propylene Glycol Methyl Ether Acetate (PGMEA) solvent	7

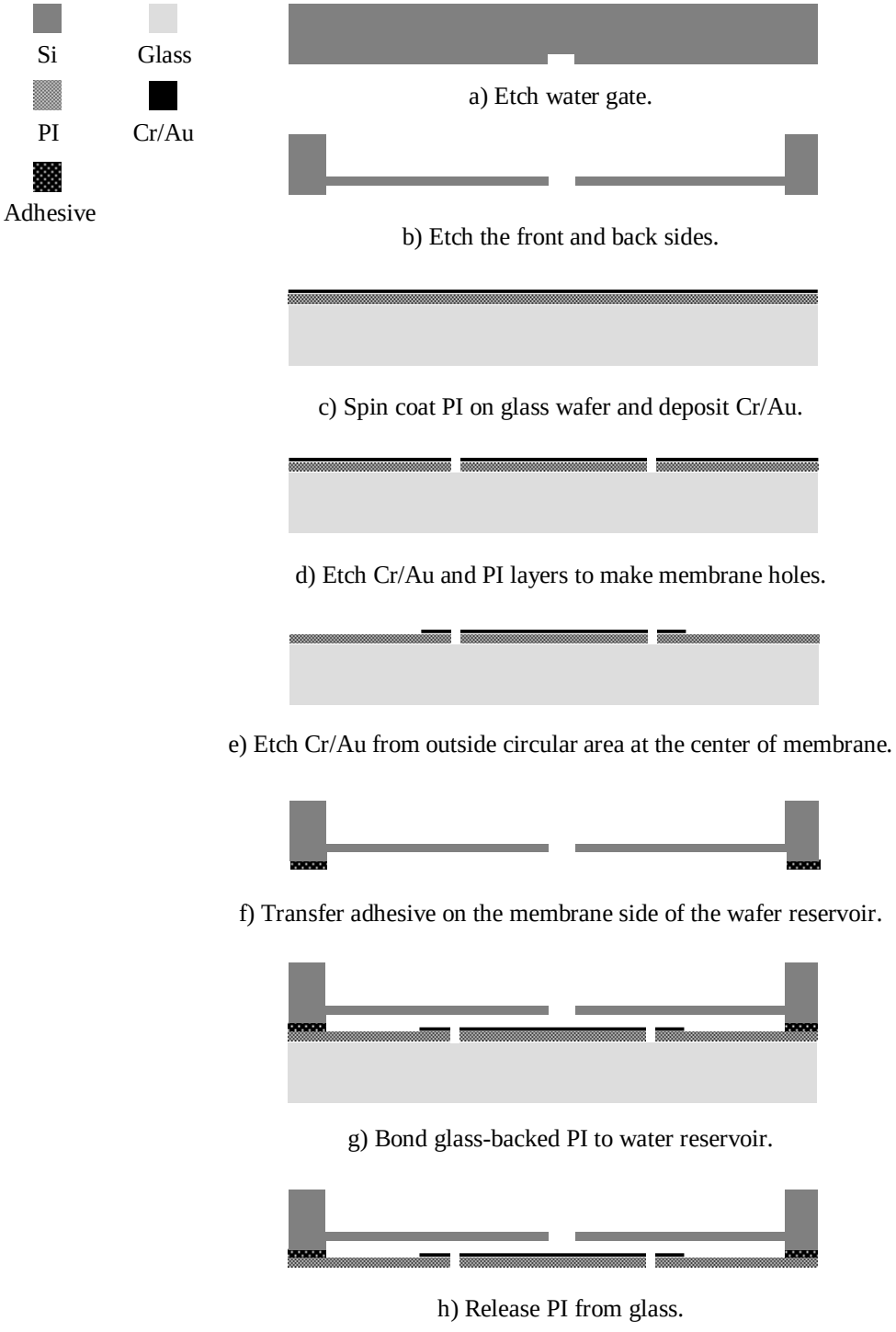

Figure 2.6. Microfabrication sequence of the water reservoir and membrane assembly.

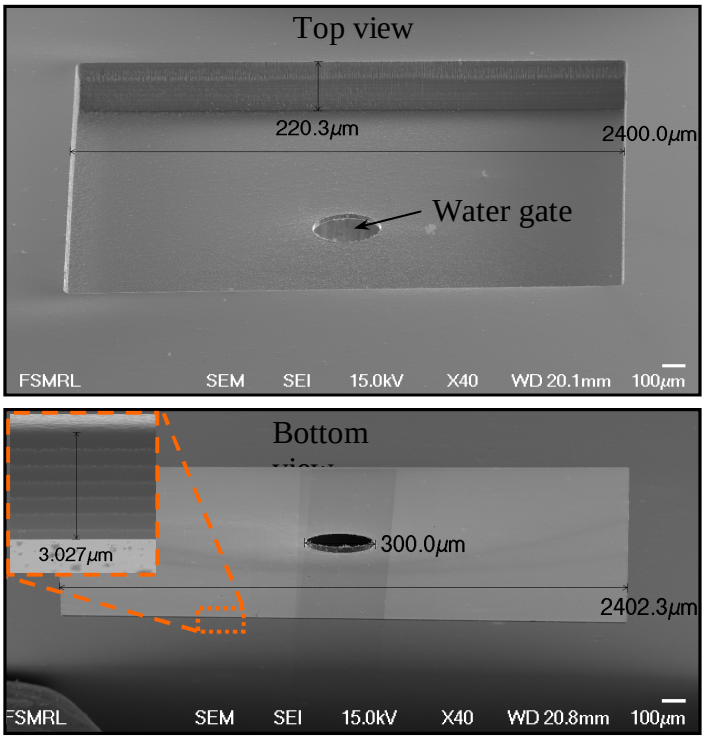

Figure 2.7. Top and bottom views of the water reservoir. The inset figure in the bottom view shows a 3μm deep recess that separates the reservoir from the PI membrane. Thickness of the reservoir bottom wall is 20μm.

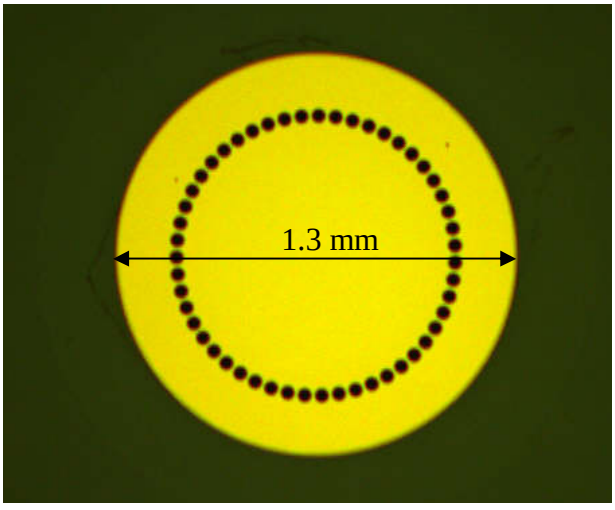

Figure 2.8. Top view of the center of the polyimide membrane coated with Cr/Au to prevent water diffusion through the membrane. The holes are 40-μm in diameter.

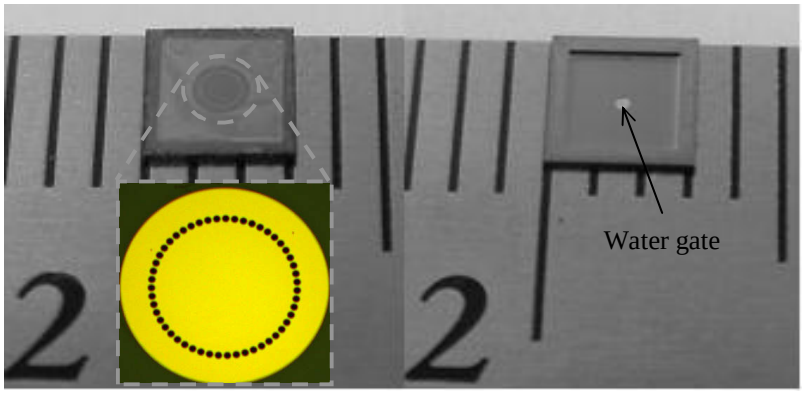

Figure 2.9. Membrane and reservoir views of the 3×3 mm^2 water reservoir and membrane assembly. Membrane holes can be seen in the inset figure.

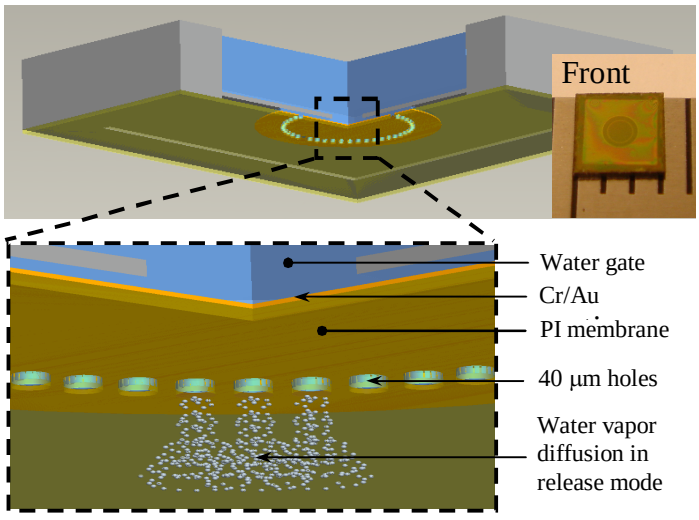

Figure 2.10. Membrane and water reservoir assembly. The inset image shows the membrane-side view of the actual device. The schematic also shows how water diffuses out of the holes when membrane is in release mode.

2.7. Fabrication of Hydride Reactor

A 500μm-thick <100> p-doped wafer was used to fabricate the hydride reactor. The fabrication process was conducted in two KOH etching steps, as shown in Figure 2.11. A low-pressure chemical vapor deposition (LPCVD) nitride was used as the masking material. Note that the corner compensation method [72] was used for etching the mesa. The hydride reactor depth is 460μm. The hydride reactor was then installed in a two-chamber anodization bath. Figure 2.12 shows the arrangement of the apparatus used for the anodization process. Anodization was conducted in a 25% HF electrolyte at a current density of about 30 mA/cm^2. The pores penetrated about 40 μm-deep into the exposed silicon areas, which included side and bottom walls of the hydride reactor. Since sidewall thickness was about 80μm, the pores penetrated only through half of the wall thickness, whereas the bottom wall became entirely porous except for a 50 nm-thick layer at the bottom of the pores. The nonporous silicon layer was later dry etched. The bottom of porous wall, as well as its cross-section view, is shown in Figure 2.13 and 2.14.

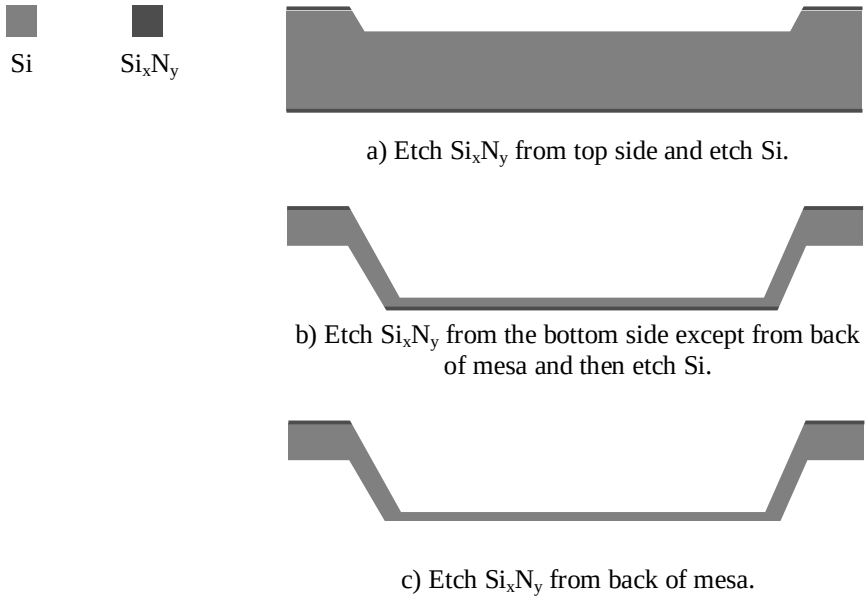

Figure 2.11. Microfabrication sequence of the hydride reactor.

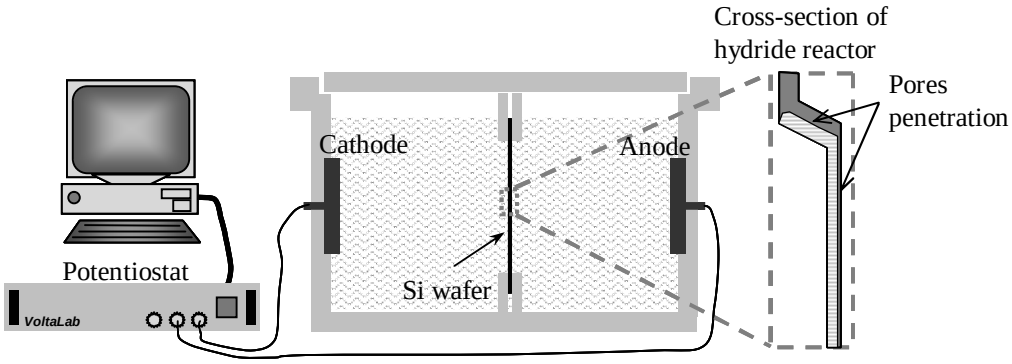

Figure 2.12. Schematic of the apparatus used for anodization of the hydride reactor.

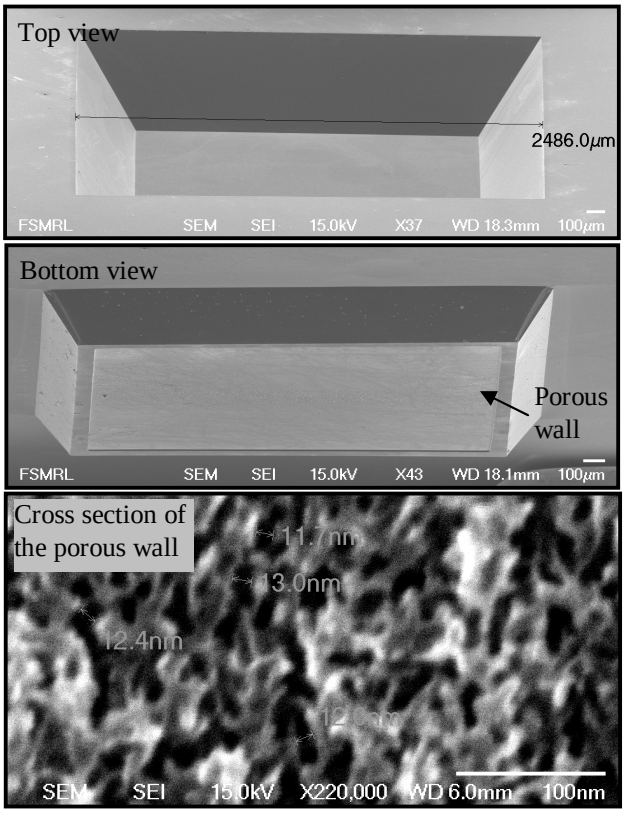

Figure 2.13. Bottom and top views and cross section of the hydride reactor. The shallow recess on the porous silicon wall of the reactor formed after the etch process in ICP-DRIE. The etching process was conducted to removed nonporous silicon, but since etch rate of porous silicon is about 2-3 times faster than that of silicon, the porous wall got etched a few microns more than the sides.

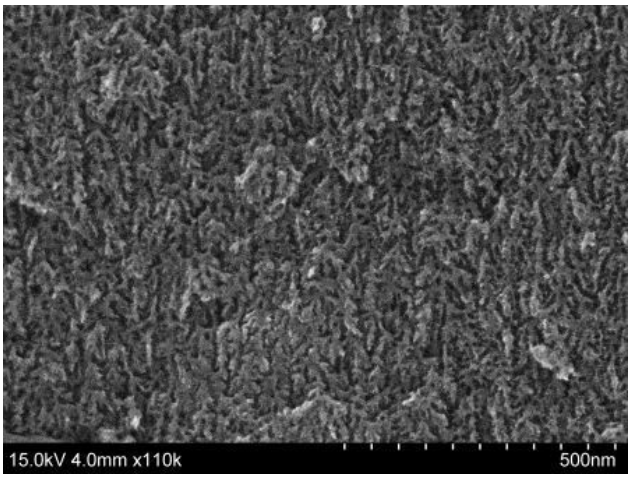

Figure 2.14. Cross-section view of the hydride reactor porous silicon wall.

2.8. Silicon/Nafion-based MEA Fabrication

The first generation of MEA was made using a SOI wafer with a 300μm-thick <100> n-type handle wafer and a 40μm-thick device layer. A 0.25μm-thick LPCVD nitride layer was deposited on the wafer. Figure 2.15 shows the fabrication sequence for Si-MEA. The silicon nitride layer was patterned and etched from 2.4 × 2.4 mm^2 square areas on the handle wafer side, and then silicon was etched in KOH solution until the oxide layer was reached. A 0.2 μm-thick Cr/Au layer was deposited on both sides of the membrane. The membrane was then etched (all five layers including Cr/Au on the front side, silicon nitride, silicon, silicon oxide, and Cr/Au on the backside) using wet and dry etch processes to open 100 × 100μm^2 square openings that were 100 μm apart, over a 2 × 2 mm^2 area at the center of the membrane. Instead of the KOH wet etch, the 40μm-thick device layer could be etched using DRIE process to open 100μm×100μm square openings that were 100μm apart (as shown in Figure 2.16) over a 1mm×1mm area. The structures are similar for both methods.

After that, a solution of Nafion® solution (28μL of 5 wt.% Nafion® ionomer 1100EW from Solution Technology, Inc.), was then painted with a paintbrush on the perforated silicon membrane to fill the openings. A leak test was performed using an in-house device. Catalyst ink was then prepared by dispersing platinum black HiSPEC 1000 (from Alfa Aesar Co.) in Nafion® solution, Millipore water, and isopropanol via sonication. Using the direct paint method, the catalyst ink was painted on both sides of the membrane (i.e., anode and cathode). The resulting catalyst loading was approximately 20 mg/cm^2. In addition to the membrane area, a small amount of catalyst ink was painted onto the gold current collectors to provide electrical connection. The current collectors were made through sputter deposition of 0.1 μm thick Cr/Au layers on the anode and cathode sides. The micro hydrogen generator was then epoxied (using Scotch- Weld 2216 B/A Gray epoxy from 3M Co.) onto the MEA to make an integrated hydrogen generator-fuel cell assembly.

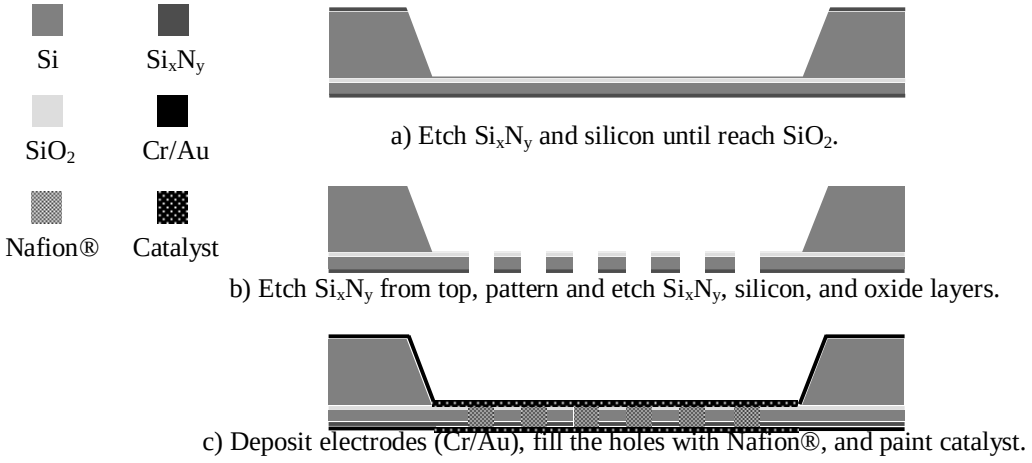

Figure 2.15. Microfabrication sequence of MEA.

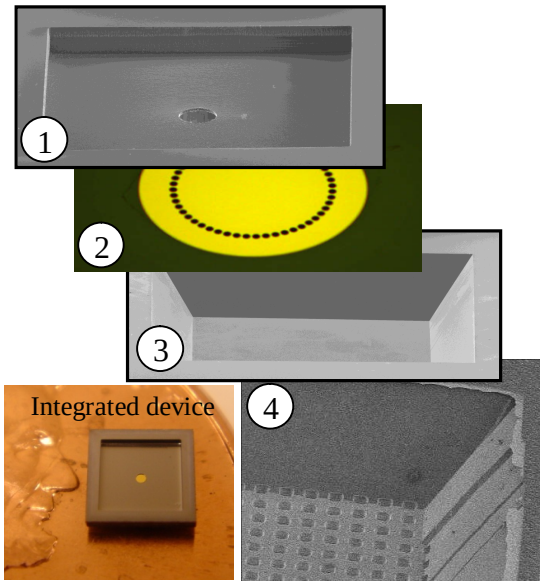

Figure 2.16. Images of different layers of device and their assembly. The SOI-based membrane electrode assembly (MEA) is shown in the most bottom of the assembly.

2.9. Characterizations

2.9.1. Bulge Test

A test piece was fabricated to determine the membrane deflection with pressure. The test piece was a silicon die (10mm×10mm) with 2.4mm×2.4mm opening at its middle, over which the PI membrane was bonded. The PI membrane was similar to that of the device in every aspect (i.e. size and microfabrication process) except that it did not have the 30μm holes and the silicon membrane inside of the water reservoir. A bulge test setup was used to measure the membrane deflection at different pressures. The test piece was installed on the pressure chamber of the setup, as depicted in Figure 2.17. The chamber pressure was increased using a piezoelectric actuator. As the results in Figure 2.18, an applied pressure of approximately 150 Pa is sufficient to deform the membrane 3μm. This value corresponds to the calculated pressure required for the rectangular membrane with a 3μm deflection in literatures. Also, this pressure is significantly less than the typical water capillary pressure in the micro-scale via holes. For example, capillary pressure in a 30μm hole with a surface to liquid contact angle of $\theta = 50$ degrees is approximately 6 kPa ($P = 2*\cos\theta/r$). This suggests that the membrane will deflect and seal the water port before hydrogen can break the capillary meniscus formed inside the membrane holes.

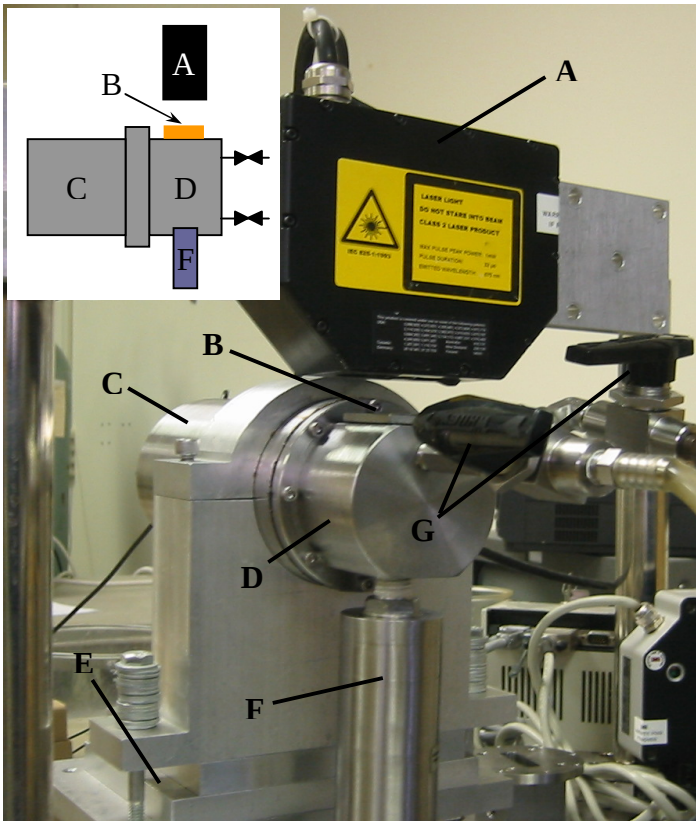

Figure 2.17. Bulge test setup. Main system components: A) laser sensor model 812330-SLS 700/15 from LMI Selcom, Inc., B) a jig for holding the test article, C) piezoelectric actuator model P-239.60 HVPZT from Physik Instrumente GmbH & Co. KG, D) water chamber, E) micro positioning stage, F) pressure transducer model PX 309-001GV S5V from OMEGA Co., and G) water inlet/outlet valves. The test article is attached to the jig (A). The micro positioning stage is used to adjust the sample right below the optical sensor. Next, water chamber (D) is filled with water using the inlet/outlet valves (G). The water level reaches the top of the water chamber but doesn't come into contact with the membrane.

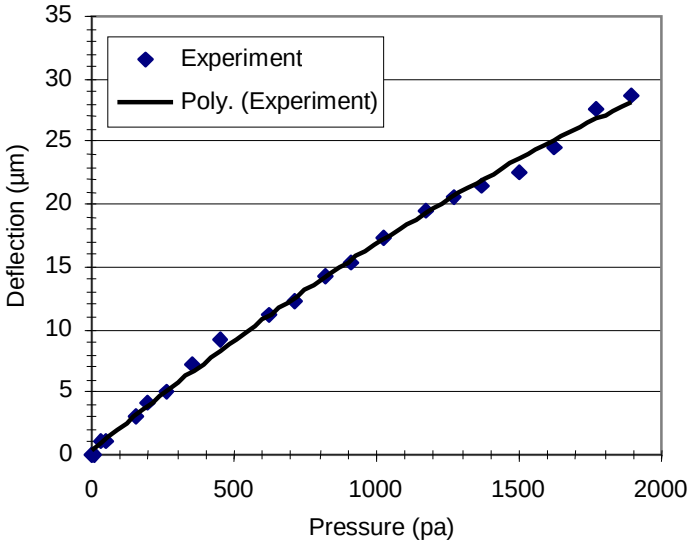

Figure 2.18. Test results show the relationship of membrane deflection and applied pressure.

2.9.2. Humidity Set-up

An experimental setup was fabricated to test the valve performance. The setup determines the open and close states of the valve as well as the water vapor released rate through the holes when the valve is open. Figure 2.19 shows a schematic of the setup. The setup consists of two main chambers C-1 and C-2. Pressure inside each chamber is adjusted by changing the liquid (Fomblin oil) level in manometers M-1 and M-2. Two push-button valves V-1 and V-2 allow purging of the C-2 chamber with dry nitrogen. A humidity sensor (Model SHT75, size 3.7mm×2.2mm×4.9mm, from Sensirion, Inc.) installed on the bottom of the C-2 chamber measures the relative humidity. The valve and water reservoir assembly was installed between the C-1 and C-2 chambers. Water was supplied to the water reservoir (i.e. topside of the valve). The two chambers were kept at the same pressure. The C-2 chamber was purged with nitrogen until a humidity level of less than 1% was reached immediately

after purging the chamber (i.e. closing the V-1 and V 2 valves), the chamber humidity started to raise indicating water vapor release by the valve. The chamber was purged with nitrogen again and the increase in the relative humidity was measured. This process was repeated several times, as shown in in Figure 2.20. Finally, pressure inside the C-2 chamber was increased approximately 400 Pa above that of the C-1 chamber by adjusting the liquid level in manometer M-2. The chamber was purged with nitrogen for several minutes. As can be seen in the same figure, the humidity did not rise at this point, showing that the valve was closed.

During the course of the experiment, no bubbles were observed to enter the water reservoir, indicating that the membrane deflection and capillary forces did not allow hydrogen to pass through the valve. Without the membrane, bubbles are observed to pass, even through long microchannels connecting the water reservoir to the hydride reactor. Also, the bottom wall of the water reservoir did not measurably bulge, suggesting that the hydrogen pressure did not increase measurably inside the device.

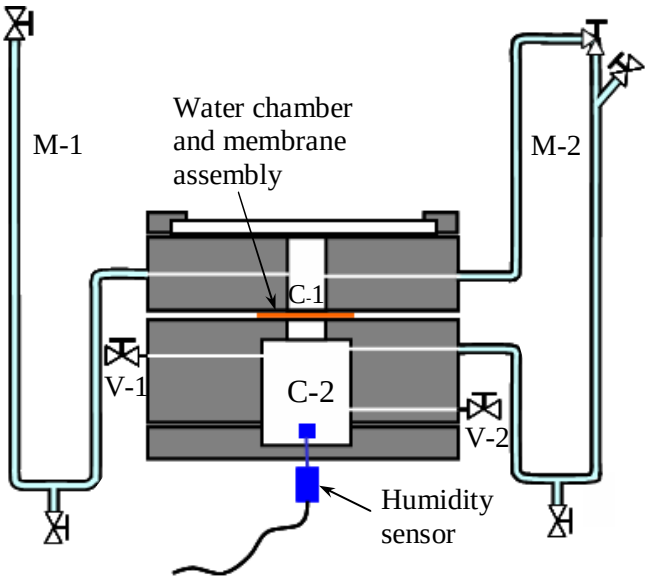

Figure 2.19. Schematic of the test setup for measuring the valve performance.

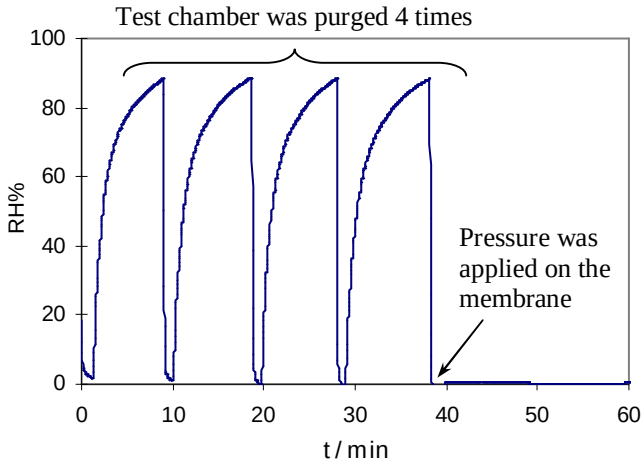

Figure 2.20. Valve performance test results showing its closure after a pressure of approximately 400 Pa was applied on the membrane. The chamber was purged for a few minutes after the fourth cycle.

2.10. Integrated Devices Testing (First Generation)

The hydride reactor was fabricated from <100> p-doped silicon using DRIE process. A 20μm recess was etched at the bottom of the hydride reservoir facing the MEA to facilitate its assembly on the MEA. The bottom wall of the hydride reactor was then anodized in a 25% HF electrolyte to produce ~5 nm diameter pores (previously shown in Figure 2.14) that allow hydrogen to exit the reactor. Typically, 60–70% of the hydride reactor is charged with $LiAlH_4$ (Sigma–Aldrich, Inc., St. Louis, MO). $LiAlH_4$ has the highest reaction rate with water vapor among typical chemical hydrides (e.g. CaH_2, $NaAlH_4$, $LiBH_4$, and $NaBH_4$) [70].

Approximately 60% of the hydride reactor volume was filled with $LiAlH_4$ powder (from Sigma-Aldrich, Inc., St. Louis, MO) inside a glove box. The membrane/water reservoir assembly was then attached on top of the hydride reservoir using Scotch-Weld 2261 B/A Gray epoxy (from 3M, Inc., St. Paul, MN). The entire assembly of the water reservoirs (as

shown in Figure 2.21) was then epoxied on the MEA. The device was left in a glove box for about 10 h for the epoxy to dry. Figure 2.22 shows the device assembly after pouring the epoxy between the hydrogen generator and the MEA.

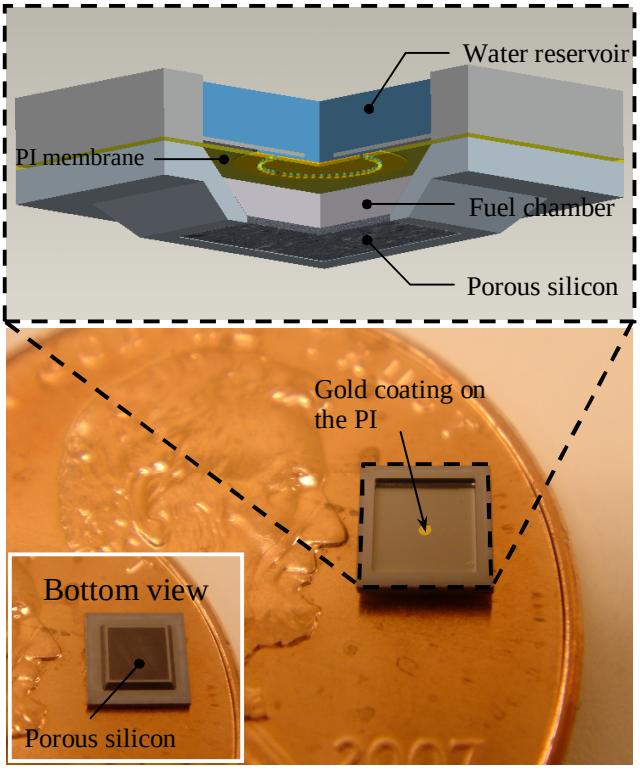

Figure 2.21. Schematic assembly of the self-regulating hydrogen generator and the actual images of the top and bottom of the hydrogen generator.

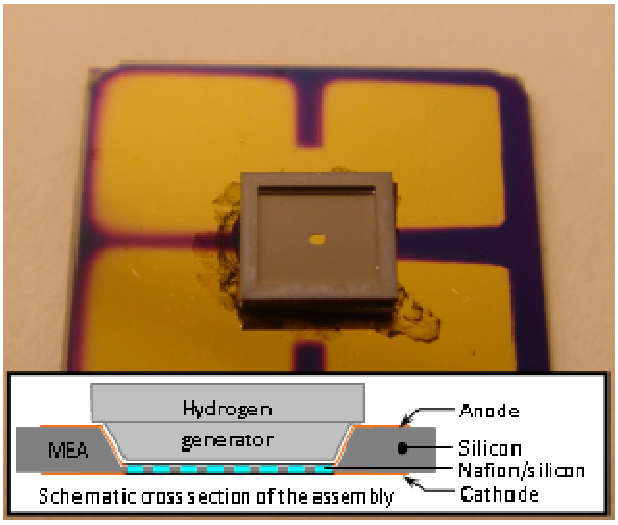

Figure 2.22. Self-regulating hydrogen generator assembled on a microfabricated hybrid silicon/Nafion MEA. The image was taken after epoxy (3M Scotch-Weld 2216 B/A Gray) was poured around the micro hydrogen generator to fix it on the MEA.

A Solartron SI 1287 potentiostat was used to conduct the tests. The integrated device was installed in a test stand that connected the anode and cathode electrodes to the potentiostat. Several devices were fabricated to conduct the following: 1) a set of tests to determine device behavior under varying load conditions and 2) life tests to determine the device energy density.

The primary goals of this experiment were the following. (1) To find out if hydrogen bubbles pass through the valve and enter the water reservoir. (2) Confirm valve closure through analysis of current transients as well as physical evidence (failure of the device due to fracture of its elements) suggesting continuous hydrogen generation and pressure build-up inside the device. In the second test, the device voltage was changed in saw-tooth wave form between 0.3 and 0.7V to evaluate the response of the control mechanism to gradual changes in load conditions.

During the course of the experiment, the humidity level in the test room was between 30% and 50%. A typical test started by supplying water to the device water reservoir. The open-circuit potential quickly increased to a maximum of about 0.9 V, as water vapor was released by the control system into the hydride chamber and the generated hydrogen reached the MEA. In the first run, the I–V characteristic curve of the device was determined. Figure 2.23 shows a typical result and its comparison with the I–V curve of the MEA before integration (using hydrogen and oxygen gas). The comparison of the two performance curves clearly suggests that the activation and ohmic polarization losses of the MEA have increased after integration. More importantly, the results show that the device performance at voltages of less than 0.6 V is limited by hydrogen generation rate. In a second test, the potentiostat was set to switch the device voltage between the open-circuit voltage and 0.3 V several times (i.e., square wave form), as shown in Figure 2.24. During the open-circuit mode, the potentiostat simply measures the device output voltage when no current is drawn from the device. The integrated device was tested using a Solartron SI 1287 potentiostat. The water reservoir was filled and tests were conducted.

Analysis of the device current output also provided interesting insight about hydrogen generation. As can be seen in Figure 2.24, after 3 min of the device not consuming any hydrogen (i.e. open circuit mode), no spike in current (beyond the steady-state value) was observed when the voltage was dropped to 0.3 V. This test suggests that hydrogen was not produced and did not accumulate inside the device when no current was drawn. Note that higher currents can be generated with increased hydrogen pressure, considering that the MEA is capable of delivering an order of magnitude higher current ($700 mA cm^{-2}$ at the operating voltage of 0.3 V), than what was delivered by the integrated device. The small

spike of ~1mA cm^{-2} versus 8mAcm^{-2} is mainly an artifact of the experiment. A similar negative spike can be seen when current goes to zero, which suggests the spikes are due to the measurement electronics on abrupt voltage changes. Also, the near square-wave variation of the current generated showed that the hydrogen generation due to changes in the valve responded in less than a second. The smooth variations of the output current in response to the gradual changes in voltage (i.e. saw-tooth wave form) suggested that the hydrogen generator provided sufficient hydrogen to the MEA when needed and reduced supply when the consumption rate was low.

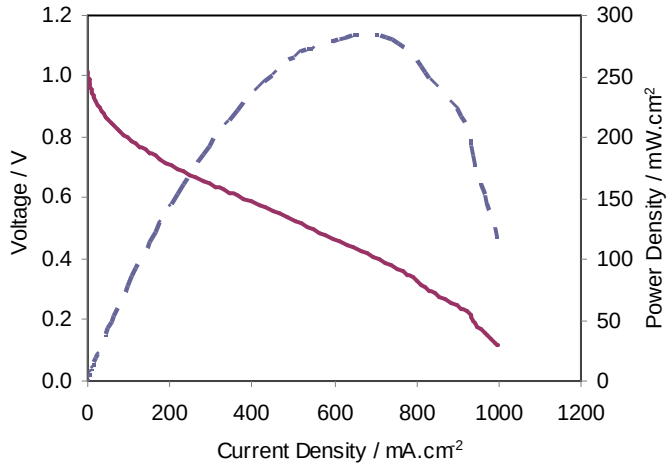

Figure 2.23. Polarization curve of the hybrid Nafion®/silicon MEA.

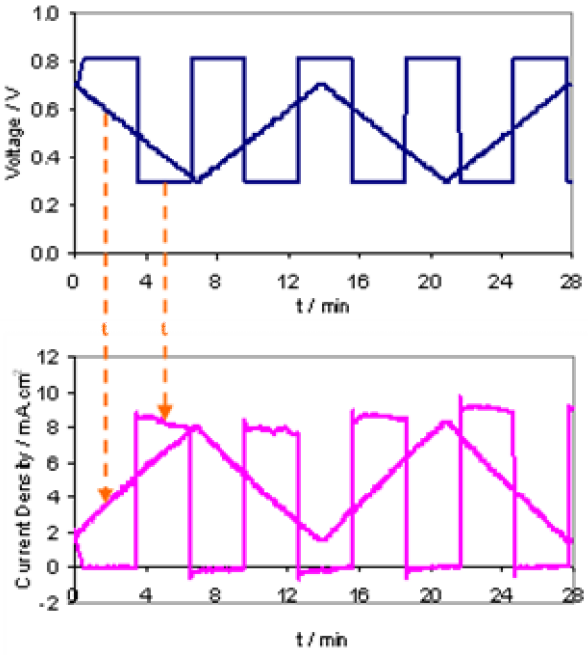

Figure 2.24. Performance of the integrated device under different load conditions. Test was conducted using fuel cell test machine Model 10AI (from Fuel Cell Technologies, Inc.). Device was run at varying voltage (square and saw-tooth waves) conditions and its current response was determined.

Three devices were tested to determine maximum achievable energy density. The devices were operated at 0.7 V until they ran out of fuel. Figure 2.25 shows the test results. The devices delivered a current of close to 0.1 mA at the beginning. Over time, however, the current decreased. It is suspected that this is due to the reduction in hydrogen generation rate over time. One explanation could be a decrease in the water vapor rate reaching the unreacted fuel at the bottom of the hydride reactor, as thickness of the reaction products gradually increased. One challenge with this reaction is the formation of compounds that are often impermeable to water vapor. More research is required to clearly find the main cause of this

behavior. The focus for this research group is currently to resolve this issue by conducting extensive research.

The energy density of the devices was between 244 and 262 Wh/L (with an average value of 254 Wh/L), calculated by dividing the overall generated energy (integral of the generated power reported in Figure 2.25) by the device volume. Considering that the hydride reactor was filled with 1.2 mg of $LiAlH_4$ (60% of the 2.22 μL reactor volume), which could generate hydrogen for 4.7-mWh energy (or 522.2 Wh/L) at an operating voltage of 0.7 V, suggested that only about 49% of the fuel was utilized in the device. The rest of the fuel could have either stayed unreacted in the reactor or the generated hydrogen leaked from the device through the adhesives that may not be hydrogen impermeable. Further studies are required to quantify and minimize these losses. Achieving an energy density on the order of 400 Wh/L is feasible with a fuel utilization efficiency of about 80%.

In addition, a calculation suggests that using the following reaction, a theoretical energy density of 756 Wh/L at the operating voltage of 0.7 V (or 863 Wh/L at 0.8 V) could be achieved:

$H_2O + 0.55\ NH_4F + 0.8\ LiBH_4 \rightarrow 0.55\ LiF + 0.55\ BN + 0.25\ LiOH + 0.25\ H_3BO_3 + 3.2\ H_2$.

Through implementation of this chemistry, an energy density on the order of 700 Wh/L can be achieved.

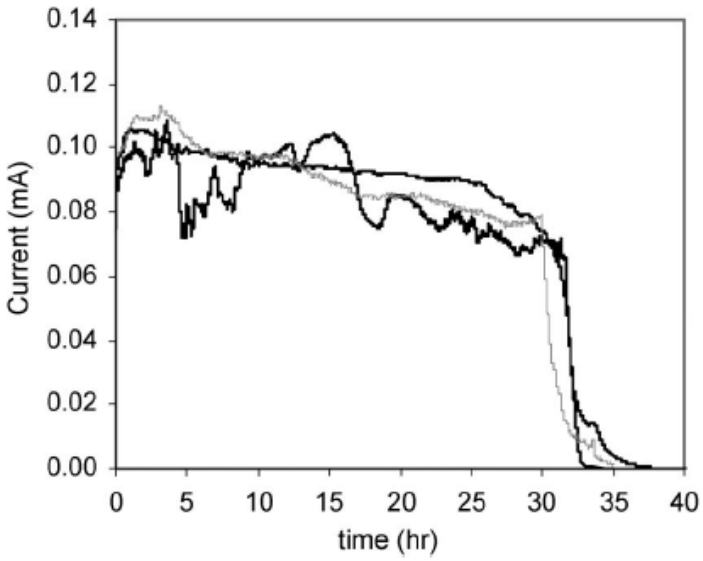

Figure 2.25. Current output of three devices operated at a constant voltage of 0.7 V. The overall energy density of the three devices varied from 244 to 262 Wh/L.

2.11. Conclusion

The development of a self-regulating micro hydrogen generator for micro fuel cells was reported. The device employs a regulator micro valve for controlling the rate of hydrogen generation in a hydride reactor, eliminating the need for complex auxiliary systems commonly suggested in hydrogen generators. The control mechanism takes advantage of capillary forces to maintain water inside a confined volume connected to a water reservoir. It delivers water vapor to the hydride reactor when hydrogen pressure inside the hydride reactor is low and relies on deflection of a membrane to seal off the water reservoir from the hydride reactor when the reactor pressure increases due to excess generation of hydrogen over that consumed by the fuel cell. A fully integrated millimeter-scale fuel-cell-based power source with onboard fuel and a control system was developed. Fabrication of this high energy density device in such a small volume (9 µL or 3 × 3 × 1 mm^3) was enabled through implementation of a scalable design architecture and using a new passive control mechanism

that occupies very little volume (less than 0.5% of the device volume). The performance of the device under varying load conditions was successfully demonstrated. The operation of the device under a constant load over a long period of time (more than 32 h) resulted in a relatively stable performance and 254 Wh/L energy output. Simplicity of the design and microfabrication processes suggested in this paper has opened a new opportunity for commercialization of more cost-effective micro fuel cells.

Several unique qualities of the hydrogen generator regulator are:

(1) The control mechanism occupies a volume of less than 50 nL (approximately 0.5% of the volume of the millimeter-scale integrated device developed in this study);

(2) Unlike most other control mechanisms, the proposed design consumes no energy;

(3) The device operates passively without a need for external electronics, allowing the fuel cells to operate similar to batteries; and

(4) The fabrications of millimeter-scale fully integrated micro fuel cells are enable by MEMS processes for the development of membrane technologies.

2.12. References

[1] J. N. Baker and A. Collinson, "Electrical energy storage at the turn of the Millennium," *Power Engineering Journal,* vol. 13, pp. 107-12, 1999.

[2] R. M. Dell and D. A. J. Rand, "Energy storage-a key technology for global energy sustainability," *Journal of Power Sources,* vol. 100, pp. 2-17, 2001.

[3] A. S. Arico, P. Bruce, B. Scrosati, J. Tarascon and W. Van Schalkwijk, "Nanostructured materials for advanced energy conversion and storage devices," *Nature Materials,* vol. 4, pp. 366-377, 2005.

[4] M. Armand and J. M. Tarascon, "Building better batteries," *Nature,* vol. 451, pp. 652-7, 2008.

[5] R. J. Wood, "Liftoff of a 60mg flapping-wing MAV," in *IEEE International Conference on Intelligent Robots and Systems,* San Diego, CA, United states, 2007, pp. 1889-1894.

[6] S. Bergbreiter and K. S. J. Pister, "Design of an autonomous jumping microrobot," in *IEEE International Conference on Robotics and Automation,* Piscataway, NJ, USA, 2007, pp. 7 pp.

[7] R. R. Selmic and A. Mitra, "Position-adaptive explosive detection concepts for swarming micro-UAVs," in *SPIE - the International Society for Optical Engineering,* USA, 2008, pp. 696106-1.

[8] S. Hollar, A. Flynn, C. Bellew and K. S. J. Pister, "Solar powered 10 mg silicon robot," in *IEEE Micro Electro Mechanical Systems (MEMS)*, Kyoto, Japan, 2003, pp. 706-711.

[9] A. Boletis, W. Driesen, J. M. Breguet and A. Brunete, "Solar cell powering with integrated global system for mm3 size robots," in *IEEE/RSJ International Conference on Intelligent Robots and Systems*, Piscataway, NJ, USA, 2006, pp. 5528-33.

[10] W. Smith, "The role of fuel cells in energy storage," *Journal of Power Sources*, vol. 86, pp. 74-83, 2000.

[11] B. C. H. Steele and A. Heinzel, "Materials for fuel-cell technologies," *Nature*, vol. 414, pp. 345-352, 2001.

[12] A. Heinzel, C. Hebling, M. Müller, M. Zedda and C. Müller, "Fuel cells for low power applications," *Journal of Power Sources*, vol. 105, pp. 250-255, 2002.

[13] G. J. La O, I. Hyun Jin, E. Crumlin, G. Barbastathis and S. Yang, "Recent advances in microdevices for electrochemical energy conversion and storage," *International Journal of Energy Research*, vol. 31, pp. 548-75, 2007.

[14] J. D. Morse, "Micro-fuel cell power sources," *International Journal of Energy Research*, vol. 31, pp. 576-602, 2007.

[15] A. Kundu, J. H. Jang, J. H. Gil, C. R. Jung, H. R. Lee, S. H. Kim, B. Ku and Y. S. Oh, "Micro-fuel cells-Current development and applications," *Journal of Power Sources*, vol. 170, pp. 67-78, 2007.

[16] M. Broussely and G. Archdale, "Li-ion batteries and portable power source prospects for the next 5-10 years," *Journal of Power Sources,* vol. 136, pp. 386-394, 2004.

[17] S. Tanaka, K. Chang, K. Min, D. Satoh, K. Yoshida and M. Esashi, "MEMS-based components of a miniature fuel cell/fuel reformer system," *Chemical Engineering Journal,* vol. 101, pp. 143-149, 2004.

[18] C. Xie, J. Bostaph and J. Pavio, "Development of a 2 W direct methanol fuel cell power source," *Journal of Power Sources,* vol. 136, pp. 55-65, 2004.

[19] S. Yao, X. Tang, C. Hsieh, Y. Alyousef, M. Vladimer, G. K. Fedder and C. H. Amon, "Micro-electro-mechanical systems (MEMS)-based micro-scale direct methanol fuel cell development," *Energy,* vol. 31, pp. 636-649, 2006.

[20] W. Qian, D. P. Wilkinson, J. Shen, H. Wang and J. Zhang, "Architecture for portable direct liquid fuel cells," *Journal of Power Sources,* vol. 154, pp. 202-213, 2006.

[21] K. W. Oh and C. H. Ahn, "A review of microvalves," *Journal of Micromechanics and Microengineering,* vol. 16, pp. R13-R39, 2006.

[22] H. Zhao, K. Stanley, Q. M. J. Wu and E. Czyzewska, "Structure and characterization of a planar normally closed bulk-micromachined piezoelectric valve for fuel cell applications," *Sensors and Actuators A,* vol. 120, pp. 134-141, 2005.

[23] E. T. Carlen and C. H. Mastrangelo, "Surface Micromachined Paraffin-Actuated Microvalve," *Journal of Microelectromechanical Systems,* vol. 11, pp. 408-420, 2002.

[24] N. Vandelli, D. Wroblewski, M. Velonis and T. Bifano, "Development of a MEMS microvalve array for fluid flow control," *Journal of Microelectromechanical Systems,* vol. 7, pp. 395-403, 1998.

[25] J. P. Hensel, R. S. Gemmena, J. D. Thornton, J. S. Vipperman, W. W. Clark and B. A. Bucci, "Effects of cell-to-cell fuel mal-distribution on fuel cell performance and a means to reduce mal-distribution using MEMS micro-valves," *Journal of Power Sources,* vol. 164, pp. 115–125, 2007.

[26] A. Richter, D. Kuckling, S. Howitz, T. Gehring and K. Arndt, "Electronically Controllable Microvalves Based on Smart Hydrogels: Magnitudes and Potential Applications," *Journal of Microelectromechanical Systems,* vol. 12, pp. 748-753, 2003.

[27] J. S. Bintoro and P. J. Hesketh, "An electromagnetic actuated on/off microvalve fabricated on top of a single wafer," *Journal of Micromechanics and Microengineering,* vol. 15, pp. 1157-73, 2005.

[28] P. J. Hesketh, J. S. Bintoro and R. Luharuka, "Microvalve for Fuel Cells and Miniature Gas Chromatographic System," *Sensors Update,* vol. 13, pp. 233-302, 2004.

[29] D. P. Wilkinson, R. Rahbari, J. Zimmerman and M. Blanco, "Flow control apparatus and method for fuel cell flow fields,", 2005.

[30] B. Schumm, "Fluid regulating microvalve assembly for fluid consuming cells,", 2006.

[31] S. Masaaki, H. Yosuke, J. Kazushi and T. Shigeaki, "Fuel Control Micro-Valve for Portable Fuel Cells," *MEW Technical Report,* vol. 53, pp. 76-80, 2005.

[32] F. F. Sherman, V. Gartstein and D. J. Quiram, "Microvalve for controlling fluid flow," 2001.

[33] K. Yoshida, Y. Hagihara, M. Saitoh, S. Tomonari, S. Tanaka and M. Esashi, "Microvalve to Control Fuel for Portable Fuel Cells," *Transactions on Sensors and Micromachines, the Institute of Electrical Engineering of Japan,* vol. 125, pp. 418-423, 2005.

[34] R. Gemmen, J. Thornton, J. S. Vipperman and W. W. Clark, "Piezoelectric axial flow microvalve," 2007.

[35] K. Yoshida, Y. Hagihara, S. Tanaka and M. Esashi, "Normally-closed electrostatic micro valve with pressure balance mechanism for portable fuel cell application," in *Proceedings of IEEE International Conference on Micro Electro Mechanical Systems (MEMS),* 2006, pp. 722-725.

[36] E. (. Yang, C. Lee, J. Mueller and T. George, "Leak-Tight Piezoelectric Microvalve for High-Pressure Gas Micropropulsion," *Journal of Microelectromechanical Systems,* vol. 13, pp. 779-807, 2004.

[37] O. Soerensen, K. S. Drese, W. Ehrfeld and H. Hartmann, "Micromachined flow handling components - micropumps," in *Proceedings of SPIE - the International Society for Optical Engineering,* 1999, pp. 52-60.

[38] A. K. Da Silva, M. H. Kobayashi and C. F. M. Coimbra, "Optimal design of non-Newtonian, micro-scale viscous pumps for biomedical devices," *Biotechnology and Bioengineering,* vol. 96, pp. 37-47, 2007.

[39] J. Doepper, M. Clemens, W. Ehrfeld, S. Jung, K. -. Kaemper and H. Lehr, "Micro gear pumps for dosing of viscous fluids," *Journal of Micromechanics and Microengineering,* vol. 7, pp. 230-232, 1997.

[40] S. Hayamizu, K. Higashino, Y. Fujii, Y. Sando and K. Yamamoto, "Development of a bi-directional valve-less silicon micro pump controlled by driving waveform," *Sensors and Actuators A,* vol. 103, pp. 83-87, 2003.

[41] D. Liu, M. Maxey and G. E. Karniadakis, "Modeling and optimization of colloidal micro-pumps," *Journal of Micromechanics and Microengineering,* vol. 14, pp. 567-575, 2004.

[42] K. Yang, I. Chen and C. Wang, "Performance of nozzle/diffuser micro-pumps subject to parallel and series combinations," *Chemical Engineering and Technology,* vol. 29, pp. 703-710, 2006.

[43] X. Yang, Z. Zhou, H. Chod and X. Luod, "Study on a PZT-actuated diaphragm pump for air supply for micro fuel cells," *Sensors and Actuators A,* vol. 130–131, pp. 531–536, 2006.

[44] Y. Takeuchi, H. Tsuji, K. Kitamura and N. Takahashi, "Method for manufacturing a cell-driving-type micro pump member," 2004.

[45] Y. Takeuchi, H. Tsuji, K. Kitamura and N. Takahashi, "Micro pump,", 2004.

[46] R. Hahn, S. Wagner, A. Schmitz and H. Reichl, "Development of a planar micro fuel cell with thin film and micro patterning technologies," *Journal of Power Sources,* vol. 131, pp. 73-78, 2004.

[47] J. Yeom, G. Z. Mozsgai, B. R. Flachsbart, E. R. Choban, A. Asthana, M. A. Shannon and P. J. A. Kenis, "Microfabrication and characterization of a silicon-based millimeter scale, PEM fuel cell operating with hydrogen, methanol, or formic acid," *Sensors and Actuators B,* vol. 107, pp. 882-891, 2005.

[48] K. Chu, S. Gold, V. Subramanian, C. Lu, M. A. Shannon and R. I. Masel, "A nanoporous silicon membrane electrode assembly for on-chip micro fuel cell," *Journal of Microelectromechanical Systems,* vol. 15, pp. 671-677, 2006.

[49] K. Chu, M. A. Shannon and R. I. Masel, "An improved miniature direct formic acid fuel cell based on nanoporous silicon for portable power generation," *Journal of the Electrochemical Society,* vol. 153, pp. 1562-1567, 2006.

[50] T. Pichonat and B. Gauthier-Manuel, "Recent developments in MEMS-based miniature fuel cells," *Microsystem Technologies,* vol. 13, pp. 1671-1678, 2007.

[51] Y. Zhang, J. Lu, S. Shimano, H. Zhou and R. Maeda, "Development of MEMS-based direct methanol fuel cell with high power density using nanoimprint technology," *Electrochem. Commun.,* vol. 9, pp. 1365-1368, 2007.

[52] T. Sarata, N. Yanase, T. Ozaki, T. Tamachi, K. Yuzurihara and F. Iwasaki, "Method of hydrogen generation, hydrogen generator, and fuel cell apparatus," WO/2006/101214, 2006.

[53] A. V. Pattekar and M. V. Kothare, "A micro reactor for hydrogen production in micro fuel cell applications," *Journal of Microelectromechanical Systems,* vol. 13, pp. 7-18, 2004.

[54] D. Park, T. Kim, S. Kwon, C. Kim and E. Yoon, "Micromachined methanol steam reforming system as a hydrogen supplier for portable proton exchange membrane fuel cells," *Sensors and Actuators A,* vol. 135, pp. 58-66, 2007.

[55] D. Gervasio, S. Tasic and F. Zenhausern, "Room temperature micro-hydrogen-generator," *Journal of Power Sources,* vol. 149, pp. 15-21, 2005.

[56] A. Kundu, J. M. Park, J. E. Ahn, S. S. Park, Y. G. Shul and H. S. Han, "Micro-channel reactor for steam reforming of methanol," *Fuel,* vol. 86, pp. 1331-1336, 2007.

[57] D. Linden, *Handbook of Batteries and Fuel Cells.* New York: McGraw-Hill Companies, 1984.

[58] A. C. Dillon, K. E. H. Gilbert, J. L. Alleman, T. Gennett, K. M. Jones, P. A. Parilla and M. J. Heben, "Carbon nanotube materials for hydrogen storage," in *Proceedings of DOE Hydrogen Program Review,* 2001, .

[59] A. C. Dillon, K. M. Jones, T. A. Bekkedahl, C. H. Kiang, D. S. Bethune and M. J. Heben, "Storage of hydrogen in single-walled carbon nanotubes," *Nature,* vol. 386, pp. 377-379, 1997.

[60] P. Chen, X. Wu, J. Lin and K. L. Tan, "High H_2 Uptake by Alkali-Doped Carbon Nanotubes Under Ambient Pressure and Moderate Temperatures," *Science,* vol. 285, pp. 91-93, 1999.

[61] M. Hirscher, "Hydrogen storage in nanoscale carbon and metals," *Applied Physics A,* vol. 72, 2001.

[62] M. Hirscher, M. Becher, M. Haluska, U. Dettlaff-Weglikowska, A. Quintel, G. S. Duesberg, Y. -. Choi, P. Downes, M. Hulman, S. Roth, I. Stepanek and P. Bernier, "Hydrogen storage in sonicated carbon materials," *Applied Physics*, vol. 72, pp. 129–132, 2001.

[63] M. Hirscher, M. Becher, M. Haluska, A. Quintel, V. Skákalová, Y. M. Choi, Dettlaff-Weglikowska, R. U. S., I. Stepanek, P. Bernier, A. Leonhardt and J. Fink, "Hydrogen storage in carbon nanostructures," *Journal of Alloys Compounds,* vol. 330-332, pp. 654-658, 2002.

[64] A. Züttel, C. Nützenadel, P. Sudan, P. Mauron, C. Emmenegger, S. Rentsch, L. Schlapbach, A. Weidenkaff and T. Kiyobayashi, "Hydrogen sorption by carbon nanotubes and other carbon nanostructures," *Journal of Alloys Compounds,* vol. 330-332, pp. 676-682, 2002.

[65] M. G. Niijkamp, J. E. M. J. Raaymakers, A. J. Van Dillen and K. P. De Jong, "Hydrogen storage using physisorption-materials demands," *Applied Physics A: Materials Science and Processing,* vol. 72, pp. 619-623, 2001.

[66] L. Schlapbach and A. Zuttel, "Hydrogen-storage materials for mobile applications," *Nature,* vol. 414, pp. 353-358, 2001.

[67] A. Zuttel, P. Sudan, P. Mauron, T. Kiyobayashi, C. Emmenegger and L. Schlapbach, "Hydrogen storage in carbon nanostructures," *International Journal of Hydrogen Energy,* vol. 27, pp. 203-212, 2002.

[68] G. Sandrock and G. Thomas, "IEA/DOC/SNL on-line hydride databases," *Applied Physics A,* vol. 72, pp. 153-155, 2001.

[69] Z. Xiong, C. K. Yong, G. Wu, P. Chen, W. Shaw, A. Karkamkar, T. Autrey, M. O. Jones, S. R. Johnson, P. P. Edwards and W. I. F. David, "High-capacity hydrogen storage in lithium and sodium amidoboranes," *Nature Materials,* vol. 7, pp. 138-141, 2008.

[70] V. C. Y. Kong, D. W. Kirk, F. R. Foulkes and J. T. Hinatsu, "Development of hydrogen storage for fuel cellgenerators. i: Hydrogen generation using hydrolysis hydrides," *International Journal of Hydrogen Energy,* vol. 24, pp. 665-675, 1999.

[71] B. R. Flachsbart, K. Wong, J. M. Iannacone, E. N. Abante, R. L. Vlach, P. A. Rauchfuss, P. W. Bohn, J. V. Sweedler and M. A. Shannon, "Design and fabrication of a multilayered polymer microfluidic chip with nanofluidic interconnects via adhesive contact printing," *Lab-on-A-Chip,* vol. 6, pp. 667-674, 2006.

[72] M. Madou, *Fundamentals of Microfabrication.* Boca Raton, Florida: CRC, pp. 200, 1997.

CHAPTER 3:

IMPROVEMENTS ON HYDRIDE-BASED MICRO FUEL CELLS WITH ON-BOARD HYDROGEN SOURCE

3.1. Introduction

Recently, we introduced a new fuel cell architecture that allows fabrication of MFCs in the microliter size range. The enabling technology has been a self-regulating micro hydrogen generator that delivers hydrogen to a membrane electrode assembly (MEA). The hydrogen generator uses a reaction between a metal hydride (e.g. $LiAlH_4$) and water vapor to generate hydrogen in a reactor. A passive microfluidic control mechanism regulates hydrogen generation through controlled delivery of water vapor to the metal hydride based on the reactor pressure. This self-regulating hydrogen generation and delivery system has eliminated the need for auxiliary components such as pumps, valves, sensors, distribution components, and power and control electronics that made fabrication of microliter-scale fuel cells challenging. We have recently reported fabrication of a fully integrated 9 μL MFC that incorporates the hydrogen generation and control mechanism. The device delivered an energy density of approximately 250 WhL^{-1} and a power density of close to 10 WL^{-1}. In this chapter, we studied alternatives for micro fuel cells with higher power density and longer shelf life for transportation and storage.

The content in this chapter is adapted from the published articles as follows;

- S. Moghaddam, E. Pengwang, R.I. Masel, and M.A. Shannon, "An Enhanced Microfluidic Control System for Improving Power Density of a Hydride-based Micro Fuel Cell," *Journal of Power Sources*, vol. 195(7), pp. 1866-1871, 2010.
- E. Pengwang, M.A. Shannon, and S. Moghaddam, "Electrochemically Dissolvable Nanocomposite Seal Layer for Long-term Storage of Chemical Hydride-based Micro Hydrogen Generators," *Journal of Microelectromechanical Systems (JMEMS)*, (submitted October 2011)

Improving the device's power density has been one of the main goals of the recent research. The issue of low hydrogen generation rate have identified due to the limited water vapor release by the microfluidic mechanism that is a cause of low power density (~10 W/L) in the 1st generation device. In this chapter, different parameters that affect the water release rate of the microfluidic mechanism are discussed and the enhanced design that increased the power density of the 2nd generation device by one order of magnitude (~100 W/L) over that of the 1st generation device is introduced.

Moreover, another main challenge for using these metal hydrides is a storage capability because they react spontaneously with any presence of moisture or water. An alternative way to keep water diffusion away from metal hydride is presented in this chapter with a designed seal layer of copper and silver that can be dissolved within a few minutes by a method of electrochemical process. With this development, a seal layer was demonstrated in millimeter integrated fuel cell devices based on metal hydride. This seal layer can be fabricated by micro fabrication processes and thin film deposition that occupies less volume than additional apparatuses in previous methods.

3.2. Modified Micro Fuel Cells

A 3D schematic cross-section of the modified device is shown in Figure 3.1. The device consists of three layers including; (1) water reservoir and vapor release mechanism, (2) hydride reactor, and 3) MEA. Details on the operation principle of the water vapor release mechanism are available in Moghaddam *et al*. [1, 2]. Briefly, during the device operation, water enters the narrow space between the bottom wall of the reservoir and a membrane through an opening. Capillary forces within the membrane holes keep the water from flowing

into the hydride reactor. Water vapor then diffuses into the hydride reactor as shown in the schematic inset in Figure 3.1. Hydrogen is generated when water vapor reacts with the hydride. The generated hydrogen then leaves the hydride reactor through a porous silicon wall (with ~5 nm pore size) at the bottom of the reactor and reaches the MEA. If hydrogen is not used by the MEA (i.e. open-circuit mode), pressure builds up inside the hydride reactor. The membrane is designed to deflect at a pressure less than the capillary forces within the membrane holes. The deflection of the membrane plugs the water port and stops the flow of water from the reservoir. Essentially, the microfluidic control mechanism is a passive valve that automatically regulates hydrogen production based on the hydrogen gas pressure within the hydride reactor.

The water reservoir was fabricated from <100> silicon using a deep reactive ion etching (DRIE) process. The membrane separating the water reservoir and the hydride reactor was made of polyimide (PI) through spinning and curing PI 5878G (HD Microsystems, Parlin, NJ) on a glass substrate. The final thickness of the PI membrane was 5 μm. Since PI is water permeable, the membrane was sputter-coated with a 0.2 μm thick Cr/Au layer to prevent water diffusion through the membrane when the valve is closed. The circularly distributed array of holes shown in Figure 3.1 was etched through the Cr/Au (wet etched) and PI (reactive ion etched) layers. The membrane was transfer-bonded [3] from glass substrate to the bottom of the water reservoir.

The modified hydride reactor was fabricated from <100> p-doped silicon using DRIE process. A 20 μm recess was etched at the bottom of the hydride reservoir facing the MEA to facilitate its assembly on the MEA. The bottom wall of the hydride reactor was then anodized in 25% HF electrolyte to produce ~10 nm diameter pores that allow hydrogen to exit the

reactor. Typically, 60–70% of the hydride reactor is charged with $LiAlH_4$ (Sigma–Aldrich, Inc., St. Louis, MO). $LiAlH_4$ has the highest reaction rate with water vapor among typical chemical hydrides (e.g. CaH_2, $NaAlH_4$, $LiBH_4$, and $NaBH_4$) [4].

The modified MEA was fabricated by sandwiching Nafion® NRE-211 with a nominal thickness of 25 μm (Dupont, Wilmington, DE) between two 25 μm thick stainless steel (SS) foils. The foils have 2 mm × 2 mm square openings to expose Nafion®. The exposed Nafion® membrane was then brush-painted with catalyst. The catalyst was prepared by dispersing platinum black HiSPEC 1000 (Alfa Aesar Co., Ward Hill, MA) in Nafion® solution, Millipore water, and isopropanol via sonication. In addition to the membrane area, a small amount of catalyst ink was also painted on the edges of the SS foil around the membrane to provide electrical connection to the SS foils that are also used as current collectors.

The assembly process of the device was conducted in a glove box. First, the hydride reactor was epoxied to the MEA (Scotch-Weld 2216 B/A Gray epoxy made by 3M Co., St. Pual, MN) to the MEA. The hydride reactor was then partially filled with $LiAlH_4$. Finally, the water reservoir and membrane assembly were assembled on the hydride chamber. The water reservoir was charged with water outside the glove box.

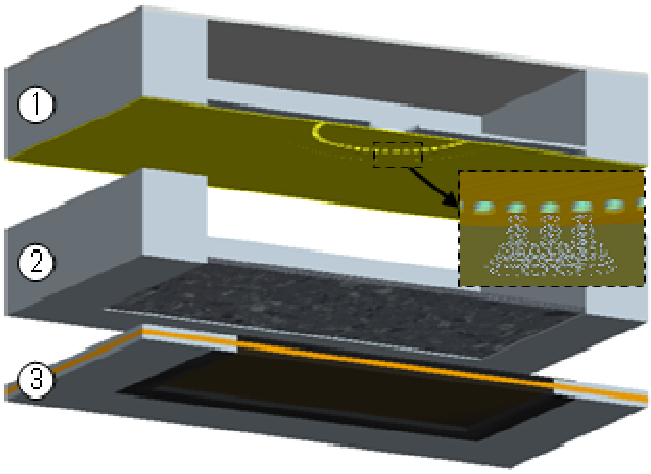

Figure 3.1. Cross-section schematic of the device showing its three main components: 1) water reservoir/valve with a stainless steel (SS) cap, 2) hydride reservoir, and 3) membrane electrode assembly (MEA). The inset schematic shows vapor release from the membrane holes. Total volume of the device is approximately 10 μm.

3.3. Parametric Study of Micro Valves

Performance of the valve is determined by a set of parameters including: gap (H) between membrane when it is not deformed and the bottom of the water reservoir (Figure 3.2a), membrane open area (A) (Figure 3.2b and c), and membrane mechanical properties. Eight test samples were fabricated to study the effects of H and A on the valve water vapor release rate ($\dot{m}$).

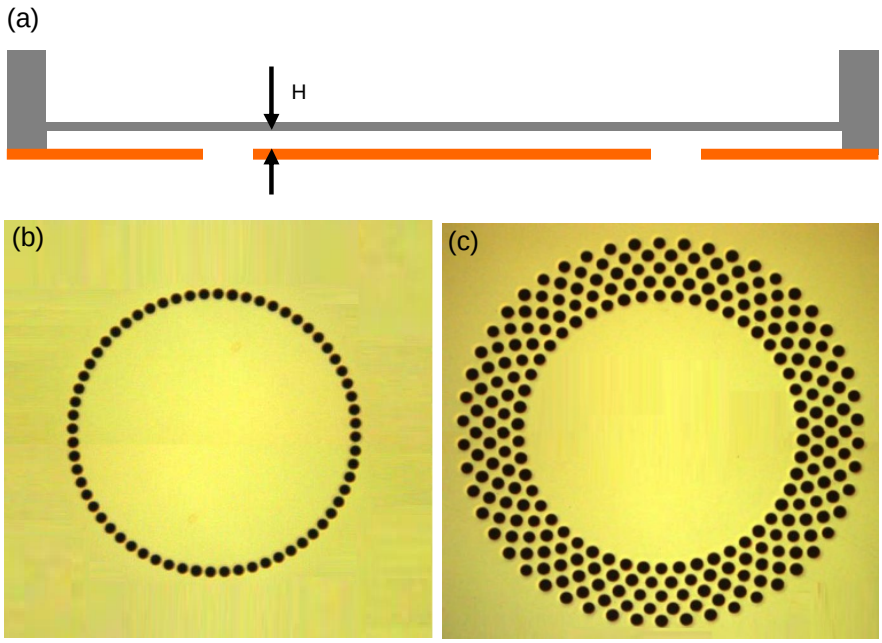

Figure 3.2. Schematic cross section of the valve (a) and front view of the Cr/Au coated PI membrane showing one row (b) and five rows (c) of 30 μm diameter holes.

The experimental setup shown in Figure 3.3 was used to conduct the tests. The setup consists of two main chambers C-1 and C-2. Pressure inside each chamber is adjusted by changing the liquid (Fomblin oil) level in manometers M-1 and M-2. Two push-button valves V-1 and V-2 allow purging of the C-2 chamber with dry nitrogen. A humidity sensor (Model SHT75, size 3.7×2.2×4.9 mm^3, from Sensirion, Inc.) installed on the bottom of the C-2 chamber measures the relative humidity as shown in Figure 3.3. A typical test involves installing the test sample between the C-1 and C-2 chambers. Water is then supplied to the water reservoir (i.e. topside of the valve). The two chambers were kept at the same pressure. The C-2 chamber is purged with nitrogen until a humidity level of less than 1% is reached. Immediately after purging the chamber (i.e. closing the V-1 and V-2 valves), the chamber humidity starts to rise as the valve releases water vapor.

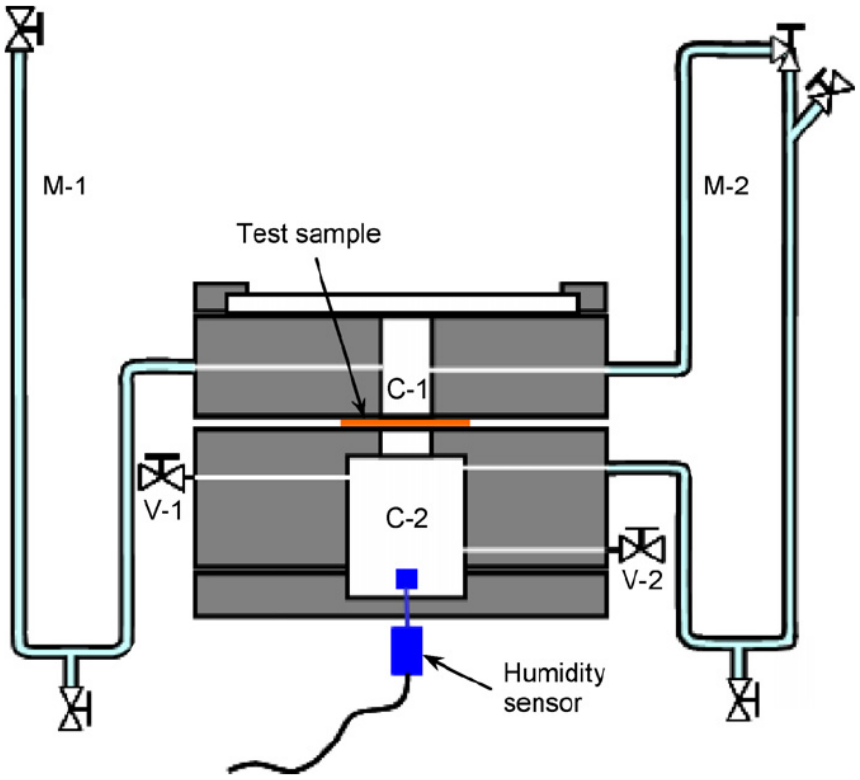

Figure 3.3. Schematic of the test setup for measuring the valve performance. Schematic shows the water chamber and membrane assembly held between the top (C-1) and bottom (C-2) chambers of the setup. Two valves (V-1 and V-2) on the C-2 chamber are used for purging it with dry nitrogen. Two manometers (M-1 and M-2) are used to measure and adjust the pressure in C-1 and C-2 chambers.

Variation of $\dot{m}$, calculated using the measured rise in humidity, is shown in Figure 3.4 and 3.5. Results on valves with constant A (one row of 30 μm diameter holes) and different H (3, 13, 26, and 40 μm) suggest that increasing H greatly enhances $\dot{m}$ at small H. However, the rate of increase declines at higher H values. In the second set of tests (as shown in Figure 3.5), samples with different A (four samples with one row of D = 20, 30, 40, and 50 μm holes and a fifth sample with five rows of D = 30 μm holes) and constant H (40 μm)

were studied. Overall, increasing A enhanced $\dot{m}$. However, the rate of increase when D was constant deviated from a linear trend seen when D was increased from 20μm to 50μm. We believe that this is due to the fact that increasing D reduces the pressure difference ($\Delta p = 2\sigma \cos\gamma / r$) between the two sides of the membrane resulting in an increase in the actual gap between the membrane and the bottom wall of the reservoir. Note that the actual gap between the membrane and the bottom of the water reservoir is not H.

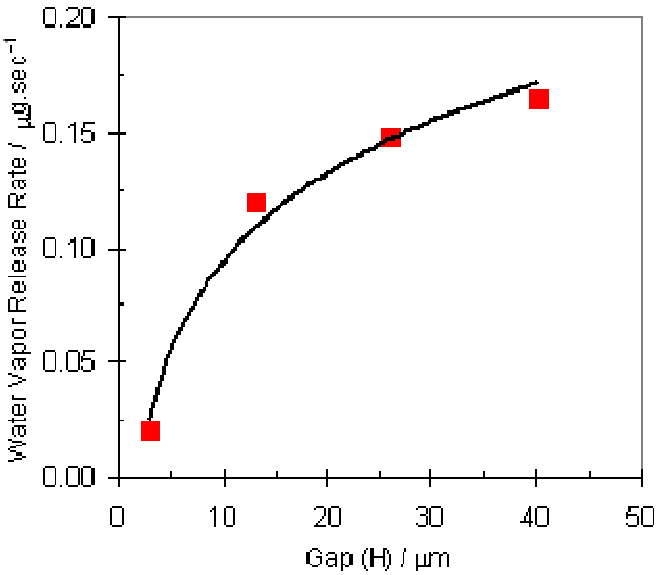

Figure 3.4. Water vapor release rate ($\dot{m}$) of four valves with similar membrane open area (A), one row of D = 30 μm holes, and different spacing between membrane and bottom wall of the water reservoir when the membrane in not deformed (H).

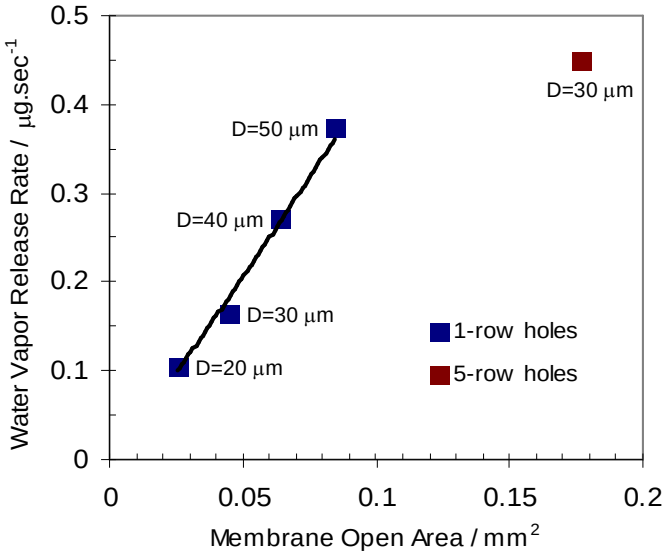

Figure 3.5. Water vapor release rate ($\dot{m}$) of different valves as a function of membrane open area (A) and pore size (D) and H = 40μm.

To measure the hydrogen generation rate of the hydrogen generator (i.e. water reservoir/valve assembly and hydride chamber shown as components 1 and 2 in Figure 3.1), an experimental setup was fabricated (as shown in Figure 3.6). The setup consists of a main SS fixture for holding the hydrogen generator. An opening on top of the fixture, as shown in Figure 3.6a, allows adding water to the water reservoir of the hydrogen generator. The hydrogen exiting the generator (through the porous wall of the hydride reactor) enters a small chamber at the bottom half of the SS fixture that is connected to a plastic Utube filled with Fomblin liquid. The hydrogen generation rate is calculated by measuring the time it takes for the liquid column to rise from point "A" to "B" (in the right leg of the U-tube shown in Figure 3.6c).

To facilitate installation of the hydrogen generator within the main SS fixture, the two components constituting the hydrogen generator were used in their pre-diced form (both part

of 8mm×8mm dies that are later diced to 3mm×3mm when integrated into the final fuel cell, shown in Figure 3.1). The assembly process was conducted in a glove box. First, hydride reactor was partially filled with $LiAlH_4$. Then the water/valve assembly was epoxied (Scotch-Weld 2216 B/A Gray epoxy made by 3M Co., St. Paul, MN) on the hydride chamber. Tests were conducted on hydrogen generators having valves with five rows of D = 30 μm holes and H = 40 μm, intended for use in the fully integrated device. The measured hydrogen generation rate of the samples ranged between 0.44 and 0.49 $\mu L\ s^{-1}$ (as shown in Figure 3.7). This was less than the theoretical value 0.56 $\mu L\ s^{-1}$ calculated using the reaction chemistry between $LiAlH_4$ and water, where $H_2O + 0.25\ LiAlH_4 \rightarrow 0.25\ LiOH + 0.25\ Al(OH)_3 + H_2$ and 0.45 $\mu g s^{-1}$ water vapor release rate of the valve. We believe that increased differential pressure across the valve membrane during the test (due to hydrostatic pressure of the rising liquid column in the U-tube) has contributed to lower hydrogen generation rate. In fact, the liquid column rise was limited to less than 25–30 mm to avoid further differential pressure because a 50–60 mm column of Fomblin yields an overall hydrostatic pressure of about 1 kPa.

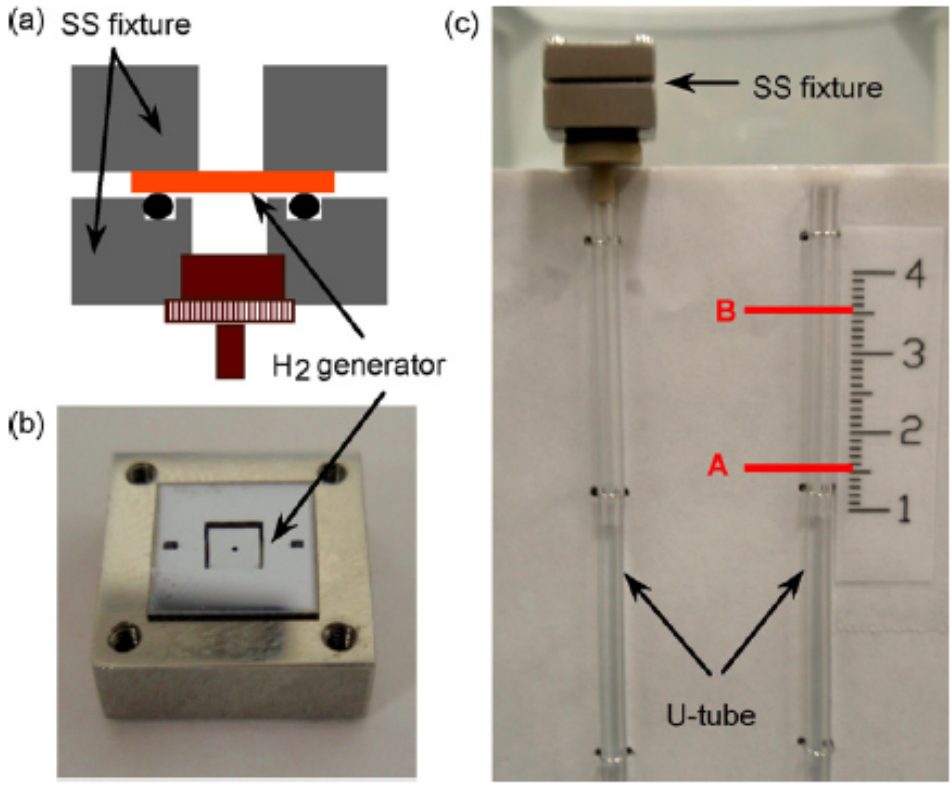

Figure 3.6. Experimental setup for measurement of hydrogen generation rate. (a) Schematic of a stainless steel (SS) fixture holding the hydrogen generator, (b) picture of the hydrogen generator sitting on the bottom part of the SS fixture, and (c) picture of the setup. After the liquid level passes marked level "B", the SS fixture is simply detached from the U-tube to avoid Fomblin liquid exiting the U-tube.

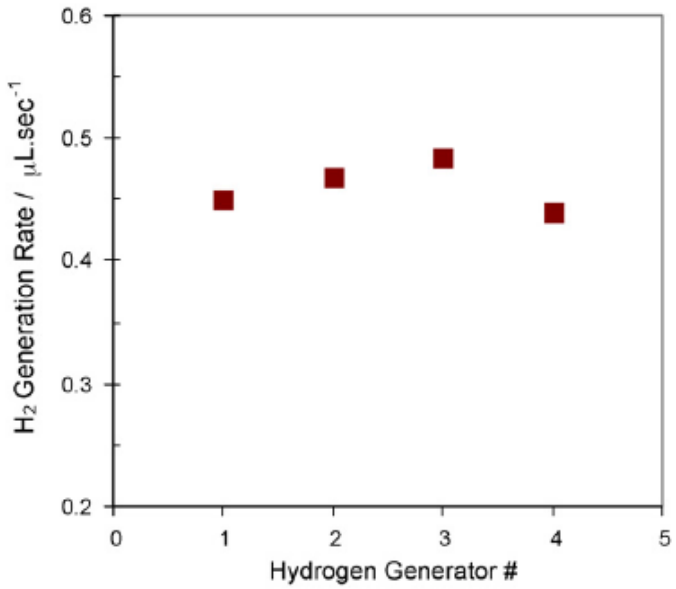

Figure 3.7. Hydrogen delivery rate of four hydrogen generators with valves having five rows of D = 30 μm holes and H = 40 μm.

Since the rate of reaction may be a limiting factor in hydrogen generation, we used Kong et al. [4] data on hydrogen generation rate of $LiAlH_4$ with water vapor for comparison. They measured a hydrogen generation rate of 2.8×10^{-5} mol g^{-1} s^{-1} in a 6.5 mm diameter cylindrical reactor made from nickel mesh. In addition, their data showed a constant hydrogen generation rate up to 60% yield after which the rate started to gradually decline, perhaps due to slower water vapor diffusion through the reaction by-products. The thickness of the hydride bed in our reactor is only ~0.3 mm, thus we do not expect a lower hydrogen generation rate than that measured by Kong et al. [4]. Using their results, we determine a hydrogen generation rate of 3.36×10^{-8} mol s^{-1} (our hydride reactor contains approximately 1.2mg $LiAlH_4$). This is equivalent to 0.76 μL s^{-1} hydrogen generation rate, which is 65% higher than the average 0.46 μL s^{-1} that we have observed in our experiment. This information suggests that the reaction rate is less likely to be the limiting factor.

3.4. Integrated Devices Testing (Second Generation)

The integrated devices were fabricated (Figure 3.8) using valves with five rows of D=30 μm holes and H=40 μm. Tests were conducted in a chamber (Figure 3.9) where humidity was held constant at 60%. Solartron SI 1287 potentiostat was used for operation of the fuel cells. In the first test, a device was operated at a constant voltage of 0.7 V and its output current was measured. As the test results shown in Figure 3.10 suggest, the device delivered a relatively steady current with a peak power density of 92 W/L and an overall energy density of 263 Wh/L. The achieved power density was an order of magnitude higher than the 10 W/L generated in the first generation of the integrated device. However, the output power was significantly lower than the capability of the MEA as well as the on-board hydrogen generation capacity. The output current of the MEA prior to its integration into the device was 4.5mA at 0.7 V operating voltage, which is 3.8 times higher than the 1.18 mA generated by the integrated device. The measured current is equivalent to approximately 0.14 L s^{-1} hydrogen.

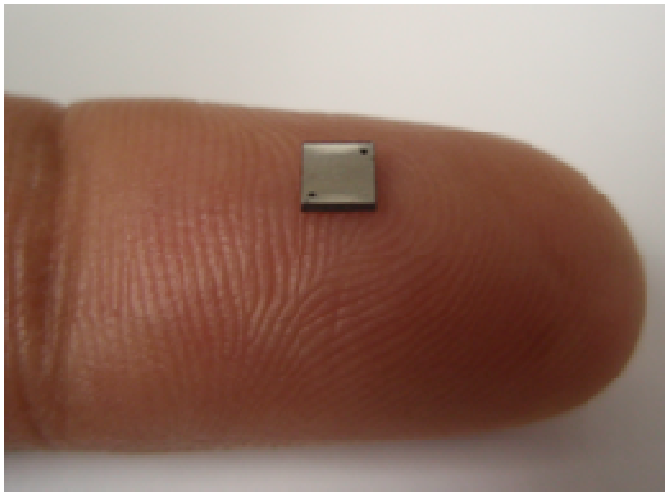

Figure 3.8. Picture of the integrated device.

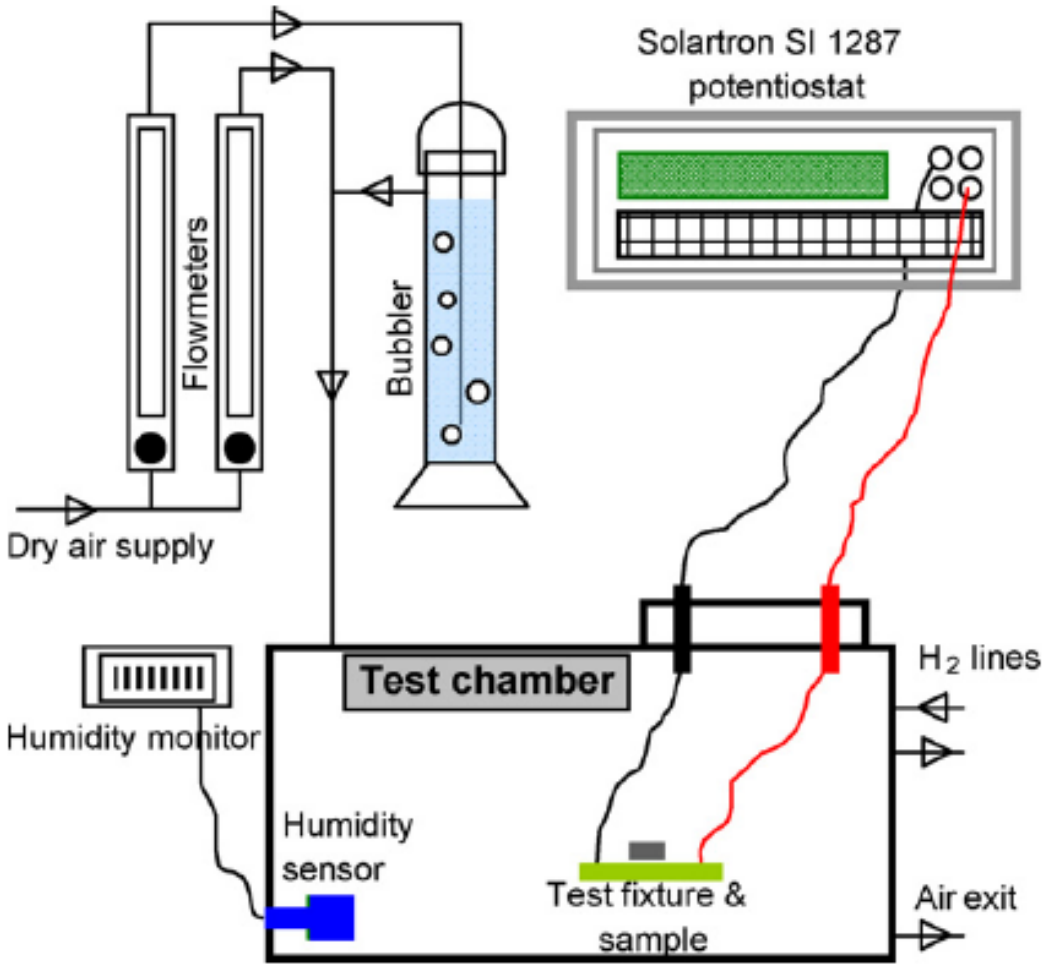

Figure 3.9. Experimental apparatus for testing the MEAs and the integrated devices. Humidity of the test chamber was kept constant at 60% in all tests. Hydrogen lines are used during testing the MEA.

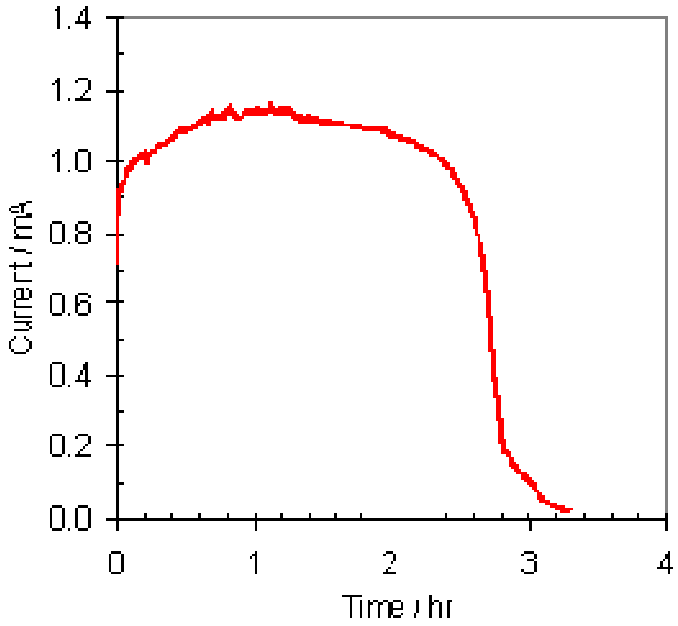

Figure 3.10. Current output of an integrated device (operated at 0.7 V) that incorporates a valve with 5 rows of D=30 μm holes and H=40 μm.

As reported in the previous section, the hydrogen generator can deliver a significantly higher rate of hydrogen than the output current of the integrated device suggests. To determine the cause of the integrated device low performance, I–V characteristic performance of the integrated device was determined. Figure 3.11 and 3.12 show the results and their comparison with the I–V performance of the MEAs before integration. The performance curves clearly suggest that the increase in activation (possibly affected by transport limitations) and/or ohmic polarization losses of the MEA is responsible for the lower current output of the integrated device at high operating voltages (above approximately 0.5 V). However, at lower voltages, the device performance becomes limited by the hydrogen generation rate, as evidenced by the almost constant current output of the device. This limiting current density is approximately 5.2 mA, which corresponds to 0.6 L s^{-1} H_2

generation, slightly higher than what was expected on the basis of a water release rate of 0.45 μgs^{-1}. Overall, the results quite convincingly suggest that the water release rate is limiting the device performance.

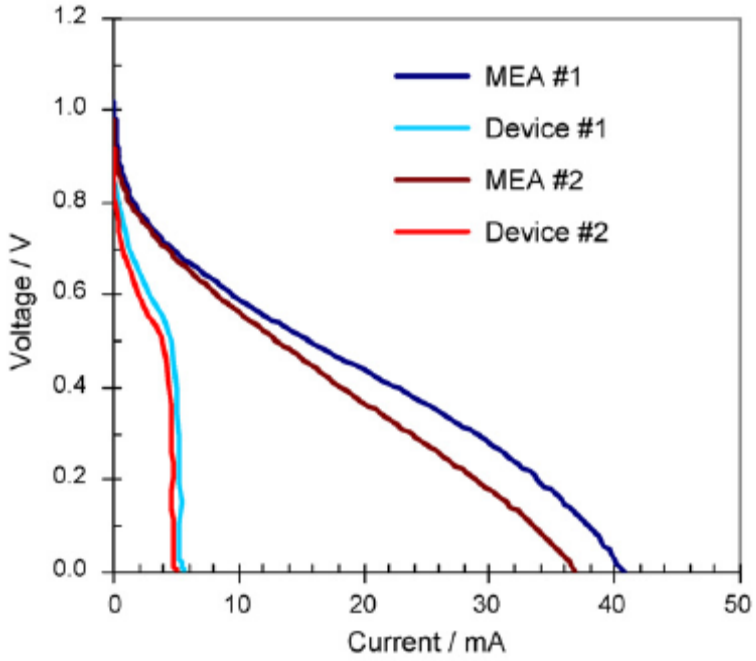

Figure 3.11. Comparison of the MEA performance before and after integration into the fully integrated device.

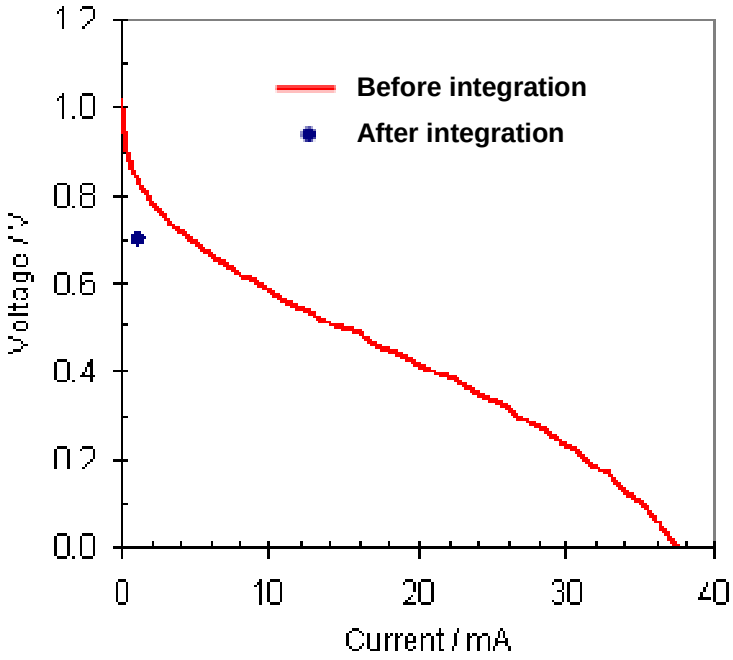

Figure 3.12. Comparison of the MEA performance before and after integration with the fully integrated device.

3.5. Electrochemically Dissolved Seal Layer

In a recent study, we introduced [1, 2, 5] a new fuel cell architecture that allows fabrication of high energy density micro fuel cells (MFCs) in the microliter size range. The device consists of an on-board hydrogen generator and a membrane electrode assembly (MEA). The enabling technology has been a self-regulating micro hydrogen generator that delivers hydrogen to the MFC membrane electrode assembly (MEA). Hydrogen is generated through hydrolysis of a chemical hydride (such as LiH, $LiBH_4$, $LiAlH_4$, and CaH_2) via a rather simple process. These hydrides have been widely considered as a medium for hydrogen storage in different applications [6-18]. An example of hydrolysis process is $LiAlH_4$ reaction with water:

$H_2O + 0.25\ LiAlH_4 \rightarrow 0.25\ LiOH + 0.25\ Al(OH)_3 + H_2$.

The logic behind selection of this hydrogen storage method is thoroughly discussed in Moghaddam *et al.* [1]. Briefly, the method is advantageous with respect to operation at low temperature and pressure, high hydrogen storage density, and the high rate of hydride reaction with water vapor.

Our recent efforts have been focused on enhancing the device energy density (to reach our goal of 1000 W-hr/L), micro- and nanofabrication process development [19], and overcoming challenges of its application. One major challenge has been to prevent slow leakage of water vapor into the hydride reactor through a microfluidic mechanism separating the two reactants. This leakage prevents long-term storage of the device. The objective of this study is to develop a solid layer (or "seal layer") to physically contain water during the storage period. The seal layer should be removed prior to the device operation.

Moreover, it is challenging to maintain a quality of metal hydride that reduces over a period of storage and affects on the fuel cell performances. It was reported that half-life of chemical hydrides can be different at temperature and pH [20]. Most of previous data on micro fuel cells was taken on relatively short runs usually only a few hours after packaging. However, in many of the applications, a device is assumed to operate for days or store for a replacement later. Since metal hydrides often react upon exposure to moist air, hence, maintaining properties of metal hydrides for a longer term test is one of key factors for micro power sources. A preparation of metal hydride as slurry with light mineral oil and dispersion was studied to enhance the stable periods of storage [21]. Modifications of metal hydrides properties are also proposed for ball milling magnesium hydrides [22], coating metal hydrides with metal oxides [23], stabilizing metal hydrides with silicon [24], and using nanocluster of metal hydrides [25] for a better performances and cycle life.

Solid moisture barriers are studied in many applications for chemical and metal hydrides storage. In the past, an alternation of seal layer to prolong a shelf life of power supply included a coating of multilayer of parylene and titanium in case of thin-film lithium or lithium-ion battery [26]. An implementation of polypropylene as a heat-seal layer, aluminum foil as a moisture barrier-layer, and biaxially oriented nylon as a tough moldable layer was also investigated to protect moisture to the battery core [27]. Also, proton conducting ceramics [28] could be used to prevent hydrogenation processes of metal hydride at elevated temperature. Porous thin film of copper was reported for a better performance and cycle life for a nickel/ metal hydride battery by coating on an anode material [29]. Moreover, dielectric barrier layer [30] and a composite of Pd/AlO_x [31] were also candidates to seal the metal hydrides in microsystems and micro power sources.

However, the specific requirements of this application present a unique case. Because of geometrical constraints and material characteristics, mechanical removal of the seal layer is not an option. We have considered electrochemical dissolution of the seal layer to be the only feasible mechanism of its removal. The main considerations in development of an electrochemically dissolvable layer are: 1) microfabrication process compatibility, 2) long-term stability during storage, 3) rapid dissolution prior to use, 4) low dissolution voltage (i.e. less than the fuel cell voltage), and 5) negligible dissolution energy consumption and volume compare to the device energy storage and volume, respectively.

In this study, long-term stability and oxidation/dissolution rate of the candidate metal films deposited through magnetron sputtering process have been studied. The seal layer thickness and its composition have been determined through a trail and error process involving its mechanical stability and the time and energy required for its dissolution. A

microfabrication process has been developed to construct the seal layer on a hole from which water exits the water reservoir. Finally, a fully integrated MFC was constructed and successfully operated after a period of storage.

3.6. Operations

The schematic cross-section of the hydrogen generator provided in Figure 3.13a shows the seal layer on the bottom of the water reservoir preventing water from entering the narrow space above a perforated membrane. Once the seal layer is dissolved, by increasing its voltage potential relative to a stainless steel (SS) lid on the water reservoir, water enters the narrow space. Capillary forces within the membrane holes keep the water from flowing into the hydride reactor. As shown in Figure 3.13b, water vapor diffuses into the hydride reactor. Hydrogen is generated when water vapor reacts with the hydride and leaves the hydride reactor through a porous wall at its bottom. If hydrogen is not used by the MEA (i.e., open-circuit mode), pressure builds up inside the hydride reactor. The membrane is designed to deflect at a pressure (about 200 Pa) less than the capillary forces within the membrane holes. The deflection of the membrane stops the flow of water from the water reservoir (Figure 3.13c). Essentially, this control mechanism is a passive valve that automatically closes when hydrogen is not consumed.

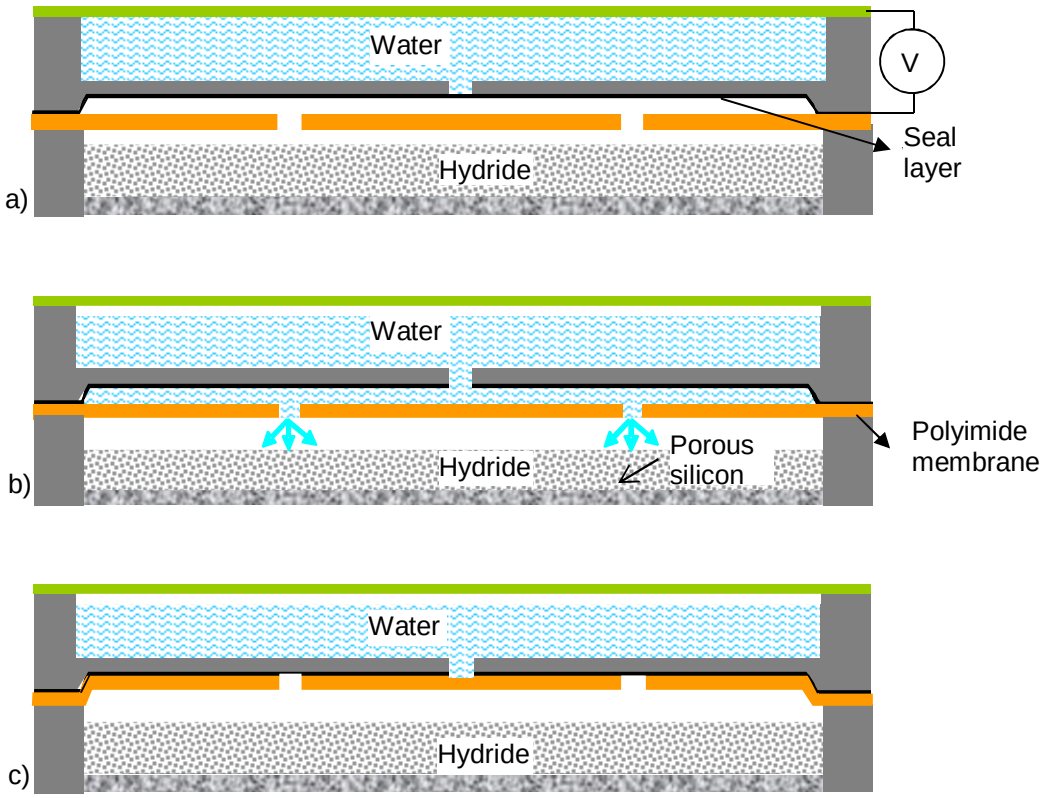

Figure 3.13. Schematic cross section of the water reservoir and fuel chamber assembly showing the device storage and operation modes; a) storage mode: the seal layer prevents water from leaving the reservoir, b) passive valve in open mode: the seal layer is dissolved and water is released, c) passive valve in closed mode: the valve membrane is deformed due to high reactor pressure and water flow is stopped.

A. Dissolution Voltage

As mentioned earlier, there are a number of considerations in development of the seal layer with the primary one being a dissolution voltage of less than 0.8-0.9 V. While a slightly higher voltage can be used as long as it does not lead to water electrolysis, the need for dissolving the seal layer using the MEA output limits the voltage. This is essential when a device uses an array of micro hydrogen generators with seal layers that are not opened

simultaneously using an external power source. The theoretical voltage of a hydrogen fuel cell (i.e. the difference between reduction and oxidation half-cells) is 1.23 V. The open circuit potential (OCP) achieved in our device is approximately 1 V and operation at voltages lower than OCP is required to achieve a reasonable output current.

B. Material Selection

The need for stability of the seal layer, when no voltage is applied, limits the choice of metals to Cu and more noble metals such as Ag, Pt, and Au. Table 3.1 lists the standard oxidation-reduction potential of these metals. In an aqueous electrolyte with near zero redox potential, a positive voltage of equal or greater than the listed values in Table 3.1 is required to significantly increase the metal oxidation rate. As the data in Table 3.1 suggest, considering the available voltage of 0.8-0.9 V, the only viable choices are Cu and Ag. In the case of Ag, the available voltage marginally suffices, if little or no voltage drop across the electrolyte and the electrolyte/cathode interface is encountered. To mitigate the voltage drop effect, the water reservoir cap is entirely made of stainless steel (SS) to constitute a two orders of magnitude surface area difference between the anode (i.e. the seal layer) and the cathode (i.e. the SS lid). The voltage drop within the electrolyte could be reduced by increasing the electrolyte concentration.

Therefore, a material for seal layer is restricted to the voltage region that it remains immunity in the solution at no voltage supply and starts to corrode when a voltage is applied. Pourbaix diagrams presenting stable phases of materials in aqueous electrochemical system are studied for this corrosion, passivation, and immunity region at different pH [32]. Example

of materials with this corrosion phenomenon at 25°C for different pH and voltage difference are copper and silver, as shown in Figure 3.14a-b.

Table 3.1: Standard oxidation-reduction potentials of some of the microfabrication compatible metals

Materials	**Electrochemical**	**E° (V)**
Gold	$Au \rightarrow Au^{3+} + 3e^{-}$	-1.50
Platinum	$Pt \rightarrow Pt^{2+} + 2e^{-}$	-1.18
Silver	$Ag \rightarrow Ag^{+} + e^{-}$	-0.80
Copper	$Cu \rightarrow Cu^{2+} + 2e^{-}$	-0.34
Chromium	$Cr \rightarrow Cr^{2+} + 2e^{-}$	+0.74
Titanium	$Ti \rightarrow Ti^{2+} + 2e^{-}$	+1.63
Aluminum	$Al \rightarrow Al^{3+} + 3e^{-}$	+1.66

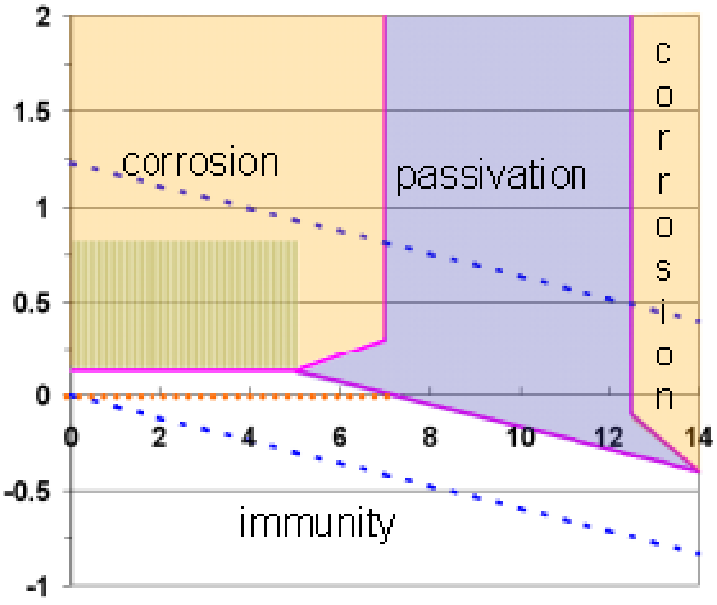

(a)

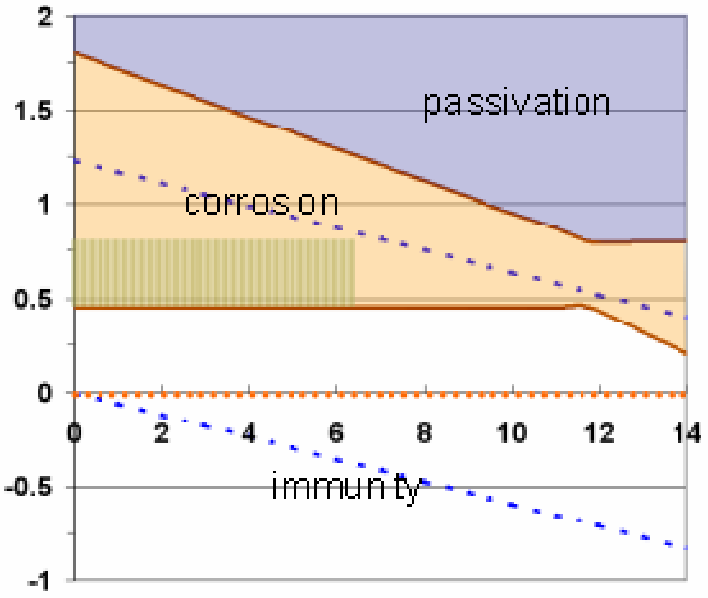

(b)

Figure 3.14. Region of corrosion phenomenon at 25 °C for copper **(a)** and silver **(b)**: orange lines for preferred ambient storage condition and green-shade area for an interested corrosion region.

3.7. Material Characterization

A preliminary study was conducted on mechanical stability of thin Cu and Ag membranes fabricated over the 300-micron diameter opening of the water reservoir bottom wall (Figure 3.15) using magnetron sputtering process. The study suggested that an approximately 0.5-µm-thick membrane could withstand the subsequent fabrication and assembly processes and the hydrodynamic forces during the water reservoir charging process. After successful demonstration of the membrane mechanical stability, a set of electrochemical tests were conducted to determine the time required for dissolving the membrane. The initial tests were conducted on metal films deposited on a silicon wafer electrically insulated by a silicon nitride layer. A test platform was fabricated by bonding a Polydimethylsiloxane (PDMS) layer with through holes over the thin metal film. The PDMS layer was fabricated using a molding process and then activated with O_2 plasma for 2 minutes and attached to the metal layer. Figure 3.16 and Figure 3.17 shows a schematic cross-section and actual samples for the test cells.

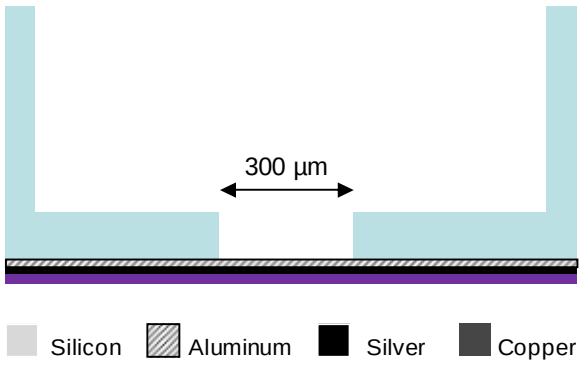

Figure 3.15. A schematic cross section showing the seal layer on the 300-µm-diameter hole of the water chamber hole.

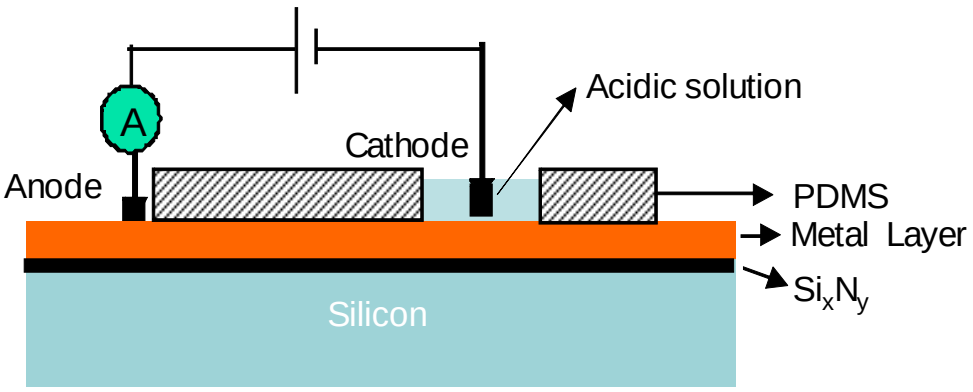

Figure 3.16. Test set up for measurement of the thin metal films dissolution rate.

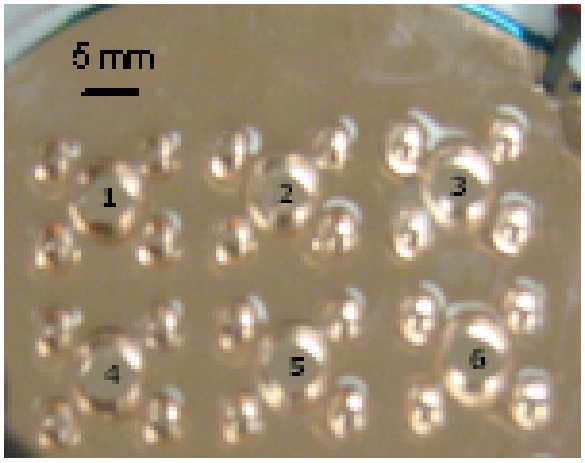

Figure 3.17. Actual samples of copper on test set up

The cells were filled with sulfuric acid electrolytes of different pH values and tested separately. A typical test started with inserting a SS electrode inside the cell and applying a DC potential between the metal film (i.e. anode) and the SS electrode (i.e. cathode). A constant voltage of 0.8 V was applied between the electrodes and the current was monitored. The current was relatively constant during the process and rapidly declined to near zero when the entire thickness of the thin metal layer was dissolved away. Figure 3.18 shows the dissolution rate of the 1µm-thick Cu films as a function of the electrolyte pH. As the data

suggest, in a pH=2 solution the current density and the dissolution rates are approximately 0.1 mA/cm^2 and 1 µm/min, respectively. Tests on Ag thin films at an applied voltage of 0.8 V in a pH=2 solution resulted in a dissolution rate of approximately 0.12 µm/min. As the results suggest, the dissolution rate of Ag is significantly less than that of Cu at similar test conditions. This was expected considering the higher redox potential of Ag versus Cu.

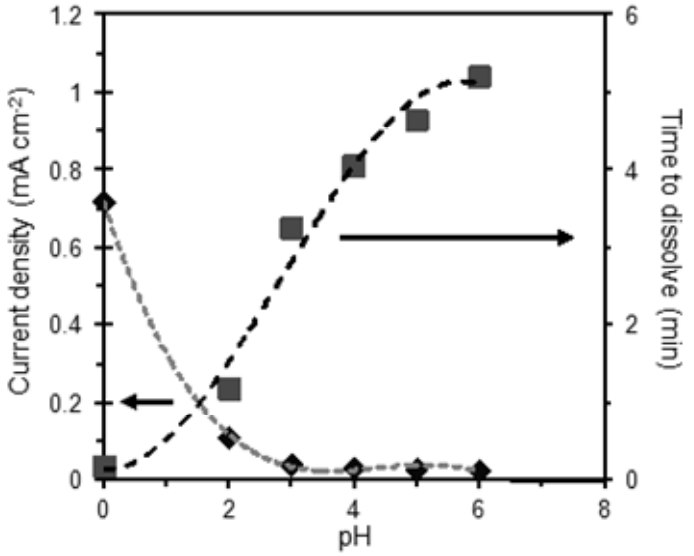

Figure 3.18. Current density and time to dissolution of Cu thin film at different pH solutions.

Another important parameter affecting the membrane material selection was its stability during the device storage. To study this parameter, several water reservoirs were fabricated and filled with different pH solutions. The packaging and water charging procedure will be discussed in the device assembly section. The packages were stored at room conditions and were weighted frequently to determine their weight loss. The membrane rupture was confirmed by a sudden change in the package weight and visual inspections. Table 3.2 provides a summary of the results. The results clearly suggest that a device with Cu seal layer does not have a meaningful shelf life and an Ag membrane remains stable at high electrolyte concentrations.

Table 3.2: Shelf life and dissolution activity of different seal layers

Materials	**pH**	**Shelf life**	**Dissolution activity @ 0.8V**
Copper (1-μm-thick)	2 6	1-2 days 7-8 days	0.1 mA/cm^2 for 1 minute 0.02 mA/cm^2 for 5 minute
Silver (0.4-μm-thick)	2	>30 days	0.04 mA/cm^2 for 4 minutes
Aluminum/Silver/Copper (100 nm/ 100 nm/ 300 nm)	2	>14 days	0.15 mA/cm^2 for 3 minutes

Considering the long dissolution time of an Ag membrane, we decided to construct a composite Cu/Ag membrane with a relatively thin Ag film protecting a thicker Cu layer. Details of the fabrication process are discussed in the following section.

3.8. Microfabrication Processes for Seal Layer

A. Seal Layer and Membrane-Water Reservoir Assembly

A p-doped <100> silicon wafer with a nominal thickness of 500 μm and a 0.5-μm-thick silicon nitride layer deposited through low-pressure chemical vapor deposition (LPCVD) process was used to fabricate the seal layer and membrane-water reservoir assembly. Figure 3.19 shows the microfabrication sequence. First, a 2.4×2.4-mm^2 square area on one side of the wafer was patterned and the silicon nitride layer was removed using the reactive ion etching (RIE) process. The wafer was subsequently etched in a 30% KOH solution at 85°C until an etch depth of 40 μm (Figure 3.19a) was reached. The silicon nitride layer served as the protection mask. Then, a 2.7×2.7-mm^2 opening on the opposite side of the wafer was patterned and the silicon nitride layer was etched using the RIE process. The silicon was subsequently etched to a depth of 420 μm (Figure 3.19b) using inductively coupled plasma deep reactive-ion etching (ICP-DRIE) process. The resulting 0.42×2.7×2.7-mm^3 volume constitutes the water reservoir. Attachment of the membrane on the 40-μm-deep recess, as will be discussed shortly, forms the vapor release control mechanism (i.e. the passive valve).

The next step was to fabricate the seal layer and the hole connecting the water reservoir to the passive valve. First, an 80-nm-thick layer of aluminum (Al) was deposited on the 40-μm-deep recess using RF plasma sputtering process. The Al film was patterned and

etched to create a 350-μm-diameter circular area (Figure 3.19c-d) at the center of the recess. The composite seal layer was subsequently built on the Al layer through deposition of 100 nm Ag and 300 nm Cu using the RF plasma sputtering deposition process (Figure 3.19e). Then, a 300-μm-diameter hole was patterned and etched on the bottom wall of the water reservoir (aligned with the Al layer on the opposite side of the wall) (Figure 3.19f). The Al layer protected Ag and prevented the ICP-DRIE reaction chamber contamination due the exposure of a non-aluminum metal to plasma once the etched silicon hole reaches the multilayer metal film (note that the DRIE process chamber and wafer holder are made of Al). The Al layer rapidly dissolves in the low pH solution.

(a) Pattern and RIE etch Si_xN_y and KOH etch silicon

(b) Pattern and RIE etch Si_xN_y and ICP-DRIE etch silicon

(c) Sputter deposit 100 nm aluminum

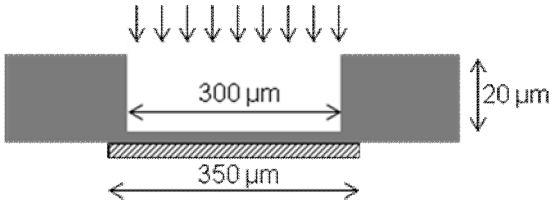

(d) Pattern main gate and ICP-DRIE

(e) Sputtering deposit 100 nm silver and 300 nm copper

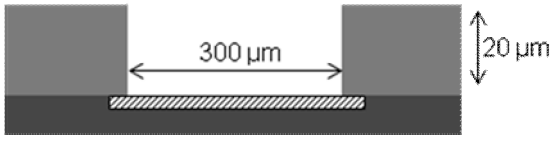

(f) Pattern main gate and ICP-DRIE

Figure 3.19. Microfabrication sequence of the seal layer and water reservoir.

The membrane was fabricated using a similar process discussed in Moghaddam *et al.* [2]. Briefly, the membrane was made through spin coating and baking of polyimide PI-5878 (from HD MicroSystems, Wilmington, DE) on a glass substrate. The final thickness of the membrane was 5 µm. The PI layer was then sputter-coated with a 0.2-µm thick Au layer. A 150 Å Cr adhesion layer was used beneath the Au layer. Finally, instead of the single-row array 30-µm-diameter holes discussed in Moghaddam *et al.* [5], a 5-row-array of similar size holes (Figure 3.20) was made to enhance the valve water release rate. The membrane was transfer-bonded onto the backside of the water reservoir using a process discussed in Moghaddam *et al*. [2]. Figure 3.21 shows a schematic of the assembly.

Finally, in order to access the seal layer for electrical connection, the polyimide layer on one edge of the device, outside the membrane area (Figure 3.20), was etched in a reactive ion etcher (RIE) using a 3:1 ratio of O_2 and Ar gasses at 250 W. A 100-µm-thick PDMS film was used to mask the rest of the membrane.

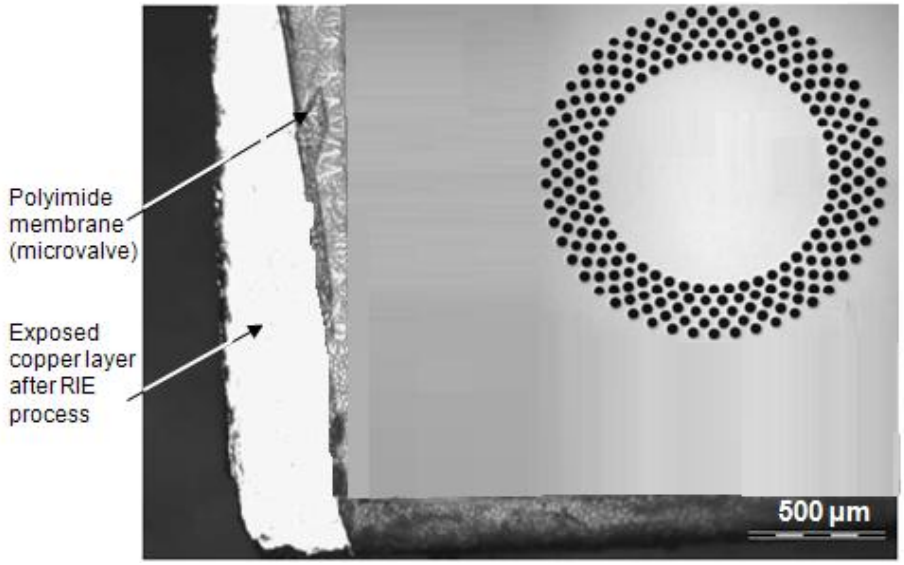

Figure 3.20. Front image of the passive valve showing a side of the seal layer exposed for electrical connection.

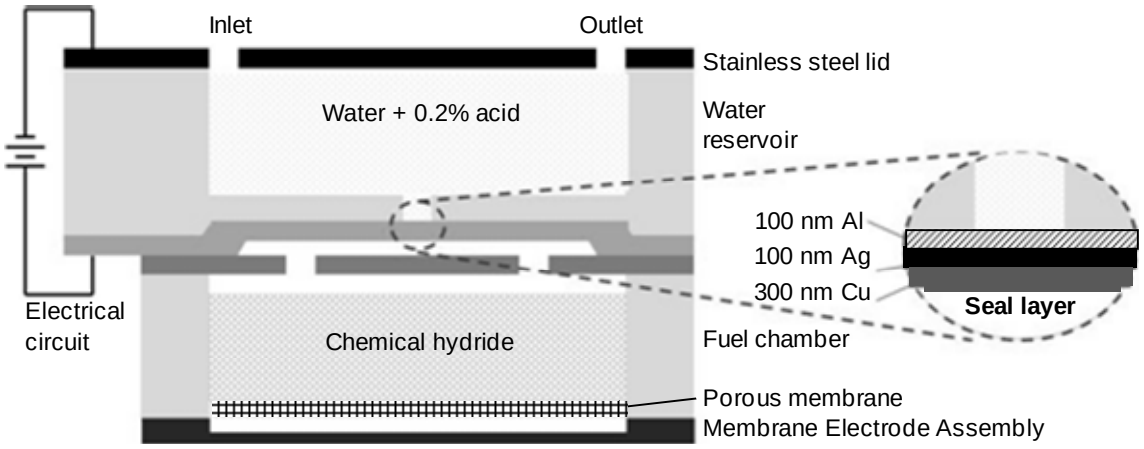

Figure 3.21. Schematic cross-section of the entire fuel cell assembly with a close view of the seal layer.

B. Fuel Reservoir

The fuel chamber was made on a p-doped <100> silicon wafer with a nominal thickness of 500 μm. As shown in the schematic Figure 3.21, 2.5×2.5-mm^2 square areas were patterned and etched using ICP-DRIE process on the two sides of the wafer. The main fuel container and a recess on its backside were etched 450 μm and 20 μm, respectively. The wall separating these two volumes was made porous using a process discussed in Moghaddam *et al.* [2]. The porous wall allows the generated H_2 to reach the membrane electrode assembly (MEA).

C. Membrane Electrode Assembly (MEA)

The MEA was fabricated by sandwiching a Nafion® NRE-211 membrane (with a thickness of 25 μm) between two stainless steel (SS) foils. The SS foils were 25-μm-thick and had 2×2-mm^2 square openings to expose the membrane. The two sides of the membrane were painted with a Pt-based catalyst mixture (Figure 3.22). The catalyst constituents and its preparation process are described in Moghaddam *et al.* [2].

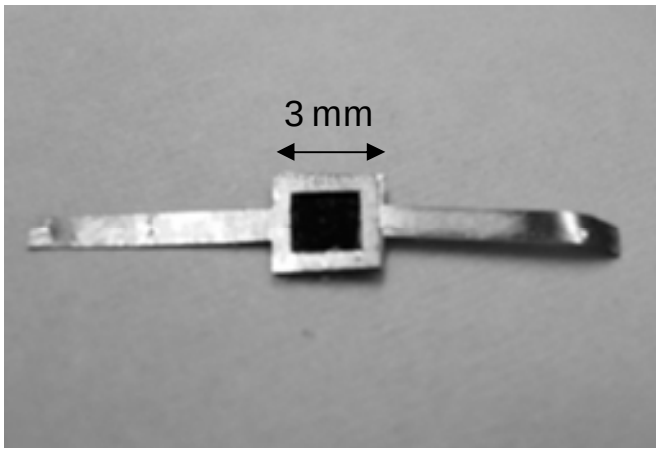

Figure 3.22. Image of the membrane electrode assembly (MEA).

3.9. Device Assembly

The water reservoir and membrane assembly was cut at an overall size of 3×3.4 mm^2 from a larger die using a laser cutting machine. The 0.4-mm-wide extension (Figure 3.21) beyond the 3×3 mm^2 square water reservoir and the passive valve area was designed to provide electrical access to the seal layer. The SS lid was attached on the water reservoir using Scotch-Weld 2261 B/A Gray epoxy (3M, Inc., St. Paul, MN). This epoxy is electrically nonconductive. The SS lid has two 250-μm-diameter holes (Figure 3.23) made to facilitate charging the water reservoir. The reservoir was filled (with water and 0.2% by volume sulfuric acid (pH=2) that has also been shown to improve the reaction kinetics [33]) from one of the holes using a syringe with a flexible capillary needle while the other hole allowed air to vent. Note that the internal surface of the water reservoir was hydroxylated prior to the membrane assembly to make it highly hydrophilic. The device was weighted to verify that it is fully charged. The lid holes were sealed using small drops of Scotch-Weld 2261 B/A Gray epoxy. A silver-filled conductive epoxy (CircuitWorks®, Kennesaw, GA) was used to connect two fine wires to the exposed area of the seal layer (i.e. the 0.4-mm-wide extended area) as well as the SS lid.

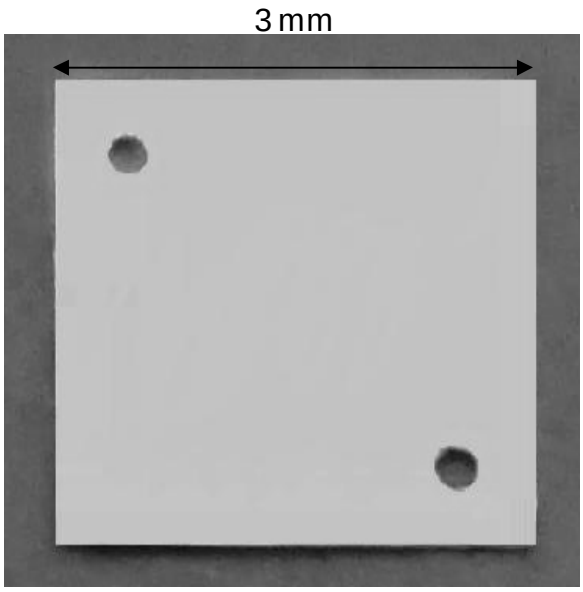

Figure 3.23. Image of a stainless steel cap.

The fuel reservoir was assembled on the MEA using Scotch-Weld 2261 B/A Gray epoxy. The rest of the device assembly process was conducted in a glovebox. First, approximately 60% of the hydride reactor volume was filled with $LiAlH_4$ powder (from Sigma-Aldrich, Inc., St. Louis, MO). $LiAlH_4$ was selected because of its high reaction rate with water vapor. The water reservoir assembly was then attached onto the hydride reservoir using the Scotch-Weld 2261 B/A Gray epoxy. The devices were stored in the glovebox for approximately 30 days.

3.10. Test Results and Discussion

A Solartron SI 1287 potentiostat was used to conduct the tests. The integrated device was installed in a test stand that connected anode and cathode electrodes of the MEA to the potentiostat. A typical test started by application of 0.8 V between the seal layer and the water chamber SS lid. This was achieved by connecting the seal layer and the SS lid wires to

positive and negative polarities, respectively, of a DC power supply. Several devices were tested to evaluate; 1) time to seal layer rupture and 2) life tests to determine the device energy density. Figure 3.24 exemplifies the seal layer dissolution event during which the device output current rapidly rises up within a few minutes after application of the 0.8 V potential. The power and energy required for the seal layer dissolution was 24 µW and 1.2 µW·hr respectively, which is negligible (~0.04%) compare to the device output energy. This clearly suggests that in applications implementing an array of these cells the fuel cells can readily supply the required power and energy to dissolve the seal layer of the their neighboring cell.

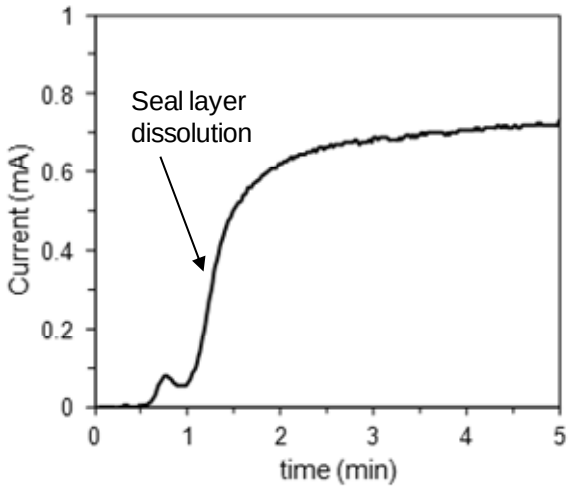

Figure 3.24. Current output at the beginning of the test illustrating the seal layer dissolution/breakup.

The test machine was set to maintain the device output voltage at 0.7 V (the applied load to the device is automatically adjusted). The device output current reaches a maximum of about 1 mA. Figure 3.25 shows a typical test result. Over time, however, the current

decreased. We suspect this is due to reduction in hydrogen generation rate over time. One explanation could be a decrease in the water vapor rate reaching the unreacted fuel at the bottom of the hydride reactor, as thickness of the reaction products gradually increased.

The results shown in Figure 3.25 correspond to an energy density of 265 W·h/L, calculated by dividing the overall generated energy (integral of the generated power reported in Fig. 11) by the device volume. Also, the device delivered a maximum power density of 45 W/L. Considering that the hydride reactor was filled with 1.6 mg of $LiAlH_4$ (60% of the 3 μL reactor volume) that could generate hydrogen for 6.2 mW·h energy (or 522.2 W·h/L) at an operating voltage of 0.7 V, suggested that only about 51% of the fuel was utilized in the device. The rest of the fuel could have either stayed unreacted in the reactor or the generated hydrogen leaked from the device through the adhesives that may not be hydrogen impermeable. Further studies are required to quantify and minimize these losses.

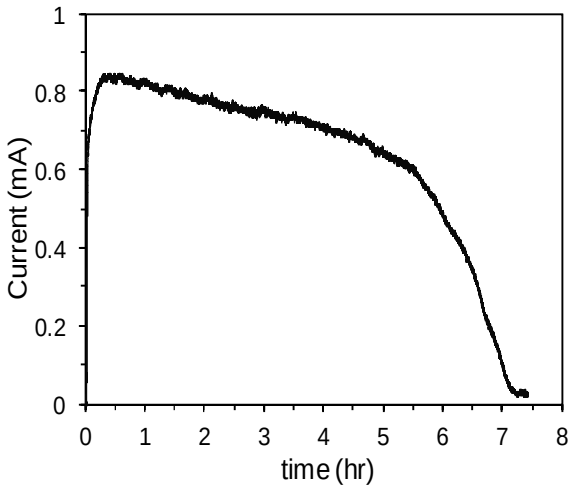

Figure 3.25. Current output of the integrated device operated at a constant voltage of 0.7 V.

Also, our calculation suggests that using the following reaction, a theoretical energy density of 756 W·h/L at the operating voltage of 0.7 V (or 863 W·h/L at 0.8 V) could be achieved:

$H_2O + 0.55\ NH_4F + 0.8\ LiBH_4 \rightarrow 0.55\ LiF + 0.55\ BN + 0.25\ LiOH + 0.25\ H_3BO_3 + 3.2\ H_2$

One challenge with this reaction is formation of compounds that are often impermeable to water vapor. If this issue is resolved, an energy density on the order of 700 W·h/L can be achieved through implementation of this chemistry.

Moreover, the volume of the extension on silicon dominated the volume of this seal layer, while the total volume of only seal layer was less than 0.05% of the integrated device. This extension area of 400 μm on the side providing some space for misalignment in this integrated device could be improved for smaller area. Hence, the designed seal layer is not only practical for metal hydride, but also the storage of water or solution for microfluidic systems and applications. In this project, approximately 1 μL (1mg) of solution is kept inside the chamber without any loss or diffusion. With this purposed seal layer, microsystems can be enhanced by the storage of solution inside the device.

3.11. Conclusion

An electrochemically dissolvable seal layer was developed for a microliter-scale fuel cell with an on-board hydrogen source and control system. The seal layer is a composite layer of 100 nm Ag, and 300 nm Cu. This development has enabled the device storage more than 30 days without any measurable degradation in volumetric energy density. The seal layer was successfully dissolved within a few minutes using an applied voltage of 0.8 V. The power and energy required for dissolution of the seal layer was negligible (i.e. 0.11 W·h/L of

the entire device volume or 0.04% of the generated energy density of the entire device). Addition of the seal layer increased the device volume by only 0.7 mm^3 (approximately 7% of the total device volume), which was mainly due to the area required for the electrical connection. Devices incorporating the seal layer were successfully operated and delivered an energy density comparable to that of the previous generation. The added volume due to the seal layer was compensated for through reduction in the dead volume of the other device elements via improvements in manufacturing processes.

3.12. References

[1] S. Moghaddam, E. Pengwang, K. Y. Lin, R. I. Masel and M. A. Shannon, "Millimeter-scale fuel cell with onboard fuel and passive control system," *Journal of Microelectromechanical Systems,* vol. 17, pp. 1388-1395, 2008.

[2] S. Moghaddam, E. Pengwang, R. Masel and M. Shannon, "A self-regulating hydrogen generator for micro fuel cells," *Journal of Power Sources,* 2008.

[3] B. R. Flachsbart, K. Wong, J. M. Iannacone, E. N. Abante, R. L. Vlach, P. A. Rauchfuss, P. W. Bohn, J. V. Sweedler and M. A. Shannon, "Design and fabrication of a multilayered polymer microfluidic chip with nanofluidic interconnects via adhesive contact printing," *Lab-on-A-Chip,* vol. 6, pp. 667-674, 2006.

[4] V. C. Y. Kong, F. R. Foulkes, D. W. Kirk and J. T. Hinatsu, "Development of hydrogen storage for fuel cell generators. i: Hydrogen generation using hydrolysis hydrides," *Int. J. Hydrogen Energy,* vol. 24, pp. 665-675, 1999.

[5] S. Moghaddam, E. Pengwang, R. I. Masel and M. Shannon, "An enhanced microfluidic control system for improving power density of a hydride-based micro fuel cell," *J. Power Sources,* vol. 195, pp. 1866-1871, 4/2, 2010.

[6] S. C. Amendola, S. L. Sharp-Goldman, M. S. Janjua, M. T. Kelly, P. J. Petillo and M. Binder, "An ultrasafe hydrogen generator: aqueous, alkaline borohydride solutions and Ru catalyst," *J. Power Sources,* vol. 85, pp. 186-189, 2000.

[7] S. C. Amendola, S. L. Sharp-Goldman, M. S. Janjua, N. C. Spencer, M. T. Kelly, P. J. Petillo and M. Binder, "A safe, portable, hydrogen gas generator using aqueous borohydride solution and Ru catalyst," *Int. J. Hydrogen Energy,* vol. 25, pp. 969-975, 2000.

[8] S. G. Chalk and J. F. Miller, "Key challenges and recent progress in batteries, fuel cells, and hydrogen storage for clean energy systems," *J. Power Sources,* vol. 159, pp. 73-80, 2006.

[9] Y. Kojima, K. Suzuki, K. Fukumoto, Y. Kawai, M. Kimbara, H. Nakanishi and S. Matsumoto, "Development of 10 kW-scale hydrogen generator using chemical hydride," *J. Power Sources,* vol. 125, pp. 22-26, 2004.

[10] J. M. Moore, J. B. Lakeman and G. O. Mepsted, "Development of a PEM fuel cell powered portable field generator for the dismounted soldier," *J. Power Sources,* vol. 106, pp. 16-20, 2002.

[11] S. Orimo, Y. Nakamori, J. R. Eliseo, A. Zuttel and C. M. Jensen, "Complex hydrides for hydrogen storage," *Chem. Rev.*, vol. 107, pp. 4111-4132, 09/12/, 2007.

[12] A. S. Patil, T. G. Dubois, N. Sifer, E. Bostic, K. Gardner, M. Quah and C. Bolton, "Portable fuel cell systems for America's army: technology transition to the field," *J. Power Sources,* vol. 136, pp. 220-225, 2004.

[13] L. Schlapbach and A. Zuttel, "Hydrogen-storage materials for mobile applications," *Nature,* vol. 414, pp. 353-358, 2001.

[14] Q. D. Wang, C. P. Chen and Y. Q. Lei, "The recent research, development and industrial applications of metal hydrides in the People's Republic of China," *J. Alloys Compd.*, vol. 253-254, pp. 629-634, 1997.

[15] C. Wu, H. Zhang and B. Yi, "Hydrogen generation from catalytic hydrolysis of sodium borohydride for proton exchange membrane fuel cells," *Catalysis Today*, vol. 93-95, pp. 477-483, 2004.

[16] A. Züttel, P. Wenger, S. Rentsch, P. Sudan, P. Mauron and C. Emmenegger, "$LiBH_4$ a new hydrogen storage material," *J. Power Sources*, vol. 118, pp. 1-7, 2003.

[17] A. Züttel, "Hydrogen storage methods," *Naturwissenschaften*, vol. 91, pp. 157-172, 2004.

[18] O. J. Adlhart, P. Rohonyi, D. Modroukas and J. Driller, "A small portable proton exchange membrane fuel cell and hydrogen generator for medical applications," *Am. Soc. Art. Int. Org.*, vol. 43, pp. 214-219, 1997.

[19] S. Moghaddam, E. Pengwang, Y. Jiang, A. R. Garcia, D. J. Burnett, C. J. Brinker, R. I. Masel and M. A. Shannon, "An inorganic-organic proton exchange membrane for fuel cells with a controlled nanoscale pore structure," *Nature Nanotechnology*, vol. 5, pp. 230-236, 2010.

[20] B. S. Richardson, J. F. Birdwell, F. G. Pin, J. F. Jansen and R. F. Lind, "Sodium borohydride based hybrid power system," *J. Power Sources*, vol. 145, pp. 21-29, 7/4, 2005.

[21] A. W. McClaine, R. W. Breault, C. Larsen, R. Konduri, J. Rolfe, F. Becker and G. Miskolczy, "Hydrogen transmission/storage with metal hydride-organic slurry and advanced chemical hydride/hydrogen for PEMFC vehicles," *Proceedings of the 2000 US DOE Hydrogen Program Review NREL/CP-570-28890,* 2000.

[22] J. Huot, G. Liang, S. Boily, A. V. Neste and R. Schulz, "Structural study and hydrogen sorption kinetics of ball-milled magnesium hydride," *J. Alloys Compd.,* vol. 293-295, pp. 495-500, 1999.

[23] Y. Kojima, K. Suzuki, K. Fukumoto, M. Sasaki, T. Yamamoto, Y. Kawai and h. Hayashi, "Hydrogen generation using sodium borohydride solution and metal catalyst coated on metal oxide," *Int. J. Hydrogen Energy,* vol. 27, pp. 1029-1034, 2002.

[24] J. J. Vajo, F. Mertens, C. C. Ahn, R. C. Bowman and B. Fultz, "Altering hydrogen storage properties by hydride destabilizatioon through allow formation: LiH and MgH2 Destablized with Si," *J. Physical Chemistry B,* pp. 13977-13983, 2004.

[25] A. Zaluska, L. Zaluski and J. O. Strom-Olsen, "Structure, catalysis and atomic reactions on the nano-scale: a systematic approach to metal hydrides for hydrogen storage," *Appl. Phys. A,* vol. 72, pp. 157-165, 2001.

[26] J. B. Bates, N. J. Dudney, B. Neudecker, A. Ueda and C. D. Evans, "Thin-film lithium and lithium-ion batteries," *Solid State Ionics,* vol. 135, pp. 33-45, 2000.

[27] J. P. Thomas and M. A. Qidwai, "Mechanical design and performance of composite multifunctional materials," *Acta Materialia,* vol. 52, pp. 2155-2164, 2004.

[28] J. B. Condon and T. Schober, "Proton conductors and metal hydrides," *Solid State Ionics*, vol. 77, pp. 299-304, 1995.

[29] T. Sakai, H. Ishikawa and K. Oguro, "Effect of microencapsulation of hydrogen storage allow on the performances of sealed nickel/metal hydride batteries," *J. Electrochem. Soc.*, pp. 558-562, 1987.

[30] Z. Zhu, S. Zhang, Y. Lv and X. Zhang, "Atomization of hydride with a low-temperature, atmospheric pressure dielectric barrier discharge and its application to Arsenic Speciation with atomic absorption spectrometry," *Anal. Chem.*, vol. 78, pp. 865-872, 2006.

[31] A. T. M. van Gogh, S. J. van der Molen, J. W. J. Kerssemakers, N. J. Koeman and R. Griessen, "Performance enhancement of metal-hydride switchable mirrors using Pd/AlO_x composite cap layers," *Applied Physics Letters*, vol. 77, pp. 815-817, 2000.

[32] M. Pourbaix, *Atlas of Electrochemical Equilibria in Aqueous Solutions*. NACE, Houston, TX, 1974.

[33] S. Murugesan and V. R. Subramanian, "Effects of acid accelerators on hydrogen generation from solid sodium borohydride using small scale devices," *J. Power Sources*, vol. 187, pp. 216, 2009.

CHAPTER 4:

DEVELOPMENT OF NANOPOROUS SILICON PROTON EXCHANGE MEMBRANE FOR MICRO FUEL CELLS

4.1. Introduction

The ever-increasing demand for high energy density power sources for portable applications has generated a worldwide effort towards the development of high-energy-density power sources. Although advances in lithium-ion battery technology in recent years have provided higher power device, this progress has not kept pace with the portable technologies, leaving a so-called power gap that is widely expected to grow in coming years. Micro fuel cell (MFC) technology, which has been under development for some time, has the potential to bridge this power gap. The energy density of the fuels used in MFCs exceeds that of the batteries by an order of magnitude. However, efforts to harvest this high energy density have been hampered by issues concerning the fabrication, performance, reliability, size and cost of MFCs. At the heart of these issues are the polymer membranes, which show low conductivity at low humidity and a large volumetric size change with humidity that is a major source of failure and integration difficulties. The development of improved membrane materials and configurations has been the focus of research for decades, and success in this regard would represent a key step forward in low-temperature fuel cell technology.

The content in this chapter is adapted from the published articles as follows;

- S. Moghaddam, E. Pengwang, Y-B. Jiang, A. R. Garcia, D. J. Burnett, C. J. Brinker, R. I. Masel, and M. A. Shannon, "An inorganic-organic proton exchange membrane for fuel cells with a controlled nanoscale pore structure," *Nature Nanotechnology*, vol. 5, pp. 230-236, 2010.

In addition, developing a membrane compatible with the manufacturing infrastructure within the semiconductor and micro-electromechanical systems (MEMS) silicon-processing industries would be a major technological breakthrough. To meet both of these objectives, we here introduce the concept of a surface nanoengineered, fixed-geometry, proton exchange membrane (PEM) that allows nearly constant proton conductivity over a wide range of humidity, with no changes in volume. In addition, our membrane is silicon-based, facilitating fabrication of membrane electrode assemblies (MEAs) and their further integration with microfabricated elements of MFCs.

Numerous studies have been conducted and significant progress has been made on microfabrication of different elements of MFCs. However, development of a silicon-based proton exchange membrane (PEM) has remained a major challenge. The potential advantages of a silicon-based PEM over the widely used Nafion membrane have encouraged development efforts in recent years [1, 2]. These efforts have been focused on creating a membrane resembling the Nafion structure (namely a poly-tetrafluoroethylene, PTFE, matrix with sulfonate acidic groups on the surface of its pores) within a porous silicon matrix. A porous silicon matrix provides better thermal and mechanical stabilities (especially at increased sulfonation level) for PEM than a polymer matrix, an aspect strongly desired for PEMs and widely sought through either incorporation of inorganic nanoparticles (e.g. SiO_2, TiO_2, and Al_2O_3) into polymer ionomers or development of inorganic PEMs (see a recent review by Devanathan [3]). Moreover, porous silicon proton exchange membranes (PS-PEM) do not swell and shrink upon water gain and loss thereby minimizing formation of cracks at the membrane and catalyst/electrode interface. It is less prone to pin hole formations due to local hot spots resulted from local dehydration and consequent ohmic losses seen in Nafion

membranes. In addition, as will be shown later, PS-PEM facilitates development of membrane electrode assembly (MEA) and its integration with other microfabricated elements of MFCs. Arrays of membranes fed from a single fuel supply manifold can be connected in series and parallel, using thin film metallic traces, to achieve high voltages thereby eliminating the need for multi-stack packages with layers of fuel and oxidant distribution channels or the power electronics to boost the output voltage of a single MEA.

Early efforts to fabricate PS-PEMs have focused on adding perfluorosulfonate ionomers such as Nafion® in a silicon membrane with microscale holes. Nafion tends to dehydrate at low relative humidity leading to low proton conductivity and poor performance. Aside from poor performance, the lack of adhesion between the perfluoro polymer and the silicon base structure, along with volumetric change of the material upon water gain and loss, results in failure of the MEA. In addition, the filling process of the holes can hardly be scaled up. The fundamental approach to solve this problem is to fabricate pores similar to that of Nafion and covalently bond molecules with functional groups on the pores' walls. However, these PS-PEM development have been unsuccessful due to difficulties in achieving two aims: 1) robust wafer-scale processing of nanoporous silicon membranes with uniform open pores; and 2) self-assembly of molecules in torturous nanopores with extremely high aspect ratios. The common approach used to fabricate porous silicon membranes through anodization process does not result in uniform open pores over the entire membrane and has high sensitivity to thickness variations across the standard silicon wafers. For functionalizing the pores, the common approach has been to soak the membrane in the solution containing the self-assembly molecules. Diffusion is relied upon to supply molecules to torturous nanopores

with aspect ratios in the 1000s, which inherently provides uneven coverage. Moreover, no evidence of functionalization deep within the pores has been presented.

In this study, we present development of a new generation PS-PEM. This has been achieved through development of a set of key processes for fabricating nanopores uniformly within a silicon membrane and self-assembly of a dense, contiguous layer of functional molecules on the nanopores' wall. However, test results on a membrane developed using the new processes revealed a fundamental issue with a fixed-geometry uniform pore (i.e. homogeneous) membrane. So, we developed the concept of non-homogeneous fixed-geometry membrane with nearly humidity-independent proton conductivity. In a conventional membrane, the water meniscus becomes unstable within the pores in a homogeneous fixed-geometry membrane at low humidity because Nafion pores shrink with decreasing humidity, leading to partial drying out. This drying out results in a significant can also increase in reactant crossover. To better understand the strategy behind our approach for overcoming the deficiencies of Nafion and significantly exceeding its proton exchange capacity, a brief overview of the existing hypothesis about the morphology of Nafion and its associated proton transport mechanisms is provided in summarized in the following section.

4.2. Proton Transport Mechanisms

The morphology of Nafion and mechanism of proton conduction within its pores have been the subject of numerous studies. The Nafion structure consists of a PTFE backbone with perfluoro vinyl ether pendant terminated by sulfonic acid groups, a combination that results in formation of hydrated nanoscale domains within which ionic transport occurs. The

morphology of Nafion structure has been extensively debated and various experimental and modeling tools have been implemented to reveal the nanoscale architecture of hydrophilic domains within the PTFE hydrophobic matrix. It is widely known that Nafion morphology changes with hydration level. Evidence of the effect of thermal history [4] as well as processing conditions [5] on its morphology has been presented. Several models [6, 7] have been proposed over the past few decades to describe the nature of the interpenetrating hydrophobic and hydrophilic domains. These models have been constructed through fitting the small angle X-ray and neutron scattering (SAXS and SANS) data. One of the early models of hydrated Nafion, the cluster-network model [8], suggested periodic 3-5 nm diameter spherical ionic clusters interconnected by narrow water channels of 1 nm width. More recent models [9-13] have suggested a network of elongated water channels (cylindrical, rectangular parallelepiped, or ribbon-like) with different characteristic length scales (as shown in Figure 4.1a and b). Recently, Schmidt-Rohr and Chen [7] proposed a new model that matches the prior experimental SAXS data better than the previous models. Their model suggests elongated cylindrical water channels with diameter of 1.8-3.5 nm with persistence length of more than 20 nm within the hydrophobic PTFE matrix.

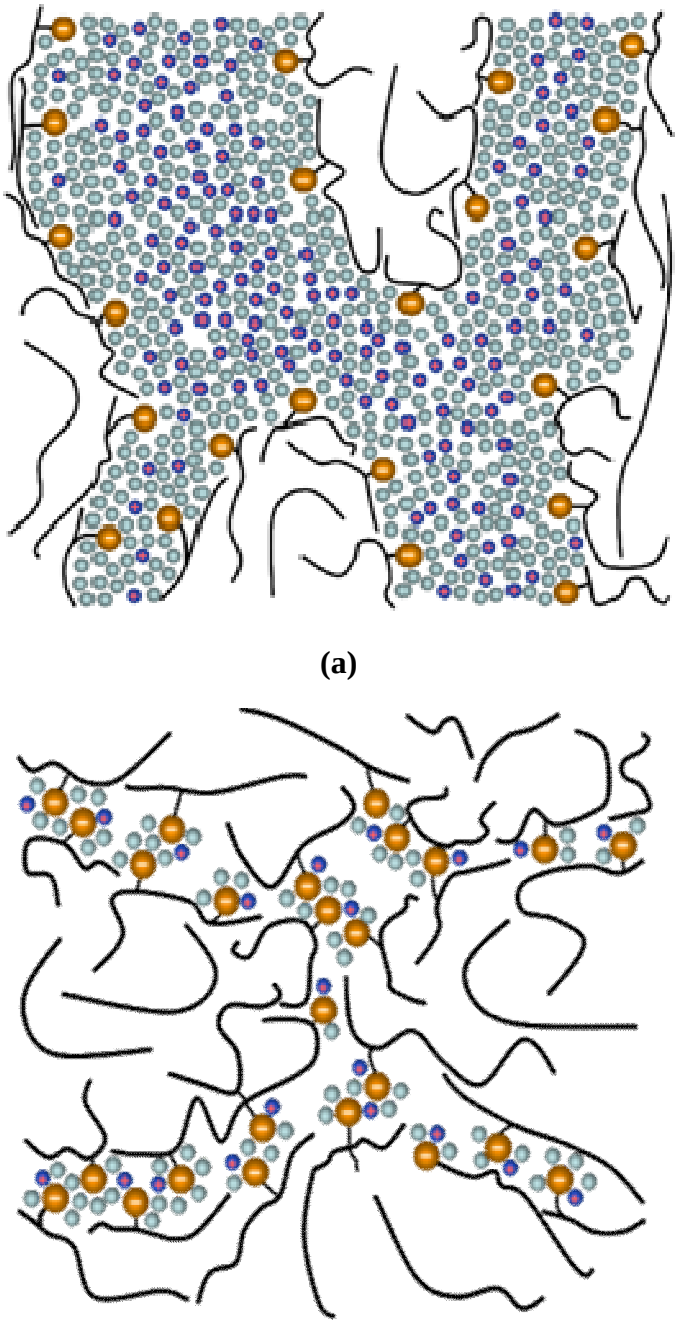

Figure 4.1. Schematic of the hydrated Nafion structure showing water molecules (cyan) and hydrated protons (blue) within water channels with sulfonate wall groups (light brown) terminating the perfluoro vinyl ether pendants on a hydrophobic PTFE backbone for **(a)** ideal membranes; **(b)** dehydrated membranes.

In terms of proton transfer, two transport mechanisms associated with different regions of the water channels have been proposed. At the center of the channels, well separated from the sulfonate groups, water is suggested to be bulk-like [14, 15]. The region containing excess proton in bulk-like water has been described as hydrated hydronium (i.e., $H_9O_4^+$, the Eigen ion) or a smaller dimer sharing the excess proton (i.e. $H_5O_2^+$, the Zundel ion). A continuous dynamical exchange between these configurations exists [16, 17] exhibiting a von Grotthuss-type sequential hopping mechanism or "structural" diffusion. The H_3O^+ ion also undergoes ordinary mass diffusion, the so-called vehicular mechanism. The relative contribution of the vehicular and structural diffusion mechanisms has been widely debated [3, 14, 15, 18-22]. Nonequilibrium statistical mechanics analysis of Paddison and Paul shows that water and hydrated proton diffusion are retarded at the vicinity of the pore wall due to the presence of sulfonate groups. The proton mobility at low ($\lambda<\sim6$) and intermediate ($\lambda<\sim10$) hydration levels has been suggested to be vehicular in nature [15, 19]. In a well hydrated 3.2 nm channel, Paddison and Paul [19] showed that transport within 12 A of the pore wall is predominantly vehicular and both mechanisms are active within 4 A of the channel center axis. Using their data for distribution of proton diffusion coefficient within the channel, we determined that approximately 90% of proton transport takes place at the central region of the channel. In addition to the view of overlapping mechanisms and suggestion of them having similar magnitude, views on dominance of one mechanism versus another also exist. While interpretation of Perrin et al. [22] of their quasielastic neutron scattering (QENS) data on the confinement effects on water mobility in molecular level rules out the Grotthuss mechanism and supports vehicular mechanism at all hydration levels, Choi et al. [21]

transport model suggests dominance of Grotthuss diffusion mechanism in all hydration levels.

4.3. Approach

Our strategy for the silicon-based membrane is to fabricate ~5–7-nm-diameter silicon pores and then assemble 3-mercaptopropyltrimethoxysilane (MPTMS), $SH–(CH_2)_3–Si–(OCH_3)_3$, molecules on the modified surface of the pores. The –SH end group of MPTMS is later oxidized to $–SO_3H$. The thickness of the MPTMS self-assembled monolayer (SAM) on silicon oxide is 0.8±0.1 nm. An increase in the size of the head group after oxidation increases the thickness of the SAM to ~1 nm. The overall size of the pores after self-assembly therefore reduces to 3–5 nm. To enable high conductivity to be maintained at low humidities, an ultrathin conformal layer of silicon dioxide is deposited at the mouth of each of the larger silicon nanopores (as shown in Figure 4.2), creating small apertures. Using the Kelvin equation, $\ln RH = -2\gamma V_m / rRT$, we calculated that a 1-nm-diameter water meniscus can be stable at 10% humidity, which is lower than the humidity level found in most practical applications of fuel cells. Although the specific conductivity of the silica layer can be relatively low, its overall contribution to total membrane resistance is negligible. In contrast to the uniform incorporation of nanoparticles (for example, SiO_2) into Nafion to enhance its hydration properties (see a recent review by Devanathan [3]), or homogeneous inorganic–organic membranes such as the one recently developed by Athens and colleagues [23], this asymmetric membrane construction maintains hydration without a detrimental effect on proton conductivity.

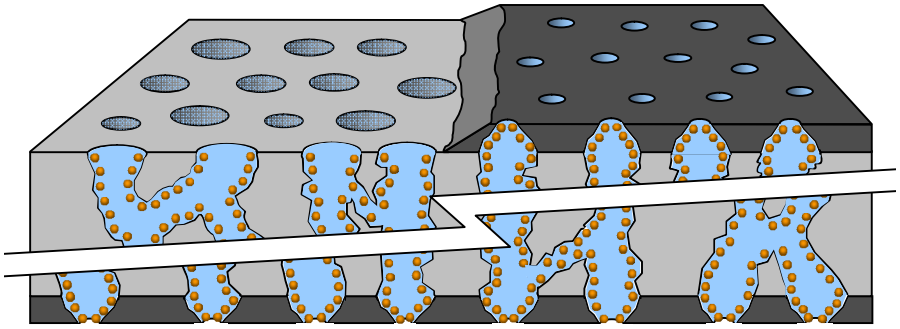

(a)

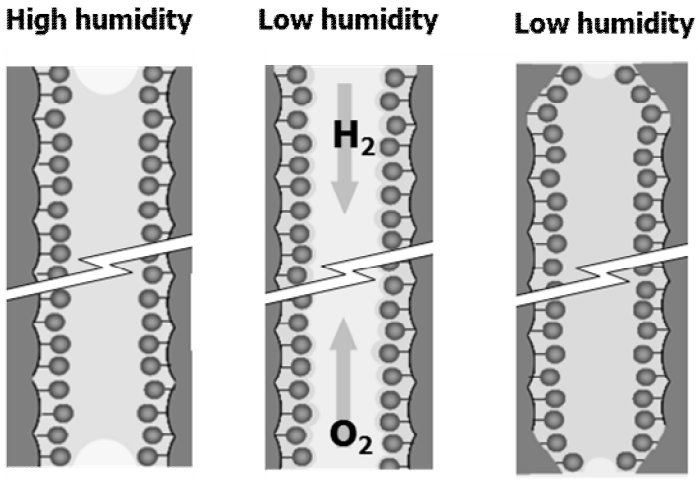

(b)

Figure 4.2. (a) Schematic of the membrane with functionalized pore wall and thin layers of porous silica on both side of the membrane. The lateral scaling is stretched for clarity. Porous silicon membrane (light grey); silica layer (dark grey); self-assembled molecular monolayer (orange); water (cyan). **(b)** Zoomed-in images for original nanoporous silicon membrane, compared with the modified membrane at different levels of humidity.

4.4. Microfabrication Processes

Fabrication of the silicon membranes begins with KOH etching of a p-doped <100> silicon wafer. A 0.8-µm-thick low-pressure chemical vapour deposition (LPCVD) nitride layer was used as a protection mask in KOH solution. The nitride layer on the back side of the membrane was patterned with a photoresist layer and then etched using a Freon plasma. The exposed silicon areas were then etched in KOH until a membrane thickness of 24±2 µm was reached. The nitride layer on the front side of the membrane was subsequently patterned and etched to expose the silicon. In membranes with an additional metal layer on the front side, the patterning step was followed by wet etching of the metal layer and then Freon plasma etching of the nitride layer.

Anodization is then used to create the pores within the silicon membrane. A typical two-cell anodization process [24], in which the wafer is installed between two electrolyte baths (manufactured by AMMT GmbH), leaves a layer of non-porous silicon on the back side of the membrane. More reviews of the challenges involved in the fabrication of open through-holes can be found in the work of Foll and colleagues [25]. The cross-section view of the nanoporous silicon after anodization process is shown in Figure 4.3a. In this process, after some pores open on the backside of the membrane, current flows through the pores instead of anodizing the rest of the membrane as shown in Figure 4.3b. To open up the pores, the remaining silicon layer should be etched using Freon plasma. As a result of variations in the thickness of the remaining silicon layer on a single membrane and over different membranes on a wafer, as well as the pore penetration depth (Figure 4.3a-b), the silicon layer is etched in some areas, thus exposing the porous silicon. The exposed porous silicon is then

etched at a much faster rate (3–5 times) than the silicon, resulting in localized thinning of the membrane. This issue makes the fabrication of thin membranes impractical.

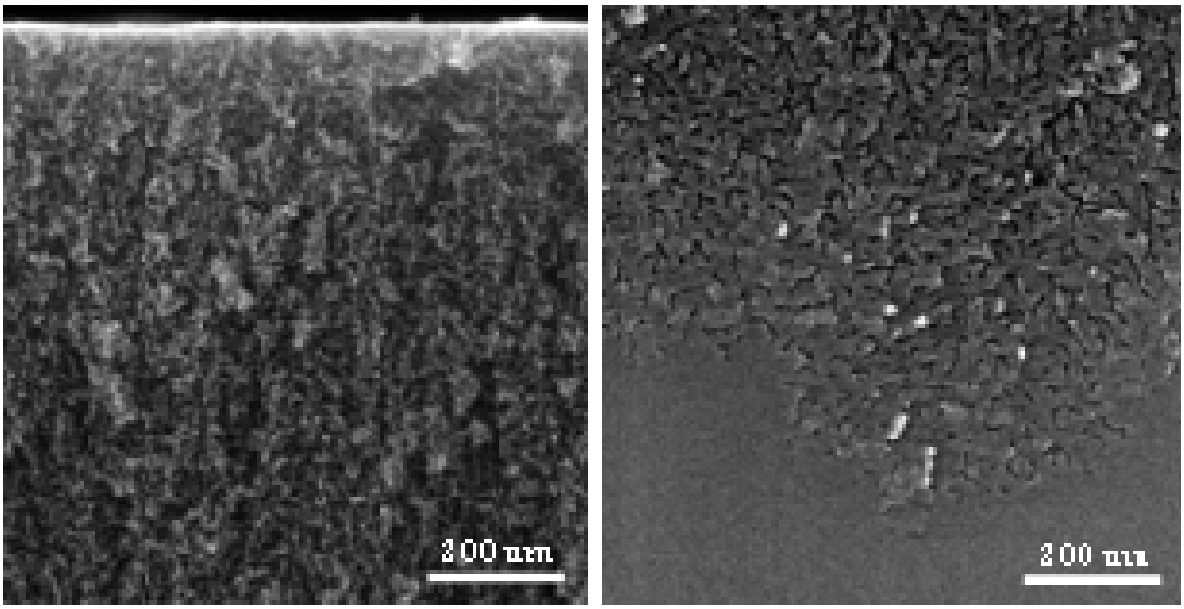

(a) **(b)**

Figure 4.3. Fabricated membranes of porous silicon proton exchange membranes. **(a)** cross section view of the membrane fabricated in a two-cell anodization bath at frontside; and **(b)** at approximately 1-2 microns from backside of the membrane.

To overcome these issues, we developed a self-terminating method that leads to the production of membranes with uniform, open-ended pores, in a single step. The process involves the deposition of a layer of chromium and gold on the back side of the membrane using a magnetron sputtering system (pressure, 5×10^{-2} torr; power, 300 W d.c.) in argon gas. The back-side chromium/gold layer is wired directly to the anode electrode to provide an electrical path by which the electrons can exit the silicon membrane once the pores penetrate to the back side of the membrane. When the pores open up, at any location, the chromium

layer is etched and the gold layer delaminates, resulting in local electrical discontinuity and therefore termination of anodization. Because the gold layer is not etched, it maintains the electrical connectivity of the rest of the membrane to the circuit. The gold delamination process occurs gradually over the entire wafer until the pores on all membranes are opened. This event appears as a sudden rise in process voltage, as shown in Figure 4.4. The finite increase in voltage arises from the continuation of the anodization process beyond the edges of the membrane into the bulk silicon. However, the gold film does not always break of entirely from all four edges of the membrane. A gentle water spray after the wafer is removed from the anodization batch removes the Au layer as shown in Figure 4.5. Interestingly, the gold layer left outside the membrane can be used as the anode electrode. The cathode electrode is also a chromium/gold layer deposited on the front side of the wafer before etching the nitride layer (both chromium/gold and nitride layers are etched in one patterning step after which the silicon membrane is exposed). Also, the front side nitride layer electrically isolates the cathode and anode electrodes. The cross-section view of the membrane at the front side and backside after the self-terminating process is shown in Figure 4.6 and 4.7 respectively.

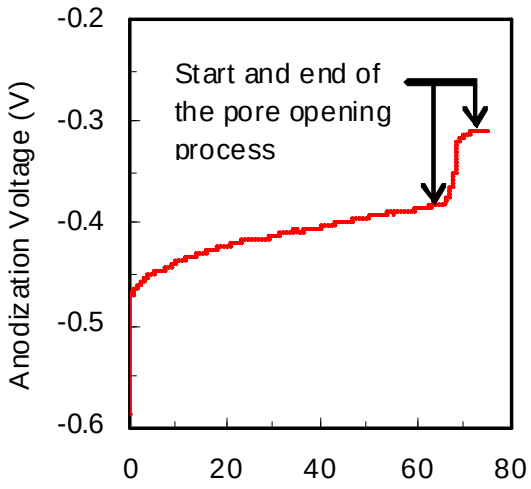

Figure 4.4. Variation of the anodization voltage at constant current showing a sudden rise in voltage when the electrolyte reaches the chromium layer.

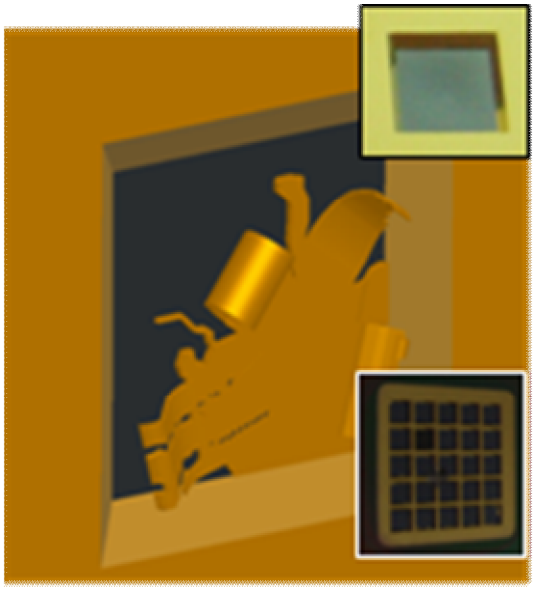

Figure 4.5. Schematic of the gold layer peel-off process when the chromium layer is etched. Insets: actual images of two silicon dies, one with a single membrane and another with a 5×5 matrix of ~2(2 mm2 membranes after completion of the process. The remaining gold layer outside the membrane area is later used as a current collector in a complete MEA.

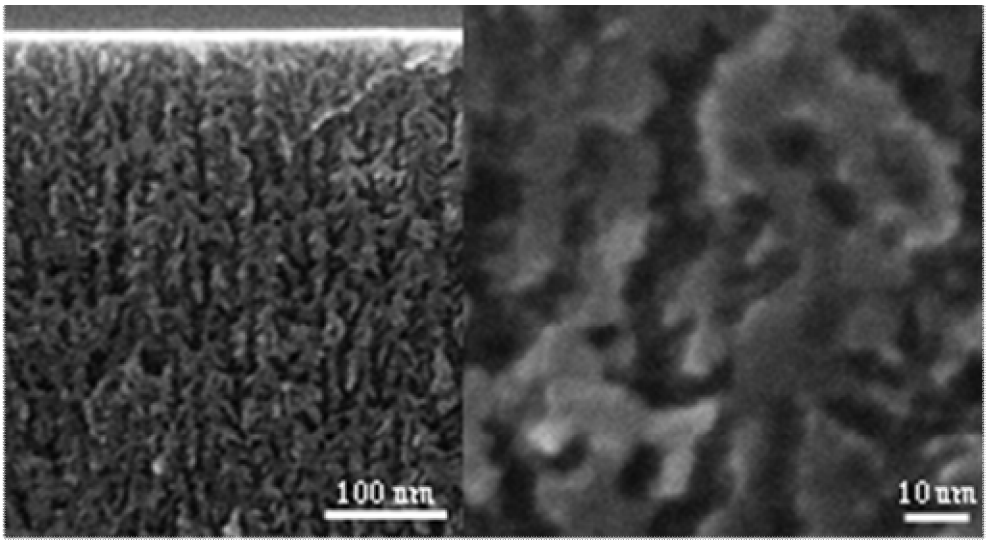

Figure 4.6. Cross-section of the membrane fabricated using the self-terminating process developed in this study at the front side of the membrane.

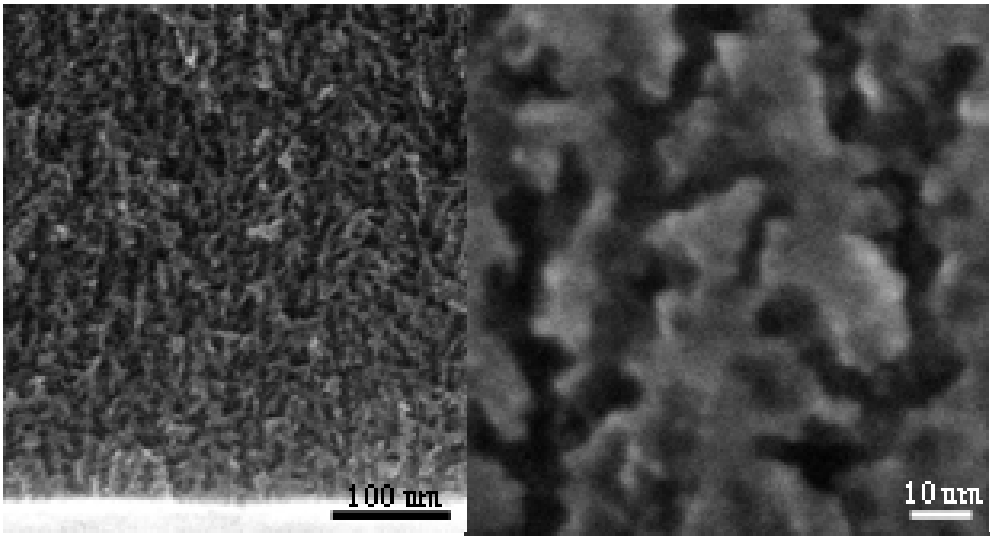

Figure 4.7. Cross-section of the membrane fabricated using the self-terminating process developed in this study at the back sides of the membrane.

4.5. Fourier Transform Infrared (FTIR) Spectroscopy

In order to avoid the previous issues, the membrane after anodization process is left in de-ionized (DI) water for a few hours to clean the anodization electrolyte from the pores and hydroxylate the pore surface. As the Fourier transfer infrared (FTIR) spectra of the membrane of Figure 4.8a suggests, the pore wall is covered with SiH_x (x=1-3) hydrophobic surface species (the absorption bands were assigned by Glass et al. [26]). Based on the drop in intensity of the 876 cm^{-1} absorption peak during the DI soak process, we assign this unsettled peak to the bending mode of $–O_3SiH$, because the decrease in intensity of this mode is accompanied with that of the known peak 2260 cm^{-1} and increase in 3743 cm^{-1} intensity. Assignment of this peak to other modes such as Si-O stretching and the OH bending of the SiOH group coupling of Si-H and Si-O-Si motions seems inaccurate, since intensity of the Si-O, Si-O-Si, and SiOH bonds do not decline during the two-day DI soak process. We have determined that the 1142 cm^{-1} peak developed during the two-day DI soak process is due to surface oxide.

To successfully conduct silane-based self-assembly within the membrane, the surface of the pores needs to be converted to hydrated silica [27-31]. This was achieved in two steps. First, the membrane was partially oxidized at low temperature (300°C) in an O_2 furnace. Although temperatures close to 600°C are required to desorb surface hydride species [32, 33], processing at such a temperature level is not practical due to the resultant significant changes in membrane morphology and membrane fracturing. The morphology of porous silicon is known to change at temperatures above 350-450°C [33, 34] due to changes in the crystalline dimensions (that is. coarsening of the porous silicon texture [35, 36]). The

changes result in significant decrease in the specific surface area [33]. However, no distinct texture coarsening has been observed at 300°C [35, 36].

The oxidized membrane spectra (Figure 4.8b) shows that all Si-H_x vibrational stretch modes have shifted to 2260 cm^{-1}, with a low intensity tail extending towards lower frequencies suggesting that the backbond of the silicon atoms are targeted by oxygen and maximum degree of oxidation to $–O_3SiH$ (corresponding to absorption at 2260 cm^{-1} frequency [37-39]) has occurred. The lower frequency tail also indicates the presence of a relatively small population of -O_ySiH_x surface species. After the oxidation step, leaving the membrane in DI water results to insertion of oxygen into Si-H bonds and the creation of SiOH surface species. As a result, the absorption bands at 2260 and 876 cm^{-1} associated with $–O_3SiH$ stretching and bending modes, respectively, disappear, and absorption at 3743 cm^{-1}, assigned to isolated SiOH species [40], intensifies together with the Si-O asymmetric stretching vibrations at 1200 to 1000 cm^{-1} assigned to the siloxane network (Figure 4.8c). The broad absorption band centered at ~3500 cm^{-1} corresponds to the overlapping of the O-H stretching bands of hydrogen-bonded water (H-O-H···H) and SiO-H stretching of surface silanols hydrogen-bonded to molecular water (SiO-H···H2O) [41]. These results suggest the creation of the well-hydrated silica pore surface needed for the subsequent self-assembly step.

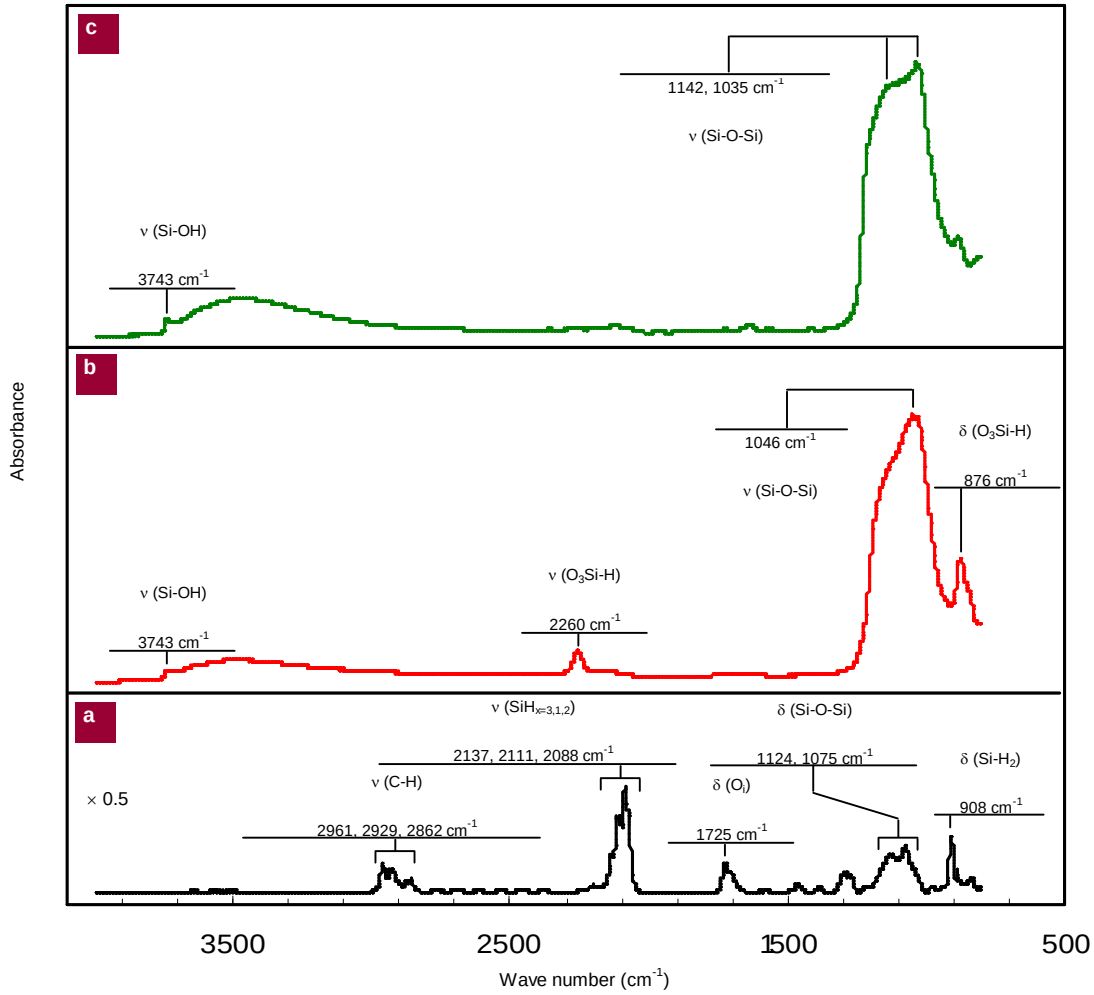

Figure 4.8. FTIR spectra of the membrane at different stages of pore surface modification. **(a)** anodized membrane left in DI water for a few hours. **(b)** oxidized membrane at 300 ºC in atmospheric O_2. **(c)** oxidized membrane after room temperature DI water soak for 2 days (no further changes in spectra after 4 days was observed).

4.6. Self-assembly of Functional Group

The membrane die was installed within a fixture between the top and bottom compartments of the functionalization set-up. This arrangement allowed continuous extraction of the depleted solvent from the bottom of the membrane pores while the solute-rich solvent was supplied over the membrane. A typical process run involved evacuating the chamber and purging with helium multiple times to remove condensed water from the pores. Excess water results in self-polymerization of the MPTMS molecules and clogging of the pores (note that surface adsorbed water remains on the surface). MPTMS in benzene solution was then supplied to the solution reservoir on top of the membrane. Although the top chamber was charged with helium and the vacuum and helium lines connected to it were closed, the lines connected to the bottom compartment were opened slightly to maintain a slow flow of dry helium. The process was continued until the top reservoir was emptied of solution.

Owing to the large surface area and high aspect ratio of the pores, a reactor was constructed (Figure 4.9) to continuously supply an ~1 mM solution of MPTMS to one end of the pores and extract the solvent from their opposite end. A self-assembly solution to the pores is functionalized to the membrane. This approach essential for uniform coverage of the super high aspect ratio pores of the membrane. This procedure enabled uniform functionalization of the hydroxyl groups within the membrane (estimated to be ~5 sites nm^{-2}). A simple estimation suggests that one pore volume of a 1 mM solution contains four orders of magnitude fewer molecules than necessary for complete coverage of all active sites on the wall of a 25 μm long pore. Therefore, high aspect ratio pores should be filled with solution thousands of times to supply enough solute molecules to the pores. Increasing the

solution concentration to reduce the number of filling times is not an option, since it leads to self-polymerization of the solute molecules and verified in our preliminary tests. The setup allows holding the membrane die between top and bottom compartments of a chamber and extracting the depleted solvent from the bottom of the membrane pores continuously while the solute-rich solvent is supplied over the membrane. A typical process run involves installing the membrane die within the setup and vacuuming the chamber and purging with helium multiple times to remove condensed water from the pores. Excess water results in self-polymerization of the MPTMS molecules and pore's clogging (note that surface adsorbed water that facilitate hydrolysis during silane-based self-assembly process remains on the surface). Then, MPTMS in benzene solution is supplied to the solution reservoir on top of the membrane. While the top chamber was charged with helium and the vacuum and helium lines connected to it were closed, the lines connected to the bottom compartment were slightly open to maintain a slow flow of dry helium. The process was continued until the top reservoir was emptied from solution.

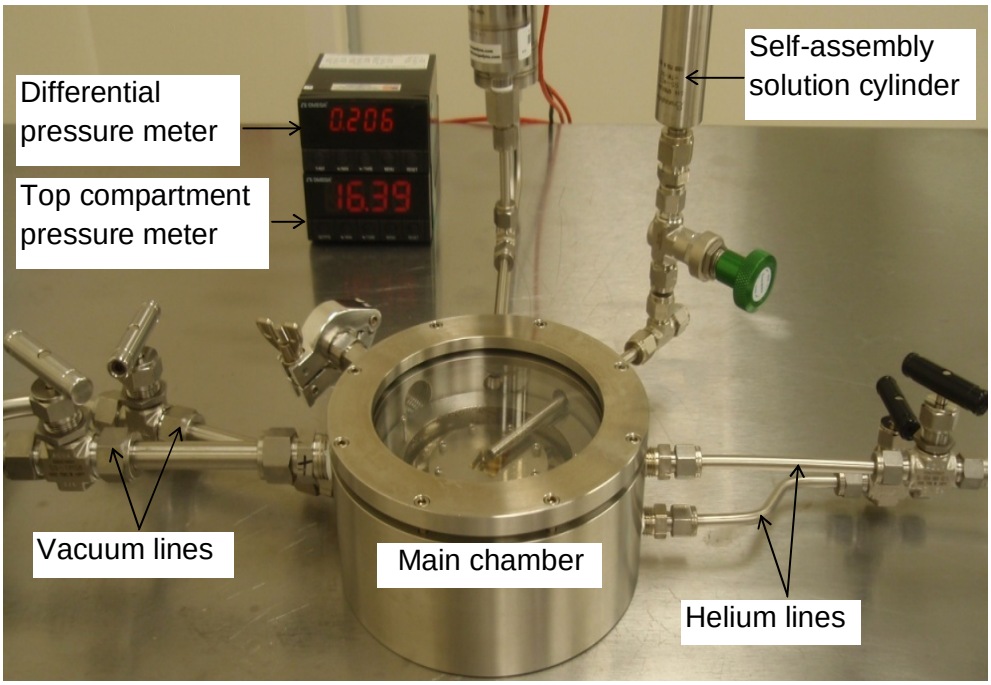

Figure 4.9. Membrane functionalization setup for self-assembly of functional groups on the membrane wall of the pores. A main chamber consists of top and bottom compartments between which the membranes wafer is installed.

Full penetration of the functional group inside the membrane was verified using Time of Flight-Secondary Ion Mass Spectroscopy (ToF-SIMS) with depth profiling, as can be seen in Figure 4.10 and 4.11. The phased depth profile using a 22 kV Au+ analysis beam and a 2 kV Cs+ sputtering beam is implemented in this experiment. The –SH end group of the MPTMS molecule was then oxidized to $-SO_3H$ in dilute nitric acid and, finally, the membrane was maintained in a large volume of DI water for 24 h to diffuse out the nitric acid and hydrate the pores.

In addition to the thickness issue, our analysis of the membrane composition using Time-of-Flight Secondary Ion Mass Spectroscopy (ToF-SIMS) shows significant rise in fluorine presence particularly towards the backside of the membrane. Cleaning the pores surface is essential for the self-assembly process. Although cleaning can be done using standard SC-1 cleaning process (1:2:10 NH_4OH:H_2O_2:H_2O solution at 75°C), in which continuous oxidation of the silicon backbone attacked by -OH and its subsequent dissolution in aqueous ammonia (NH_3) under-etches the fluorine surface compounds, the process quickly enlarges the pores non-uniformly across the membrane thickness. The membrane can completely dissolve in solution for several minutes depending on its thickness and porosity. In addition to the thickness issue, our analysis of the composition of the membrane using time-of-flight secondary ion mass spectroscopy (ToF–SIMS) showed a significant rise in the presence of fluorine, particularly towards the back side of the membrane as shown in Figure 4.10. However, the self-terminating process does not have this issue as shown in Figure 4.11.

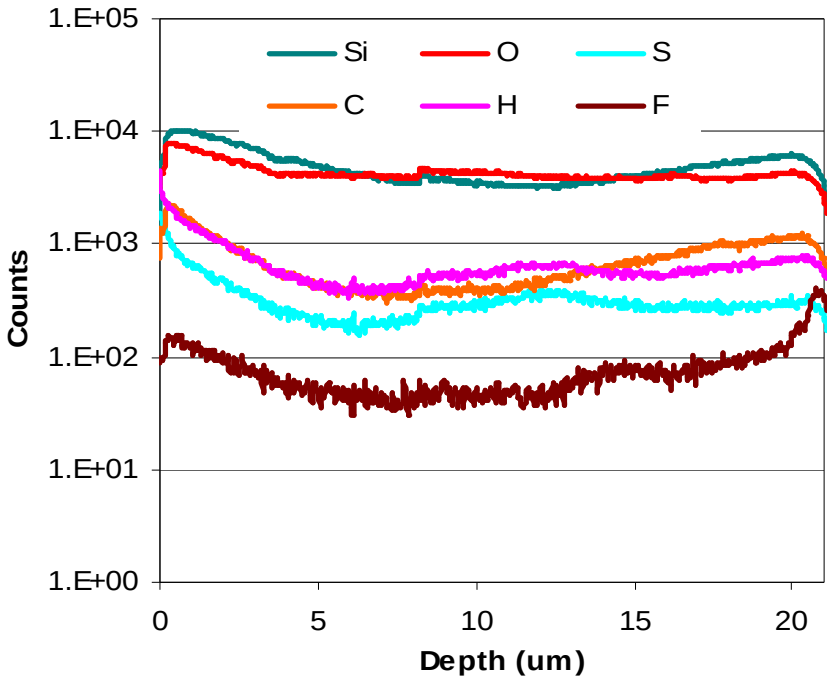

Figure 4.10. ToF-SIMS results showing composition of the 20-µm thick membrane from previous processes. A spot on the membrane was carved in gradually until reached to the bottom of the membrane. Note that the sudden spike in fluorine content at the bottom of the membrane is due the back-etching process used to open up the pores.

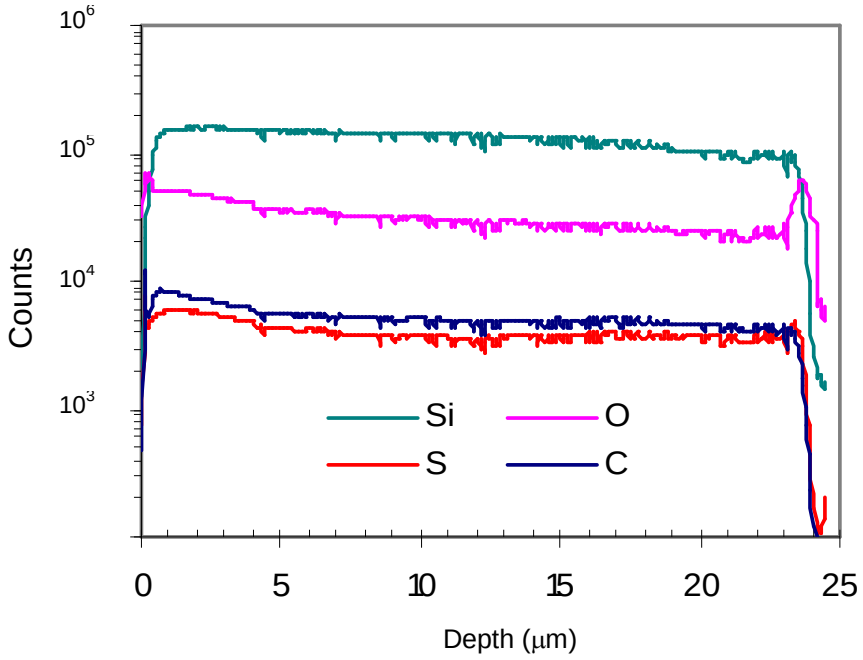

Figure 4.11. Time of Flight-Secondary Ion Mass Spectroscopy (ToF-SIMS) results showing composition of a functionalized 24 microns thick membrane with a self-terminating process.

4.7. Modifications with a Plasma-Defined Atomic Layer Deposition

To create a thin hydrophilic silica aperture at the mouth of the pores, we used plasma-directed atomic layer deposition (PD–ALD) [42]. Unlike conventional ALD, in PD–ALD, a remote plasma (instead of water vapor exposure) is used to activate the surface. Because both the plasma Debye length and the radical mean free path greatly exceed the pore diameter, surface activation and silica deposition are confined to the immediate external surface of the membrane pores, with no deposition on the internal pores. Successive oxygen plasma and tetramethyl orthosilicate (TMOS) exposure steps using an argon carrier gas resulted in an ~2-

nm-thick silica layer. The interior of the pores within the silica layer were then functionalized with MPTMS. Scanning electron microscopy (SEM) images for the membrane surface before and after PD-ALD are shown in Figure 4.12. The maximum diameter of the pores at the two surfaces of the membrane is ~2 nm, as estimated from the SEM and analysis of water desorption isotherms (Figure 4.13). The graph of water desorption isotherms shows the corresponding Kelvin diameter as well as the corrected Kelvin diameter based on the t-curve for a silica surface of Hagymassy and colleagues. Note that using silica t-curve results in a small error in the case of the functionalized pores.

We used our previously developed a plasma-defined atomic layer deposition (PD-ALD) technique [42] to construct an approximately 2 nm thick silica layer to reduce the minimum pore size at the finished surfaces of the membrane to 2 nm. Unlike in regular ALD, in which deposits penetrate into the internal porosity, PD-ALD process is confined to the immediate surface. This is achieved through selection of precursors that are nonreactive unless triggered by plasma, so that ALD can be spatially defined by the supply of plasma irradiation. Because both the plasma Debye length and the radical mean free path exceed greatly the pore diameter, deposition does not occur within the interior pores. We used tetraethyl orthosilicate (TEOS) precursor. The interior of the pores within the 2 nm thick silica layer was then functionalized with MPTMS. The maximum diameter of the pores at the two surfaces of the membrane is expected to be approximately 2 nm (factoring in the SAMs thickness).

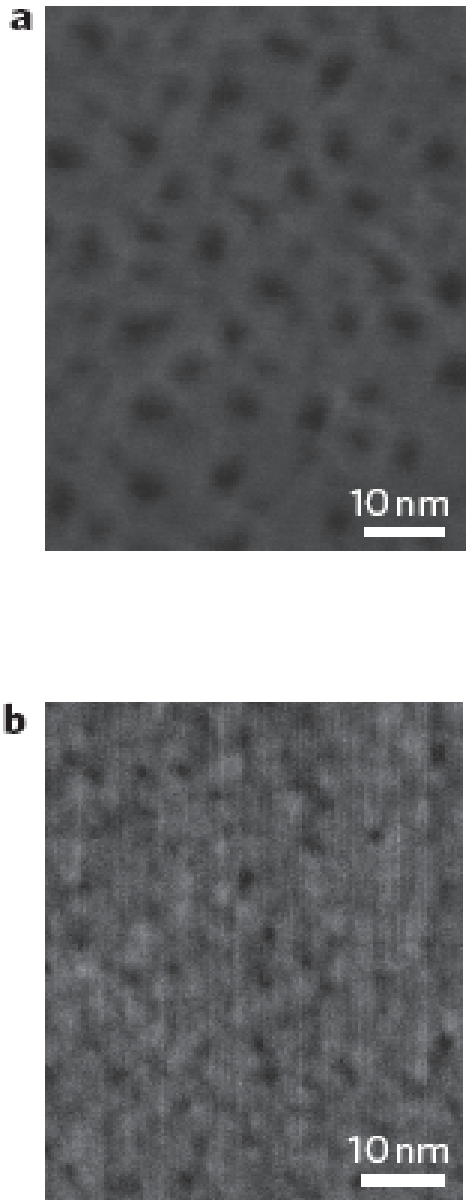

Figure 4.12. Top view of two membranes without **(a)** and with **(b)** the PD–ALD silica layer.

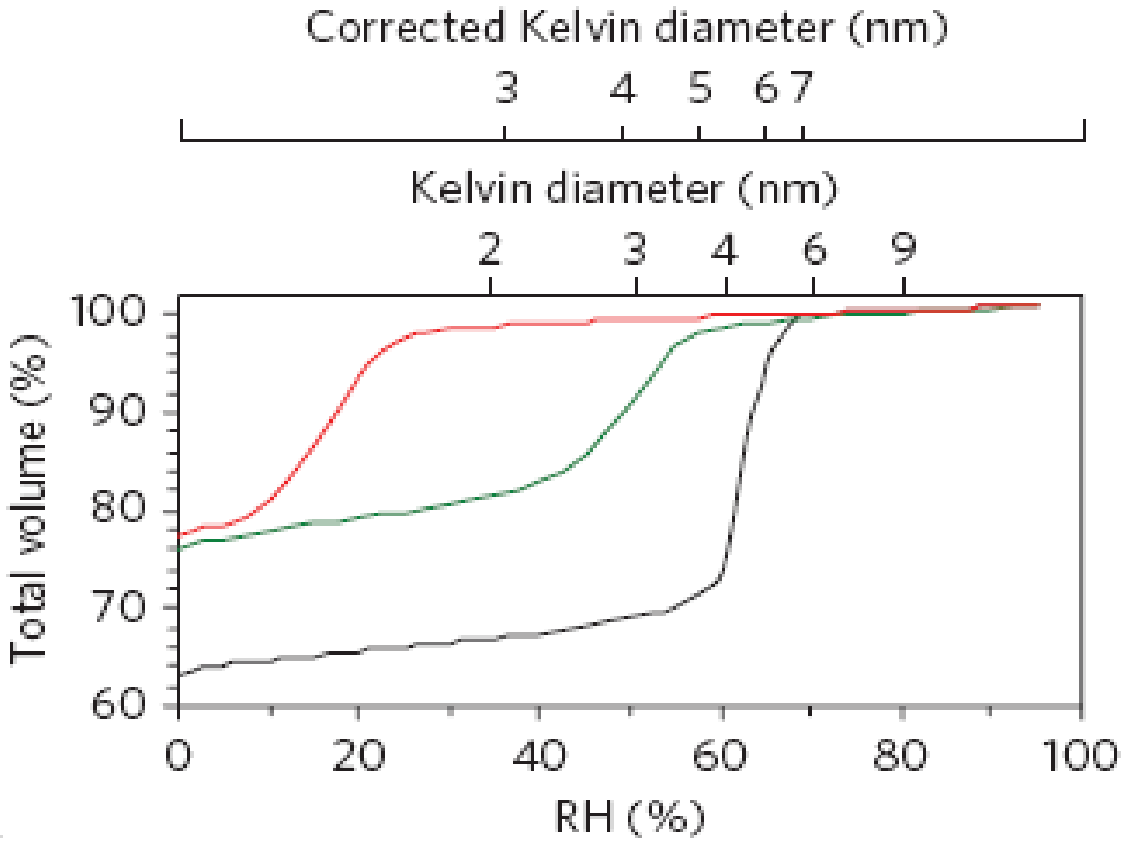

Figure 4.13. Water desorption isotherms of the membrane (determined using DVS-Advantage 1 machine (Surface Measurement Systems) on samples with 25 membranes at 25°C) before functionalization (black), after functionalization (green) and after application of the PD–ALD silica layer and subsequent functionalization (red).

The last fabrication stage of the MEA is spray painting of the anode and cathode catalysts on the membrane (Figure 4.14). A catalyst ink with an 18 wt% ratio of Nafion ionomer 1100 EW (from Solution Technology) to platinum back (from Alfa Aesar) was prepared in de-ionized (DI) water and isopropyl alcohol (IPA). Direct spray painting of the catalyst ink onto the membrane is straightforward, because the membrane does not swell and wrinkle as the catalyst solution comes into contact with the membrane surface. The membrane was set on a hot plate at 85°C during spraying. Because a relatively high thermal conductivity of the membrane, the solution droplets evaporate fast when it contacts the membrane surface. As mentioned previously, and shown in Figure 4.5, chromium/gold layers already deposited on both sides of the die are used as current collectors. The catalyst layer overlaps with the chromium/gold electrode around the edges of the membrane and provides electrical connectivity. The platinum loading in both anode and cathode catalysts layers was approximately 7 mg/cm^2.

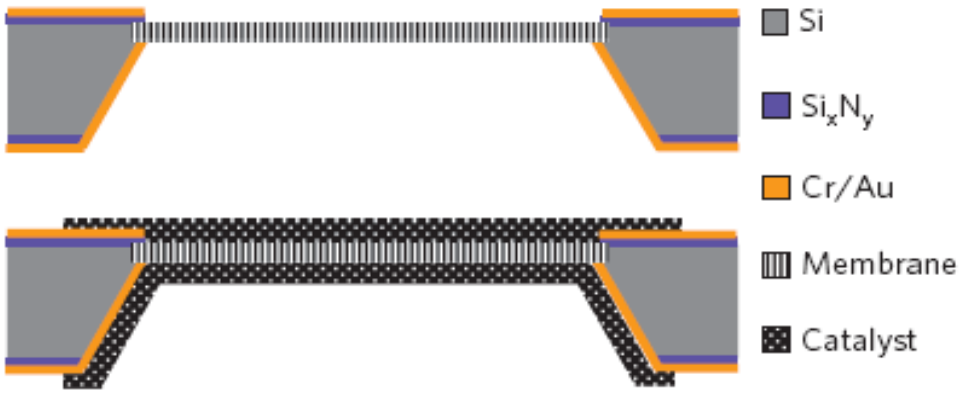

Figure 4.14. Cross-sectional schematic of a single membrane within its silicon die before and after application of the catalyst layers.

4.8. Results and Discussions

All tests were conducted on the membrane electrode assemblies (MEAs) in a configuration most relevant to micro fuel cells (MFCs), in which no auxiliary equipment for conditioning the membrane as well as the supply gases is desired. The condition of the testing is at room temperature (~25°C). Hydrogen is supplied to the anode through a hole within the bottom Teflon block, and an opening in the top Teflon block exposes the cathode to air. The internal electrical resistance of the package was measured to be 7 mΩ. This was measured by replacing the device die with a gold foil and using the four-probe measurement technique. The test package (Figure 4.15) was left in an environmental chamber to simulate different ambient humidity levels (the uncertainty in the humidity measurement was ±2%). Then, the data is collected for the performances.

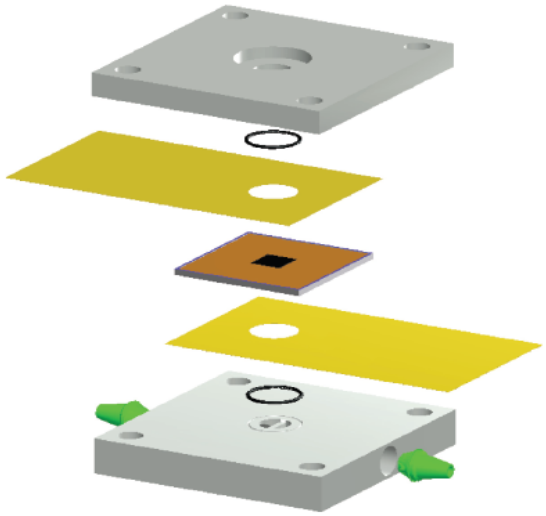

Figure 4.15. Three-dimensional schematic of the MEA test package showing two Teflon blocks sandwiching the MEA, with two 50-μm-thick gold foils positioned in between, coming into contact with the anode and cathode electrodes to provide an electrical connection to the outside of the package.

The membrane proton conductivity was measured using the four-probe technique (using a Solartron SI 1287). The results (MEA-1) are compared (Figure 4.16) with another silicon-based MEA but without the PD–ALD-deposited silica layers (MEA-2), as well as with another MEA based on DuPont Nafion PFSA NRE-211 membrane (MEA-3) with a nominal thickness of 25 microns. This MEA was fabricated by sandwiching Nafion between two stainless steel foils with 2 x 2 mm^2 square openings aligned during adhesive bonding of the layers. The exposed 2 x 2 mm^2 Nafion membrane was subsequently brush-painted with catalyst. Before discussing the various differences between the developed membrane and Nafion, we should mention that adding the silica layer resulted in ~25% decline in the

maximum conductivity of the PS–PEM, from ~0.11 to 0.08 S cm^{-1}. This significant decline is most likely due to the closure of some of the smaller membrane pores after the PD–ALD and subsequent self-assembly processes, rather than impeded proton mobility at the smaller entrance and exit of the pores, considering the small thickness of the silica layers.

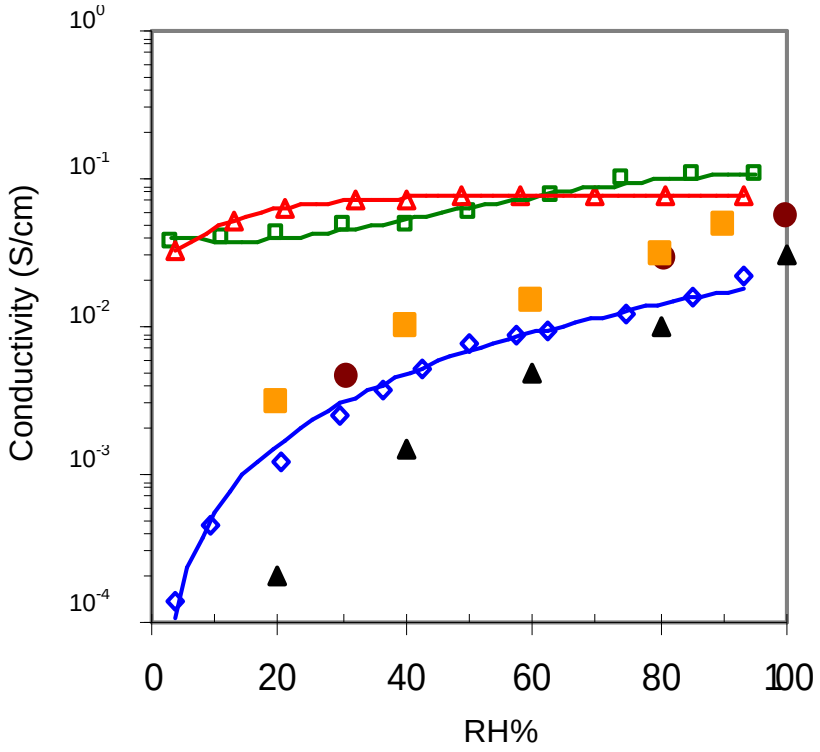

Figure 4.16. Proton conductivity as a function of humidity: PS-PEM with the PD-ALD-deposited silica layers, MEA-1 (red), PS-PEM without the silica layers, MEA-2 (green), Nafion NRE-211 hot-pressed at 100ºC, MEA-3 (blue), N-117 heat-treated at 105ºC (black triangles) and 30ºC testing temperature [4], N-117 at 30ºC [18] (orange squares), N-117 at 30ºC [43] (brown circles).

Other than this observation, the results show that the conductivity of the MEA-1 membrane is almost constant down to ~20% humidity, at which point it starts to decline significantly. A similar trend is seen for the MEA-2 membrane, but with the decline beginning at a higher humidity level (50–60%). This difference is expected, because a smaller pore diameter allows the water meniscus to remain stable at a lower humidity ambient. The decline in humidity levels beyond this thermodynamic equilibrium condition leads to partial drying out of the pores and an increase in crossover, as is made evident by the drop in open circuit potential (OCP) (Figure 4.17). Overall, the data suggest a nearly humidity-independent conductivity, as long as the vapor pressure at the membrane/ambient interface remains below the ambient saturated vapor pressure, so that the ambient vapor condenses within the pores, keeping them filled with water. This fundamentally different property of the silicon-based membrane compared to that of Nafion, in which the pores shrink at low ambient humidity, is a major contributing factor to the difference in conductivity between these two membranes. When Nafion shrinks with decreasing humidity, the amount of bulk-like water at the centre of the pores sharply declines. Shrinkage, along with a reduction in the interconnectivity of the water clusters, is responsible for the exponential decay in Nafion conductivity. The inhomogeneous construct of the porous silicon/ALD silica membrane creates an aligned barrier of silica pores over the larger silicon nanopores. Although the homogeneous incorporation of silica nanoparticles into Nafion has been shown to enhance water retention at low humidity, it results in decrease in proton conductivity compared to a fully hydrated Nafion, perhaps due to narrow water channels with low proton mobility.

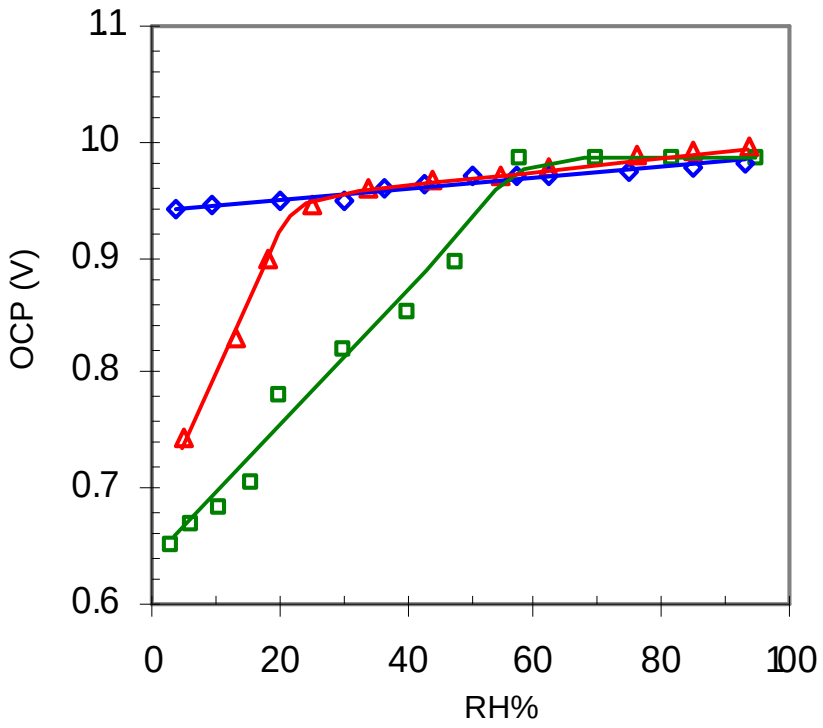

Figure 4.17. OCP as a function of humidity: : PS-PEM with the PD-ALD-deposited silica layers, MEA-1 (red), PS-PEM without the silica layers, MEA-2 (green), Nafion NRE-211 hot-pressed at 100ºC, MEA-3 (blue).

The conductivities of the MEA-1 and MEA-2 membranes are factors of 3.5 and 4.8, respectively, greater than that of the MEA-3 membrane at 95% humidity. However, we should mention that the MEA-3 membrane has passed through a hot-pressing step at 100°C (as part of its fabrication process), which is widely known to adversely affect Nafion conductivity. Our data on the MEA-3 membrane at high humidity closely matches data on a N-117 membrane heat-treated at 105°C in a study by Sone and colleagues [4]. At low humidity, however, the conductivity of the MEA-3 membrane is an order of magnitude higher than that of the heat-treated N-117. Data on non-heat-treated N-117 membranes from

Zawodzinski and colleagues [44] and Sumner and colleagues [43] are provided in Figure 4.16 for further comparison. The data suggest a conductivity of ~0.06 S cm^{-1} at 95% humidity for non-heat-treated Nafion, which is moderately less than the 0.08 and 0.11 S cm^{-1} conductivities associated with MEA-1 and MEA-2 membranes, respectively. Understanding the reasons behind the higher conductivity of the PS–PEM compared to Nafion requires detailed characterization of the PS–PEM, as well as a more concrete understanding of the Nafion structure and mechanisms of proton conductivity within its pores. Other than the morphological differences (size, shape, and tortuosity of the pores, as well as the pore wall properties) between the two membranes, the difference in number density of the sulphonate groups on the pore wall and the length and chemistry of their pendant groups are among the parameters that can affect proton mobility.

The current–voltage (I–V) performance of MEA-1 at different humidity levels is provided in Figure 4.18 and 4.19. The MEA delivered a maximum power density of 332 mW cm^{-2} at 70% humidity. However, operation at lower humidity led to a decline in performance, primarily due to an increase in activation overpotential losses resulting from an increase in charge transfer resistance within the catalyst layer due to Nafion dryout. Although the greater loss and its effect on the maximum power density was minimal at 55% humidity, further reducing the humidity to 25% resulted in a significant activation loss that led to ~30% decline in maximum output power. Operation at high humidity levels also led to performance degradation (Figure 4.19) as a result of partial water flooding of the cathode catalyst due to a low water evaporation rate. In addition to the I–V performance tests, an MEA was subjected to continuous operation at 150 mA cm^{-2} for 40 h. Other than a drop of 0.018 V during the first 5 h of operation (Figure 4.20a), believed to be mainly due to the system reaching a

steady state, the device showed an additional drop of 0.007 V over the remainder of the test period (0.18 mV h^{-1}). To determine if changes in the membrane proton conductivity were responsible for the observed drop in potential, a second test was carried out in which the membrane conductivity was measured frequently after periods of operation (Figure 4.20b). The results did not show any statistically significant change in membrane conductivity. The membrane conductivity does not therefore seem to be responsible for the decline observed in MEA performance.

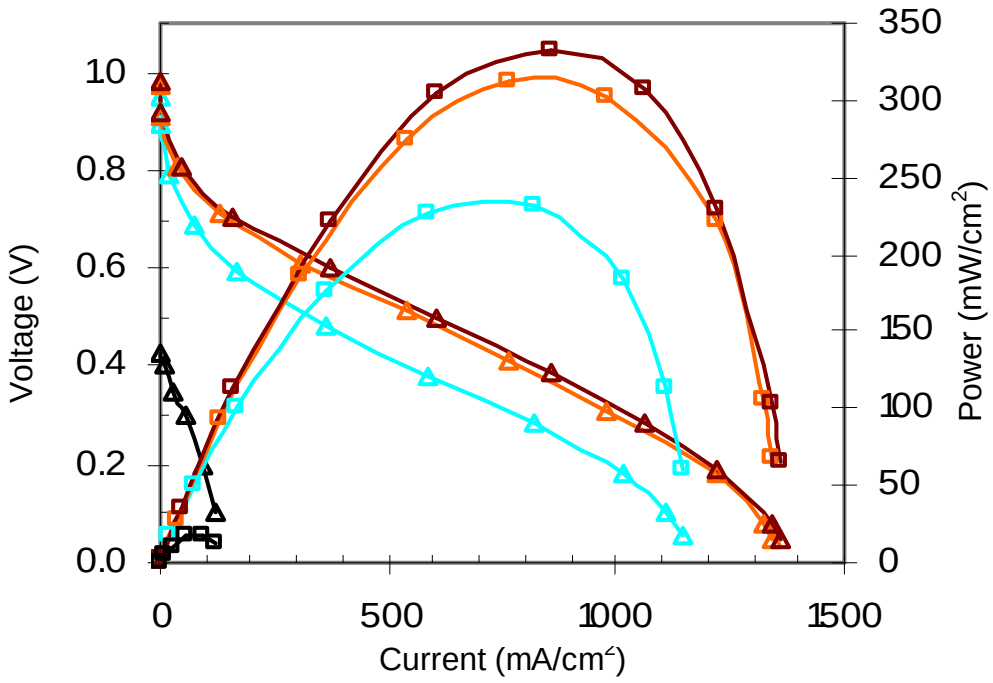

Figure 4.18. Voltage-current and power characteristics of MEA-1 at moderate and low humidity ambient: 70% (brown), 55% (orange), and 25% (cyan) and comparison with Pichonat and Gauthier-Manuel's PS-PEM (black). Performances of the PS-PEM membrane and MEA are tested at room temperature (~25ºC) with a dry hydrogen feed and air-breathing cathode.

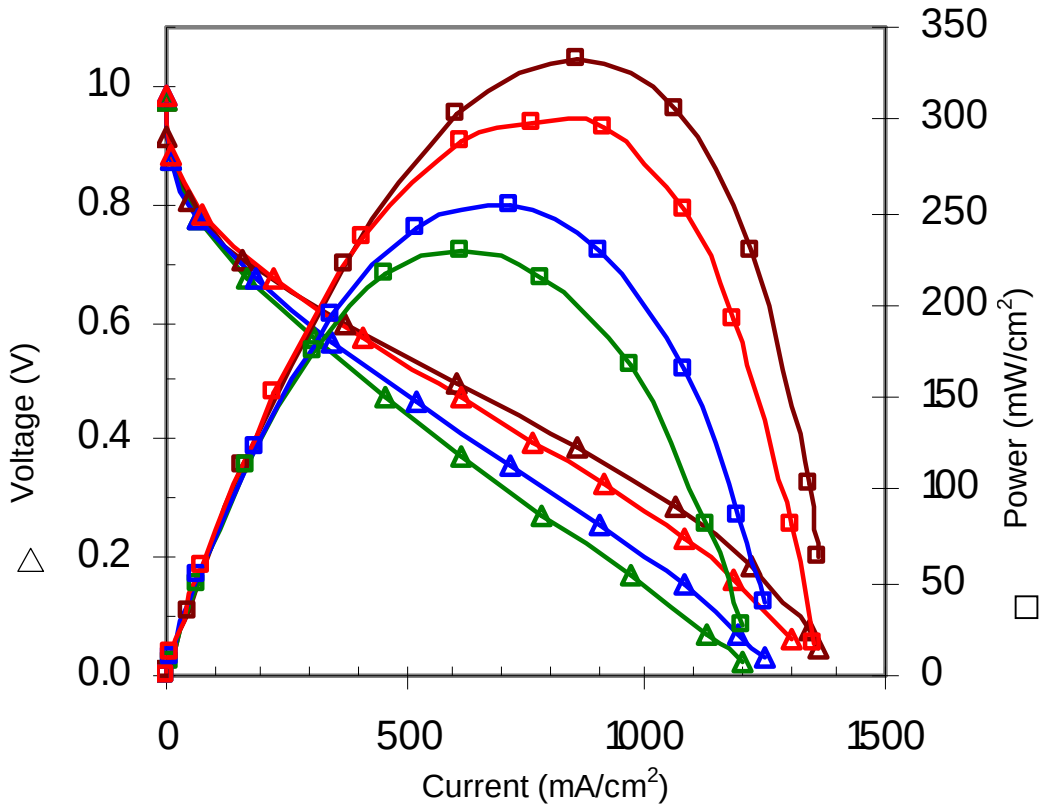

Figure 4.19. Effect of high humidity on MEA-1 performance: 95% (green), 92% (blue), 85% (red), and 70% (brown). The performances of the PS-PEM membrane and MEA are tested at room temperature (~25ºC) with a dry hydrogen feed and air-breathing cathode.

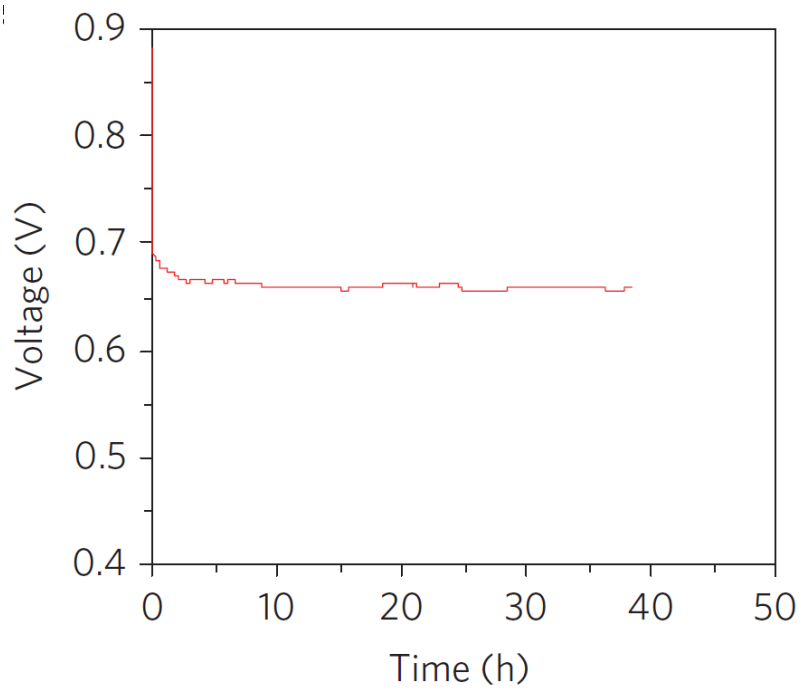

(a)

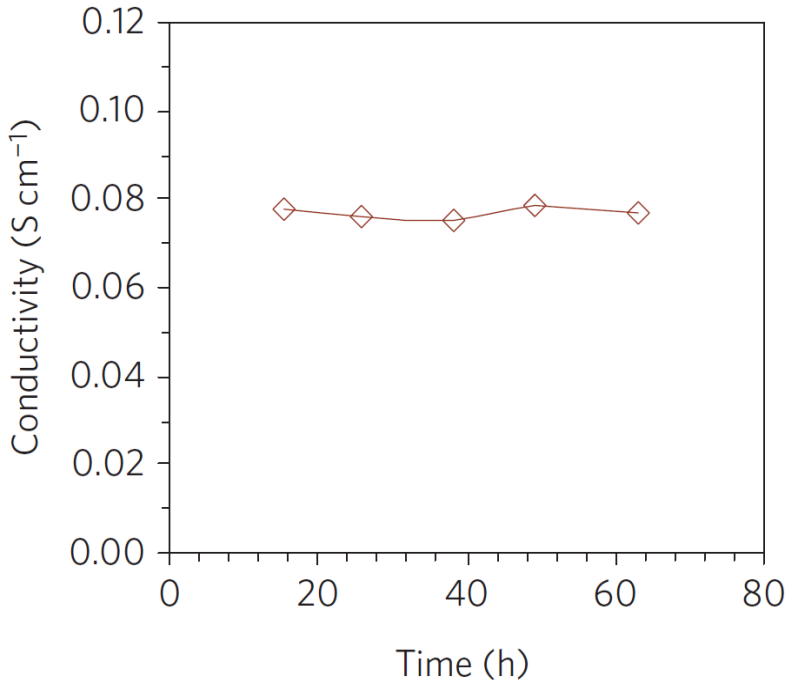

(b)

Figure 4.20. (a) Life test results at an operating current of 150 mA cm^{-2} and 75% humidity. **(b)** Membrane proton conductivity measured at different time periods after starting the test at 150 mA cm^{-2} operating current and 75% humidity.

4.9. Conclusion

We have reported the development of a next-generation PEM/MEA. The fixed geometry of the pores and asymmetric construction of the membrane allow high proton conductivity at low humidity levels. Owing to the many advantages of this PEM/MEA, we envision that this technology can simplify the fabrication and operation of small fuel cells. The fabrication processes developed to create the PS–PEM provide a versatile route to nanostructuring membranes with tailored properties for optimum performance. The ability to modify the surface of this dimensionally stable membrane opens up vast opportunities to fine-tune the characteristics of the membranes (for example, water and fuel transport through the membrane), enabling the development of better fuel cells. The technologies presented in this work can potentially be used for low-crossover membranes for liquid fuels, membranes for use in above ambient operating temperatures (120–140°C), anion exchange membranes, and so on. In addition, the known geometry of the pores and the ability to systematically control the pore surface chemistry with SAMs provide a unique opportunity to enhance our understanding of the physics of proton transport and its relation to pore size and surface properties.

4.10. Acknowledgements

Financial support for the UIUC team was provided by the Defense Advanced Research Projects Agency (DARPA). C.J.B. was supported through the US Department of Energy, Office of Basic Energy Sciences (grant DE-FG02-02-ER15368) and, Division of Catalysis and Division of Materials Sciences and Engineering. Y.B.J. was supported through the Sandia National Laboratories LDRD program. This work was carried out in part in the

Frederick Seitz Materials Research Laboratory Central Facilities, University of Illinois, which are partially supported by the US Department of Energy under grant nos DE-FG02-07ER46453 and DE-FG02-07ER46471. The authors would like to thank T. Spila, R. Haasch and V.V. Mainz for their assistance with the ToF–SIMS, XPS and NMR analysis, and G. Mensing for reviewing the paper. The help of R. Morgan and J. Jihyung in preparing catalysts is also appreciated.

4.11. References

[1] S. Gold, K. Chu, C. Lu, M. A. Shannon and R. I. Masel, "Acid loaded porous silicon as a proton exchange membrane for micro-fuel cells," *Journal of Power Sources,* vol. 135, pp. 198-203, 2004.

[2] T. Pichonat and B. Gauthier-Manuel, "Realization of porous silicon based miniature fuel cells," *Journal of Power Sources,* vol. 154, pp. 198-201, 2006.

[3] R. Devanathan, "Recent developments in proton exchange membranes for fuel cells," *Energy & Environmental Science,* vol. 1, pp. 101-119, 2008.

[4] Y. Sone, P. Ekdunge and D. Simonsson, "Proton conductivity of Nafion 117 as measured by a four-electrode AC impedance method," *Journal of Electrochemical Society,* vol. 143, pp. 1254-1259, 1996.

[5] J. Lin, P. Wu, R. Wycisk, P. N. Pintauro and Z. Shi, "Properties of water in prestretched recast Nafion," *Macromolecules,* vol. 41, pp. 4284-4289, 2008.

[6] K. A. Mauritz and R. B. Moore, "State of understanding of Nafion," *Chemical Reviews,* vol. 104, pp. 4535-4585, 2004.

[7] K. Schmidt-Rohr and Q. Chen, "Parallel cylindrical water nanochannels in Nafion fuel-cell membranes," *Nature Materials,* vol. 7, pp. 75-83, 2008.

[8] T. D. Gierke, G. E. Munn and F. C. Wilson, "The morphology in Nafion perfluorinated membrane products, as determined by wide- and small-angle X-ray studies," *J. Polym. Sci. Polym. Phys. Edn,* vol. 19, pp. 1687-1704, 1981.

[9] M. Kim, C. J. Glinka, S. A. Grot and W. G. Grot, "SANS study of the effects of water vapor sorption on the nanoscale structure of perfluorinated sulfonic acid (NAFION) membranes," *Macromolecules,* vol. 39, pp. 4775-4787, 2006.

[10] M. H. Litt, "A reevaluation of Nafion morphology," *Polymer Preprint,* vol. 38, pp. 80-81, 1997.

[11] H. -. Haubold, T. Vad, H. Jungbluth and P. Hiller, "Nano structure of NAFION: a SAXS study," *Electrochimica Acta,* vol. 46, pp. 1559-1563, 2001.

[12] L. Rubatat, G. Gebel and O. Diat, "Fibrillar structure of Nafion: matching Fourier and real space studies of corresponding films and solutions," *Macromolecules,* vol. 37, pp. 7772-7783, 2004.

[13] L. Rubatat, A. L. Rollet, G. Gebel and O. Diat, "Evidence of elongated polymeric aggregates in Nafion," *Macromolecules,* vol. 35, pp. 4050-4055, 2002.

[14] T. A. Zawodzinski, C. Derouin, S. Radzinski, R. J. Sherman, V. T. Smith, T. E. Springer and S. Gottesfeld, "Water uptake by and transport through Nafion® 117 membranes," *Journal of the Electrochemical Society,* vol. 140, pp. 1041-1047, 1993.

[15] K. Kreuer, S. J. Paddison, E. Spohr and M. Schuster, "Transport in proton conductors for fuel-cell applications: simulations, elementary reactions, and phenomenology," *Chemical Reviews,* vol. 104, pp. 4637-4678, 2004.

[16] N. Agmon, "The Grotthuss mechanism," *Chemical Physics Letters,* vol. 244, pp. 456-462, 1995.

[17] D. Marx, M. E. Tuckerman, J. Hutter and M. Parrinello, "The nature of the hydrated excess proton in water," *Nature,* vol. 397, pp. 601-604, 1999.

[18] T. A. Zawodzinski, M. Neeman, L. O. Sillerud and S. Gottesfeld, "Determination of water diffusion coefficients in perfluorosulfonate ionomeric membranes," *Journal of Physical Chemistry,* vol. 95, pp. 6040-6044, 1991.

[19] S. J. Paddison and R. Paul, "The nature of proton transport in fully hydrated Nafion®," *Physical Chemistry Chemical Physics,* vol. 4, pp. 1158-1163, 2002.

[20] S. J. Paddison, R. Paul and T. A. Zawodzinski, "Proton friction and diffusion coefficients in hydrated polymer electrolyte membranes: Computations with a non-equilibrium statistical mechanical model," *Journal of Chemical Physics,* vol. 115, pp. 7753-7761, 2001.

[21] P. Choi, N. H. Jalani and R. Datta, "Thermodynamics and proton transport in Nafion II. proton diffusion mechanisms and conductivity," *Journal of the Electrochemical Society,* vol. 152, pp. E123-E130, 2005.

[22] J. Perrin, S. Lyonnard and F. Volino, "Quasielastic neutron scattering study of water dynamics in hydrated Nafion membranes," *Journal of Physical Chemistry C,* vol. 111, pp. 3393-3403, 2007.

[23] G. L. Athens, Y. Ein-Eli and B. F. Chemelka, "Acid-functionalized mesostructured aluminosilica for hydrophilic proton conduction membranes," *Advanced Materials,* vol. 19, pp. 2580-2587, 2008.

[24] V. Lehmann, *Electrochemistry of Silicon: Instrumentation, Science, Materials and Applications.* Wiley-VCH, 2002.

[25] H. Föll, J. Carstensen and S. Frey, "Porous and nanoporous semiconductors and emerging applications," *Journal of Nanomaterials,* vol. 2006, pp. 1-10, 2006.

[26] J. A. Glass, E. A. Wovchko and J. T. Yates, "Reaction of atomic hydrogen with hydrogenated porous silicon detection of precursor to silane formation," *Surface Science,* vol. 348, pp. 325-334, 1996.

[27] P. Silberzan, L. Leger, D. Ausserre and J. J. Benattar, "Silanation of silica surfaces. A new method of constructing pure or mixed monolayers," *Langmuir,* vol. 7, pp. 1647-1651, 1991.

[28] C. P. Tripp and M. L. Hair, "An infrared study of the reaction of octadecyltrichlorosilane with silica," *Langmuir,* vol. 8, pp. 1120-1126, 1992.

[29] J. D. LeGrange, J. L. Markham and C. R. Kurkjian, "Effects of surface hydration on the deposition of silane monolayers on silica," *Langmuir,* vol. 9, pp. 1749-1753, 1993.

[30] C. P. Tripp and M. L. Hair, "Direct observation of the surface bonds between self-assembled monolayers of octadecyltrichlorosilane and silica surfaces: a low-frequency IR study at the solid/liquid interface," *Langmuir,* vol. 11, pp. 1215-1219, 1995.

[31] S. Onclin, B. J. Ravoo and D. N. Reinhoudt, "Engineering silicon oxide surfaces using self-assembled monolayers," *Angewandte Chemie International Edition,* vol. 44, pp. 6282-6304, 2005.

[32] P. Gupta, V. L. Colvin and S. M. George, "Hydrogen desorption kinetics from monohydride and dihydride species on silicon surfaces," *Physical Review B (Condensed Matter),* vol. 37, pp. 8234-8243, 1988.

[33] A. Halimaoui, Y. Campidelli, A. Larre and D. Bensahel, "Thermally induced modifications in the porous silicon properties," *Physica Status Solidi (b),* vol. 190, pp. 35-40, 1995.

[34] H. Sugiyama and O. Nittono, "Microstructure and lattice distortion of anodized porous silicon layers," *Journal of Crystal Growth,* vol. 103, pp. 156-163, 1990.

[35] R. Herino, A. Perio, K. Barla and G. Bomchil, "Microstructure of porous silicon and its evolution with temperature," *Materials Letters,* vol. 2, pp. 519-523, 1984.

[36] V. Labunova, V. Bondarenkoa, I. Glinenkoa, A. Dorofeeva and L. Tabulinaa, "Heat treatment effect on porous silicon," *Thin Solid Films,* vol. 137, pp. 123-134, 1986.

[37] P. Gupta, A. C. Dillon, A. S. Bracker and S. M. George, "FTIR studies of H_2O and D_2O decomposition on porous silicon surfaces," *Surface Science,* vol. 245, pp. 360-372, 1991.

[38] Y. Ogata, H. Niki, T. Sakka and M. Iwasaki, "Oxidation of porous silicon under water vapor environment," *Journal of the Electrochemical Society,* vol. 142, pp. 1595-1601, 1995.

[39] T. I. Gorbanyuk, A. A. Evtukh, V. G. Litovchenko, V. S. Solnsev and E. M. Pakhlov, "Porous silicon microstructure and composition characterization depending on the formation conditions," *Thin Solid Films,* vol. 495, pp. 134-138, 2006.

[40] R. K. Iler, *The Chemistry of Silica.* Wiley: New York: 1976.

[41] C. J. Brinker and G. W. Scherer, *Sol-Gel Science: The Physics and Chemistry of Sol-Gel Processing.* Academic Press, Inc.: New York: 1990.

[42] Y. Jiang, G. Xomeritakis, Z. Chen, D. Dunphy, D. J. Kissel, J. L. Cecchi and C. J. Brinker, "Sub-10 nm thick microporous membranes made by plasma-defined atomic layer deposition of a bridged silsesquioxane precursor," *Journal of American Chemical Society,* vol. 129, pp. 15446-15447, 2007.

[43] J. J. Sumner, S. E. Creager, J. J. Ma and D. D. DesMarteau, "Proton conductivity in Nafion 117 and in a novel Bis[(perfluoroalkyl)sulfonyl]imide ionomer membrane," *J. Electrochem. Soc.*, vol. 145, pp. 107-110, 1998.

[44] T. A. Zawodzinski, T. E. Springer, J. Davey, R. Jestel, C. Lopez, J. Valerio and S. Gottesfeld, "A comparative study of water uptake by and transport through ionomeric fuel cell membranes," *Journal of Electrochemical Society*, vol. 140, pp. 1981-1985, 1993.

CHAPTER 5:

ALTERNATING CURRENT TRAVELING WAVE MEMBRANES FOR NANOSCALE COLLOIDAL SEPARATIONS

5.1. Introduction

Source waters are known to contain large suspended solids, apart from dissolved salts. A significant fraction of these suspended solids exists as colloidal suspension and these would typically pass through the standard 0.45 μm pore in an SDI test filter. Moreover, the colloidal suspension has a tendency of irreversibly fouling RO membranes and this directly leads to energy losses, increased pressure in the system, and reduced filtering capacity [1, 2]. Natural waters are known to contain colloids in both inorganic (silica) and organic (carbohydrates and lipids) forms [3, 4]. Their concentration in water has been estimated at up to 10^9 particles per milliliter, occurring in sizes of up to 120 nm [4, 5]. Particles in colloidal length scales are stable in suspension and cannot be removed by gravimetric means. However, these colloids are known to possess net negative surface charge due to deprotonation of surface silanol (Si-OH) in the mildly alkaline pH of 7-8 [6]. This surface charge could be employed to transport and filter out suspended colloids from solution by means of an electric field.

In this study, microfluidic devices with a traveling electrode membrane are developed for the purpose of colloidal separations with a particle size in nanoscale. An alternating

---

The content in this chapter is adapted from the published articles as follows;

- E. Pengwang, B.R. Flachsbart, X. Jin, N.R. Aluru, and M.A. Shannon, "Design and Fabrication of AC Traveling Wave Membranes for Nanoscale Colloidal Separation," *Langmuir*, (submitted October 2011).

current (AC) electrokinetic technique is implemented to create non-uniform electric field with spatial phase variation to manipulate colloidal transportation. Engineering design rules and simulation tools are also implemented to forecast separation of colloids using a traveling waveform on charged particles. With differences in AC spatial voltage supply, electrokinetics of charged particles are studied for transport across the nanochannels in a special membrane. With standard techniques of microfabrication and polymer processing, the development of this AC traveling wave membrane is investigated. In this study, the membrane consists of embedded electrodes in a thin layer of SU8 material, acting as an electrical insulator. The process of sputtering the electrode material, followed by dry plasma etching with high voltage creates nanochannels through the membrane. In this chapter, detailed information on an AC traveling wave membrane is presented for the removal of particles and colloids below 0.1 microns in size. The initial objective here is to prove the concept using larger sized colloids and transport them through a selective nanoporous membrane, before moving to smaller particle sizes. The final objective is to develop the experimental apparatus to evaluate permselective membranes and optimize electrode biasing such that various sized colloids can be collected and pumped across the membrane. To enable a design optimization of the AC electrokinetic-based particle separator, we will also develop simulation tools and test their accuracy in predicting the transport and separation of colloids through this alternating permselective membranes in the presence of AC fields.

5.2. Materials and Methods

5.2.1. Traveling Waveform Membrane

The supplied voltage for an alternating current (AC) electrokinetic-based separation scheme can be formulated as a function of wavelength (λ) and frequency (*f*) for a specific location (*x*) and time (*t*) as shown in Equation 5.1, where ϕ_0 is the amplitude, *f* is the frequency of the AC signal, *k* is a wavelength constant, and ω is a radian frequency.

$$\phi = \phi_0 \sin(\frac{2\pi}{\lambda} x - 2\pi ft) = \phi_0 \sin(kx - \omega t) \tag{5.1}$$

In this case, multiple electrodes can be used for multi-stages of separation. The phase and amplitude of the AC voltage can be modified to manipulate the motion of nanoscale colloids as formulated in this equation as well. The schematic diagram and layout of the biasing for traveling waveform membrane across the nanochannel are shown in Figure 5.1. The blended structure of SU8 polymer and titanium electrodes is supplied with spatial AC signals. Also, a coating layer is used, represented in red, to prevent stiction of the colloids to the membrane structure. In the top view, the device consists of a feed stream, a permeate stream, a clean stream, and a rejectate stream as shown in Figure 5.1(b).

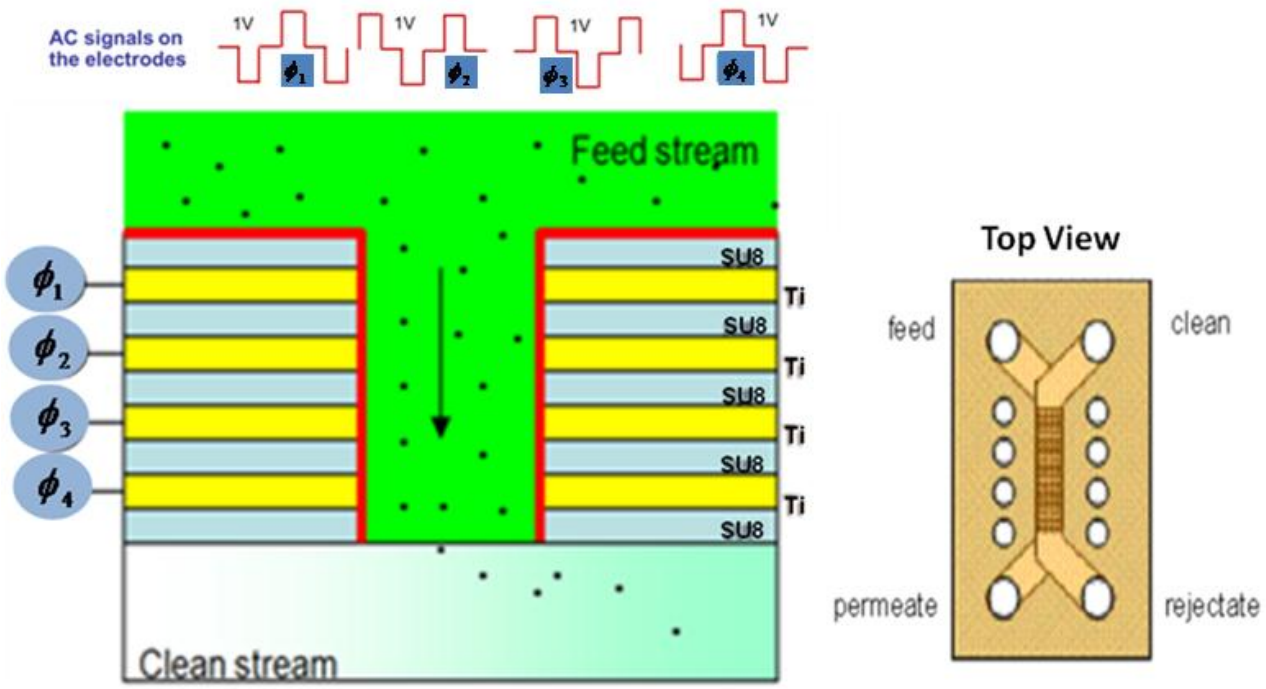

(a) (b)

Figure 5.1. Front view of a device with a traveling wave membrane for separating colloids (a); top view of the device with inlet/outlet for feed and clean stream (b).

One of the assumptions to manipulate colloids is to use a generated group velocity of the waveform based on the telegraph equation. With four different phases of AC voltage to consecutive electrodes, a waveform of colloids is formed. The generating phase velocity (v_p) and group velocity (v_g) of a wave can be expressed as a rate at which the phase of the wave propagates in the medium. They are given in terms of the wavelength (λ), frequency (f), wavelength constant (k) and radian frequency (ω) as shown in Equation 5.2.

$$v_p = \lambda f = \omega / k \quad \text{and} \quad v_g = \frac{d\omega}{dk} \tag{5.2}$$

5.2.2. Electrokinetics of Nanoscale Particles

Electrokinetics of nanoscale particles have been studied under the influence of various AC voltages [7-13]. Depending on the conductivity of the solution, size of particle, and operating frequency, many patterns of electric field can be used to manipulate colloids in both micro and nanoscale. In summary, two main characteristics can be used to manipulate colloids; fields that effect the particle, and fields that effect the fluidic motion.

Based on the research of particle transportation, behavior of polarizable colloids can be manipulated by a traveling wave dielectrophoresis. By applying a sequences phase shift of 90° to consecutive electrodes, traveling wave techniques have been implemented in several studies to manipulate polarizable colloids in aqueous solutions. Traveling wave dielectrophoresis force can induce a motion of particles along traveling electric field for colloids such as blood cells [14-16], pollen, cellulose particles [17], yeast cells [18], polystyrene latex beads [19-21], and cancer cells [22]. An example of conventional dielectrophoresis trapping of nanoscale particles is demonstrated at the field gradient maximum located at the edge of the electrode. The investigation was tested with an AC voltage supply of 1 V and 20 MHz for charged latex spheres [20]. The device was designed with an electrode gap of 4 μm in a water medium of 18 mS m^{-1} conductivity. Moreover, different behavior of colloidal transport can be observed, such as electrolysis (at high voltage), reverse pumping and forward pumping with recirculation speed up to 100 μm/sec with high voltage and frequencies in 1-10 kHz. Principles and mechanisms of dielectrophoretic separation have been extensively studied [23-30]. The theoretical dielectrophoretic force for arrays of electrodes can be represented as a function of

permittivity for the particles and suspending medium (ε_p, ε_m), conductivity of the particles and medium (σ_p, σ_m), AC frequency (f), radius of the particle (r), periodic distance between electrodes of the same phase (λ), and electric field ($\tilde{E}$). Dielectrophoretic force generated from interactions of non-uniform electric fields and a change in dipole moment of the particle can be formulated. The time-averaged force on the particles is shown in Equation 5.3. The first term ($\nabla(\tilde{E}\cdot\tilde{E}^*)$) results to in-plane motion, governed by conventional dielectrophoretic force that can be simplified to Equation 5.4. The second term ($\nabla\times(\tilde{E}\times\tilde{E}^*)$) results to motion along the travelling electric field, also known as a traveling wave dielectrophoretic force that can be simplified as Equation 5.5, where the factor f_{CM} is the Clausius-Mossotti factor as shown in Equation 5.6 for a spherical particle.

$$< F >= 4\pi\varepsilon_m r^3\left(\frac{1}{4}\mathrm{Re}[\nabla(\tilde{E}\cdot\tilde{E}^*)]-\frac{1}{2}\mathrm{Re}[\nabla\times(\tilde{E}\times\tilde{E}^*)\right) \tag{5.3}$$

$$< F_{DEP} >= 2\pi\varepsilon_m r^3\cdot\mathrm{Re}[\,f_{CM}\,]\cdot\nabla\left|\tilde{E}^2\right| \tag{5.4}$$

$$< F_{twDEP} >= -\frac{4\pi^2\varepsilon_m r^3\cdot\mathrm{Im}[\,f_{CM}\,]\cdot\tilde{E}^2}{\lambda} \tag{5.5}$$

$$f_{CM}=\frac{\varepsilon_p^*-\varepsilon_m^*}{\varepsilon_p^*+2\varepsilon_m^*}\qquad\text{where}\qquad\varepsilon^*=\varepsilon-j\left(\frac{\sigma}{2\pi f}\right) \tag{5.6}$$

The real and imaginary parts of f_{CM} give the in-plane and out-of-phase components of the dipole that determine the conventional dielectrophoretic behavior and the traveling wave dielectrophoretic behavior. At low frequencies, the Clausius-Mossotti factor is dominated by the conductivity of the medium and particle. At high frequencies, the Clausius-Mossotti factor is dominated by the permittivity of the medium and particle. When an imaginary part of the Clausius-Mossotti function is maximized, the real part of the Clausius-Mossotti

function is reduced to close to zero. Thus, a dielectrophoretic force is minimized when a traveling wave dielectrophoresis membrane is operated at its cutoff frequency.

Another AC electrokinetic effect for colloid transportation is fluid motion; this is also referred to as electroosmosis in many publications. Electroosmosis causes the fluid movement beyond the shear plane by the movement of the charge with respect to the liquid, while dielectrophoresis phenomenon dominates the movement of colloids when the charge movement is within the Stern and the diffusion part of the double layer [31]. In many cases of electrophoretic phenomenon, the motion of the nanoparticle and the movement of liquid will be governed by the electric field and the Coulomb effect on its charge [32, 33]. Principles and mechanisms of AC electrokinetic separation have been studied with various techniques; circular arrays [34, 35], asymmetric electrode array [36-41], and linear traveling wave methods [31, 35, 42, 43]. Since electrophoresis effects are stronger when the particle is small and the ratio of charge to mass is high, motion of nanoscale charged particles by electrophoresis effects is as important as dielectrophoresis phenomenon [44]. Since the colloids, proteins, and humic substances are primarily negatively charged, they will pass through membranes and concentrate at the end of the patterned electrodes. Since small ions can freely pass through the nanopore in both directions, the electrode solution will remain essentially neutrally charged, and Faradic redox reactions at the electrodes will not be required to drive the transport.

In this chapter, AC electrophoresis is studied because a well-known technique of DC electrophoresis is with well-understood limitations. Charged particles can be drawn across a permselective membrane with sufficiently high DC voltages applied at the driving electrodes with the drawback on energy consumption. Although electrokinetics of colloids with

alternating current (AC) has not been extensively studied, the promising aspect of implementing AC over DC field is to overcome typical electrochemical issues such as concentration polarization and electrolysis. In our proposed technique, an alternating voltage below the electrolysis limit is applied to the electrodes, with adjacent electrodes at a different sequential phase, but the same magnitude. However, in AC electrokinetics, the AC electric field is required to be sufficient for transporting colloids across the membrane. Therefore, fabricating a nanostructured membrane with a small gap between each electrode can be one technique that is energetically favorable for nanoscale colloidal separation. Hence, AC currents, with relatively low losses, can be used to separate smaller particles.

The mathematical model for particle transport involves a set of equations governing electric force, fluid flow, and particle motion. The motion of a solid particle is influenced by the fluid flow equation, governed by the Navier-Stokes (Equation 5.7), continuity equation (Equation 5.8), and Newton's equation (Equation 5.9), where p is the hydrostatic pressure, μ is the fluid viscosity, and $\mathbf{f}$ is the body force including the electric body force due to the space charges and the forces from the particles, m_{p} is the mass of the particle, $\mathbf{u}_{\mathrm{p}}$ is the velocity of the particle, F_{E} is an electrostatic force acting on the particle, and F_{D} is the drag force from the fluid.

$$\rho\left(\frac{\partial \mathbf{u}}{\partial t}+\mathbf{u}\cdot\nabla\mathbf{u}\right)=-\nabla p+\mu\nabla^{2}\mathbf{u}+\mathbf{f} \tag{5.7}$$

$$\nabla\cdot\mathbf{u}=0 \tag{5.8}$$

$$\frac{d\left(m_{p}\mathbf{u}_{p}\right)}{dt}=F_{D}+F_{E} \tag{5.9}$$

For DC electrophoresis, the mobility of particles is controlled by Stoke's law when the interactions between the charged particles are ignored. The Henry formula can be used to express the movement of the particle, but it is valid only for low zeta potential. Moreover, the Dukhlin-Semenikhin formula is used for the transport of particles with thin double layer (κa >> 1) in a symmetric electrolyte solution. An approximation of the mobility can thus be made as: $u_p = \frac{2\varepsilon_0 \varepsilon_r \zeta}{3\eta}$ and $u_p = \frac{\varepsilon_0 \varepsilon_r \zeta}{\eta}$ for low and high κa value when the particles encounter the DC electrophoretic field. Moreover, from the Helmholtz-Smoluchowski equation, Morgan *et al*. [43] suggested an approximation for fluid velocity by using an AC potential drop across the diffusion double layer and the tangential electric field outside the double layer for an AC electric field. However, the Helmholtz-Smoluchowski theory only explains the relationship between zeta potential and electrophoretic mobility [45] when the particle radius is much greater than the Debye length (κa >> 1) and the influence of surface conductance is ignored.

In our experiment, particle radius is smaller than the values of Debye length (κ^{-1}) calculated from electrolyte concentration. For example, the Debye length can be approximated in the range of 200-300 nanometers in deionized water as shown in Table 1. This phenomenon can be distinguished from previous work that mostly investigated the effect of electric field for the particles larger than 1 μm in diameter. In the case of a small Debye length (κa >> 1), dielectrophoresis is claimed to govern the movement of colloids. Reducing the thickness of the double layer will result in increasing the retardation force from the particle surface. When the double layer is thicker than the particle size, the retardation force is less. In our case of a smaller particle size (κa < 1), many parameters can be studied

for the behaviors of AC electrokinetics and electrophoresis transport: such as the surface charge of particles, electric field, medium viscosity, surface conductivity, size of particle, Dukhin number, and zeta potential.

Table 5.1: Ranges of electrolyte conditions and Debye length (κ^{-1})

Electrolyte Conditions	**DI water**	**10^{-3} M NaCl Solution**	**0.1 M NaCl Solution**	**Sea water**
Debye length (nm)	~200-300	10	1	~0.2-1

Surface conductivity and surface charge density of particles have been widely studied for particle transport [45-50]. In general, the surface conductivity for a latex sphere is approximated for a particle larger than 1 μm by the equation $\sigma_p = \sigma_b + 2K_s / a$ where $\sigma_b = 0$ for bulk conductivity and K_s is surface conductance. In general, surface conductivity of dispersed particles is associated with ionic motion above the slipping plane in the double layer. In this case, the value of the surface conductivity depends on the ζ-potential, which is valid for a symmetrical electrolyte with equal ionic diffusion coefficient. Zeta potential can also affect the surface charge density and stability of colloidal dispersions. Colloids with a high zeta potential are electrically stabilized while colloids with a low zeta potential tend to coagulate or flocculate. Furthermore, the concentration of ions and conductivity of the electrolyte solution are also important for determining the surface charge density of a particle. In general, the Dukhin number can be used to represent a dimensionless number that

can compare the effect of surface conductivity to the bulk electrical conductivity. Hence, the Dukhin number is an important parameter in the study of nanoscale colloid transportation within an AC electrophoretic field.

5.3. Numerical Simulations

We have developed simulation tools to predict the separation of colloids using a travelling waveform on nanoscale particles. Using OpenForm® software to simulate the motion of colloids with 100-150 nm in diameter, the movement of charged nano-particles has been studied in a system with two microchannels interconnected by a nanopore. Interdigitated electrode arrays are placed on the surface of the pore, as shown in Figure 5.2(a). The pore is 4 μm wide and 5 μm long. Charged particles are subjected to electrostatic forces, particle-particle interaction forces, and drag forces from the fluid. In the simulation, the amplitude of AC signal is 1 V. Figure 5.2(b) shows the velocity of a single particle at various frequencies. At the same frequency, a smaller particle moves slower than a larger particle. There is an optimal frequency for the particle to pass through the pore. At frequencies higher than the optimal frequency, the particle is pulled forward and backward by the wave because the particle moves slower than the wave's velocity. The optimal frequency for a 100 nm particle is around 30 kHz. Results from simulations showed that the colloids can be moved across an embedded electrode membrane with traveling waveform. Figure 5.3 shows the snapshots of a pack of particles at different times when the operating frequency is 30 kHz.

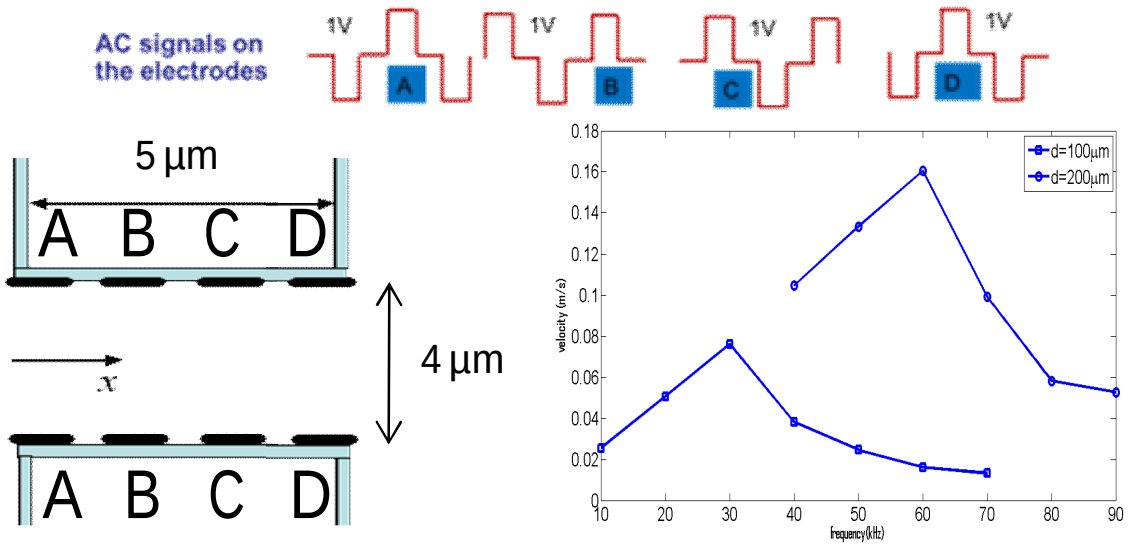

(a) (b)

Figure 5.2. Numerical simulation of particle movement under a traveling waveform: (a) simulation setup, and (b) velocity variation with frequency.

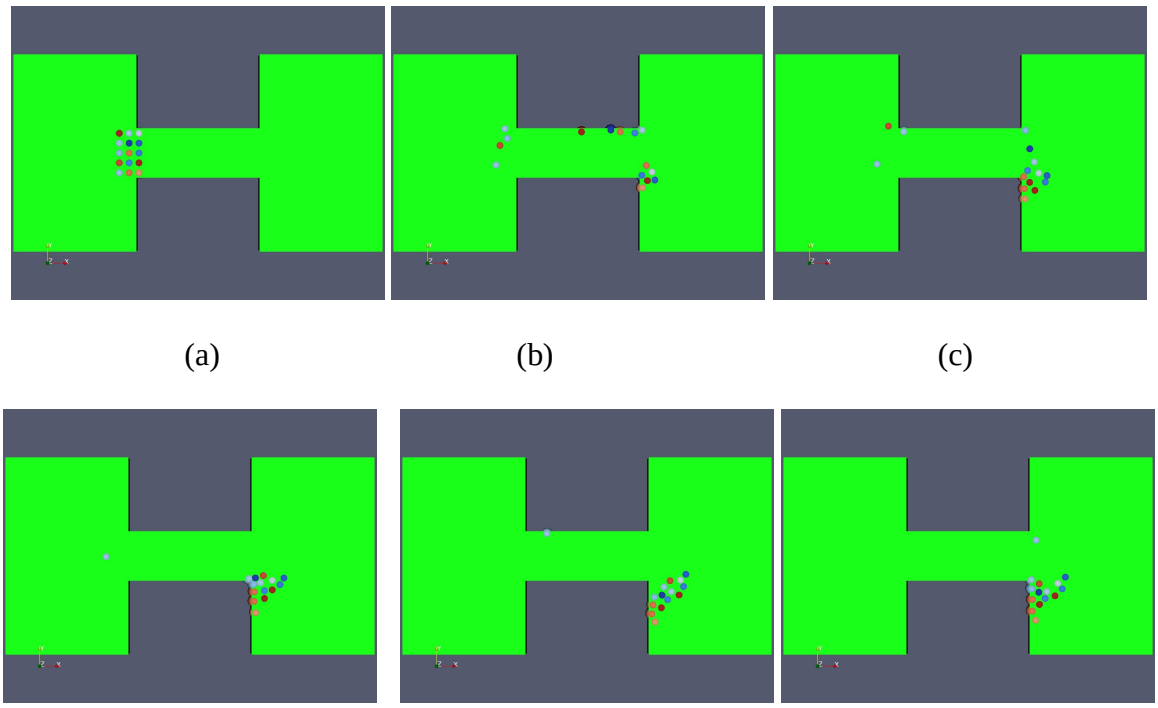

(a) (b) (c)

(d) (e) (f)

Figure 5.3. Snapshots of a pack of particles moving under a traveling wave when the frequency is 30 kHz. (a) t=0 s, (b) t=50 μs, (c) t=100 μs, (d) t=150 μs, (e) t=200 μs, (f) t=250 μs.

5.4. Microfabrication

In order to improve the transportation of colloids, we will improve the fabrication of our MEMS-based travelling electrode membranes. With a fluidic channel through a series of electrodes, spatial phase variation can be studied to improve the transport of colloids from the feed stream to the clean stream. The first generation of traveling electrode membrane consists of five layers of 1 μm thick SU8 epoxy-based negative photoresist alternating with four layers of 50 nm thick titanium electrode (all made using standard MEMS processes); five layers of SU8 and four layers of titanium. The through channels are made in the SU8 / titanium stack by plasma etching with SF_6 and oxygen gas [51].

The top and bottom layer of the microchannel was created by using two layers of SU8 materials before a traveling wave membrane. The first layer was created on a cleaned glass substrate with P6 release layer by actively dispensing at a spinning speed of 2000 rpm for 30 seconds and hardbaking at 140°C for 2 minutes. Then, SU8 was casted on the top of P6 layer for a thickness of 150 μm at temperature of 80°C for 4 hours. The mask pattern with inlet/outlet only (without the microchannel) was exposed on the casted SU8 for 40 seconds. The assembly was then baked at 75°C for 4 minutes and 110°C for 4 minutes before developing a pattern on SU8 developer in ultrasonic bath for 1 minute. The patterned SU8 was released in water after 24 hours and cleaned. The fabrication flow for microchannel layers is shown in Figure 5.4. The other layer with the microchannel was then prepared following the same procedures, except releasing the membrane from the glass substrate in the last step. Then, the first layer of inlet/outlet was bonded to the layer of the microchannel by using a transferred epoxy technique. An adhesive layer of 1 μm thick SU8 was spincoated on a PDMS puck at 2000 rpm. This SU8 was pressed to the microchannel layer for 1 minute and

then peeled out. As a result, the adhesive layer adhered to the microchannel layer at a contact region. Then, the microchannel was baked at 110°C for 2 minutes to remove any solvent before aligning it with the released layer with inlet/outlet. The assembly was then bonded with an EV501 bonder using a 200 N force at a temperature of 85°C for 5 minutes. After bonding, the assembly was exposed to UV light at 20 mW cm^{-2} for 40 seconds and baked at 110°C for 4 minutes to complete the bonding processes. Last, the assembled part was then released in water after 24 hours.

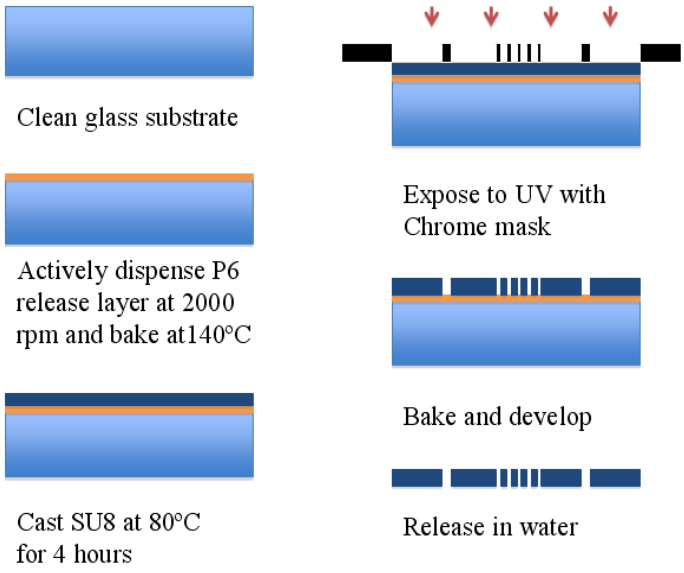

Figure 5.4. A microfabrication process of microchannel layer with inlet, outlet, and microfluidic pathway

The traveling wave membrane was created on a cleaned glass piece with a P6 release layer similar to the microchannel. Then, a layer of SU8 was spincoated on the glass at 2000 rpm for 30 seconds. The thickness of the SU8 layer was 1µm for this procedure. The glass piece was then pre-baked at 110°C for 4 minutes, exposed at 20 mW cm^{-2} for 20 seconds, and post-backed at 110°C for 4 minutes. The glass piece was then sputtered with titanium at

the rate of 54°A/min for 10 minutes to create the first electrode layer. This metal was then selectively coated with aluminum to create an etch stop for final electrical connection. Then, the assembly was cleaned with oxygen plasma RIE for 10 seconds to remove any debris before applying more layers of SU8. This process was repeated until the number of electrodes and insulator layers was four and five respectively. The fabrication flow for this multi-layer traveling wave membrane is shown in Figure 5.5. The overall thickness of the membrane is about 5.2 µm (5 µm SU8 and 0.2 µm for metal electrodes). Then, the assembly was coated with aluminum entirely and patterned with photoresist for opening windows of 4 um in diameter. After hardbaking, the assembly was then etched by a plasma etching with SF_6 5 sccm and O_2 50 sccm at 30 mTorr, 800W power supply. Images of fabricated membrane with holes of 4 µm in diameter after etching through are shown in Figure 5.6.

The traveling wave membrane was then transferred from the glass substrate to the top microchannel by the same transferred epoxy techniques and thermal bonding as discussed in a microchannel layer. The releasing processes were developed [52] to ensure that the membrane is strong enough and not broken for the water releasing processes. After releasing from the glass substrate, the bottom microchannel was used to sandwich the traveling wave dielectrophoresis membrane by the same transferred epoxy and thermal bonding processes. The device was then connected to flexible tubes for inlet/outlet by using two-part-epoxy (3M, USA).

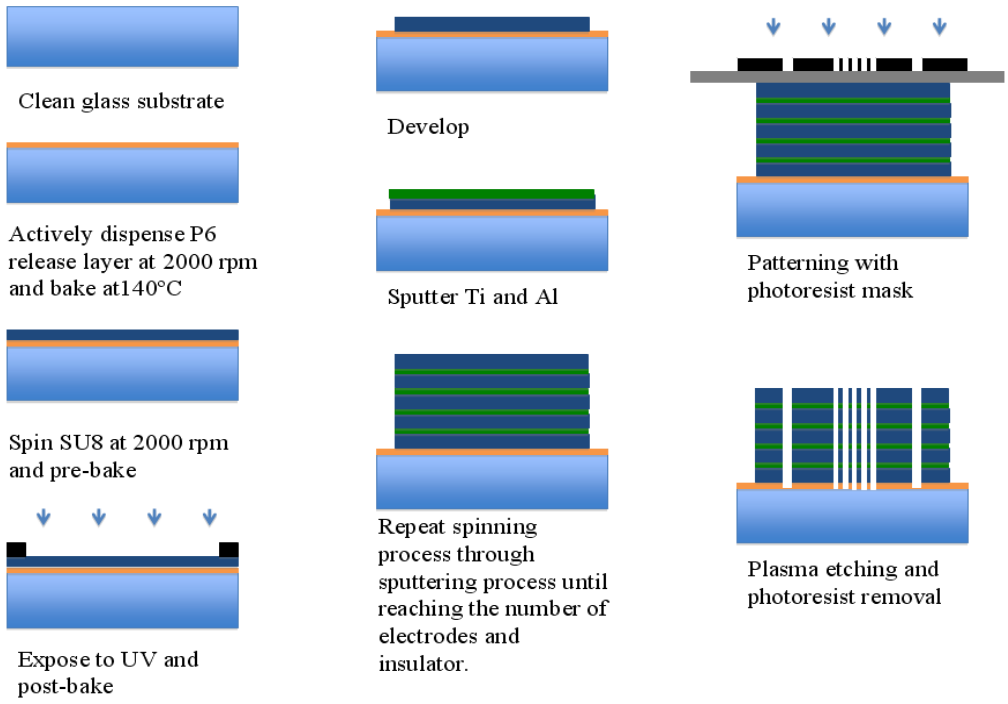

Figure 5.5. A microfabrication process for a multi-layer of travelling wave membrane is made of SU8 material and titanium electrodes.

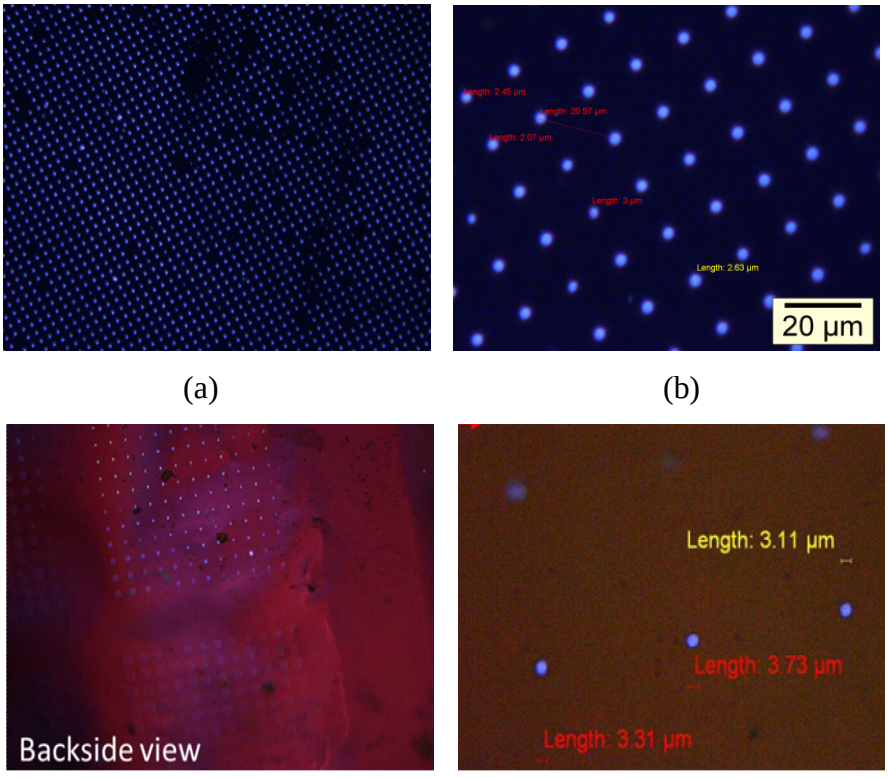

(a) (b)

(c) (d)

Figure 5.6. An image of etched hole of titanium layer and SU8 layer after plasma etching for a membrane with ~2-4 µm opening at low magnification (a), at 50x magnification with a backlight (b), backside view of a traveling membrane after etching and releasing processes (c), at 50x magnification with a backlight (d).

5.5. Experimental Results

Investigation of colloidal transport was observed through motion detection of fluorescent particles in the test assembly. An Agilent 33220A function generator was connected to a Tektronix TDS 6848 oscilloscope and to an electrical circuit box that creates the phase separated traveling waveform. The signals with 90 degree phase difference from the circuit box was then supplied to each layer of membrane and the channel was observed

under a Leica DMIRE inverted fluorescent microscope with a FITC-L5 (excitation of 480 nm, emission of 527 nm) filter and the Image-Pro Plus® software as a image recording.

A solution of DI water with 200 ppm concentration of 93 nm fluorescent latex colloids (Product number FC02F/8972 manufactured from Bangs Laboratories, Fishers, IN) was prepared for the feed stream. The particle conductivity is unknown. The particle surface charge is -209 μeq/gram or -3.3 μC/cm^2 (given from the manufacturer's documentation). The chemical group of this fluorescent microsphere is a carboxyl P(S/V-COOH) functional group with a dragon green color and the same range of fluorescent lens (excitation of 480 nm, emission of 520 nm). In the experiment, the medium conductivity (in deionized water) is 0.05 mS/m, measured by a conductivity meter. The voltage supply is 1 V, the relative permittivity of the medium is about 80, the relative permittivity of the particles is about 2.5, and the flow velocity of the feed and clean streams is 0.03 μL/min equally.

Before supplying the traveling wave voltages, no change in the clean stream was observed for any motion of colloids. After supplying the voltages, the testing result showed dissipation from the end of the microchannels as shown in Figure 5.7. Although the velocity of 100 nm colloids was expected to be optimal at 30 kHz for 100 nm particle, we found that it was difficult to distinguish a difference in colloid motion in the range between 100 Hz and 1MHz. Probably, this occurred because of interactions between the particles.

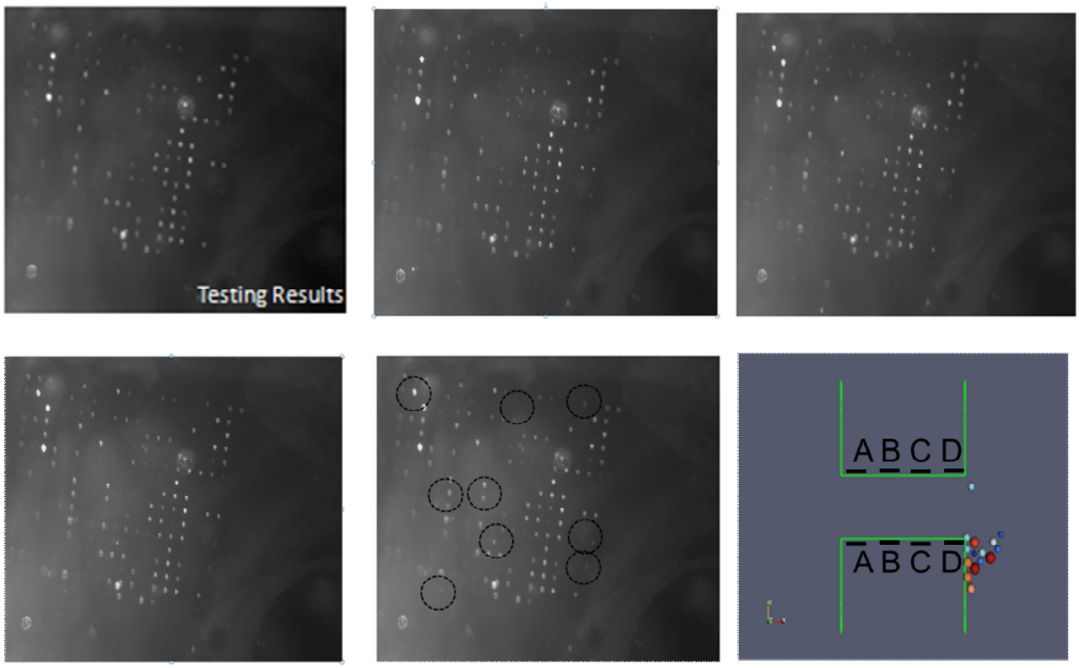

Figure 5.7. Snapshots from experimental results of a four-electrode membrane, compared to the previous simulation results. The membrane transported 93 nm diameter colloids through the membrane with traveling wave electrodes, and most of the colloids tended to stick to the end of the microchannel of the fabricated device.

5.6. AC Electric Field Induced Micro-mixing

The traveling wave membrane can pump particles across the membrane, but both simulations and experimentation show that particles will collect at the exit of the pore, sticking to the end of the microchannel. Hence, several bias schemes are investigated in this study to remove colloids at the end of the microchannels. In order to facilitate the propagation of electric fields into the bulk electrolyte and depolarize these electrodes, a new scheme is proposed. We learn that an AC electric field applied on the microelectrodes can also induce fluid flow to form a micro mixing phenomena at the electrode-electrolyte interface [8, 53-57]. Hence, we study the effect of surface electrodes by replacing a single

electrode at the end of microchannel with a surface interdigitated electrode. The electrodes on the surface would set up a local AC electroosmotic flow that should carry away approaching charged particles, and improve particle collection in the clean stream. The schematic of this concept is shown in Figure 5.8.

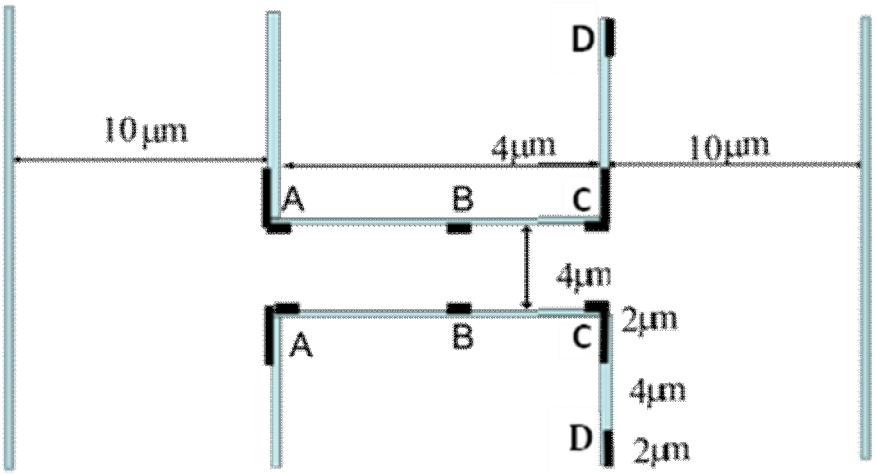

Figure 5.8. Testing configurations for traveling waveform with additional traveling electrodes at the surface of the microchannel on a clean stream.

Using a simulation from OpenForm® software, we studied an AC electric field with a traveling waveform on the sidewall at the entrance/ exit surface electrodes. The simulation shows the motion of colloids with different sizes (~100-150 nm) across the 5 μm thick traveling electrode membrane with surface electrode as shown in Figure 8. Computational results of applying the AC traveling wave signals at these microelectrodes are depicted in Figure 5.9. In summary, about 85% of particles appear to be collected in the right chamber after 5 milliseconds of simulation when the electrodes are at the surface and the colloids are at the entrance. The simulation also shows that charged particles are carried away from the

pore by the surface electrode at the end of the pore. However, if nanoscale colloids are dispensed far away from the entrance, it will take longer time for them to transport across the traveling wave membrane. With the same simulation, about 25% of particles appear to be collected in the right chamber after 40 milliseconds of simulation as shown in Figure 5.10.

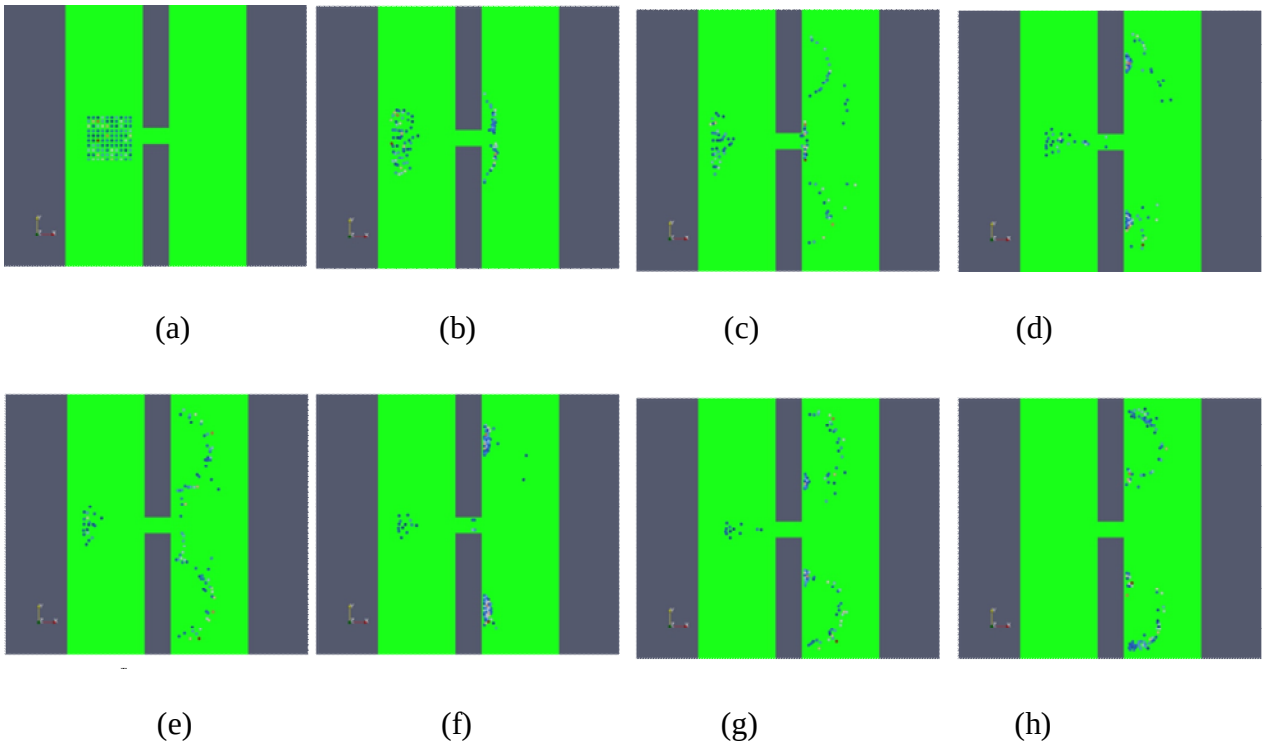

Figure 5.9. Snapshots from simulations of colloids that are close to the entrance across a traveling wave membrane with surface electrodes at (a) 0 ms, (b) 0.5 ms, (c) 1 ms, (d) 2 ms, (e) 3 ms, (f) 4 ms, (g) 5 ms, and (h) 20 ms.

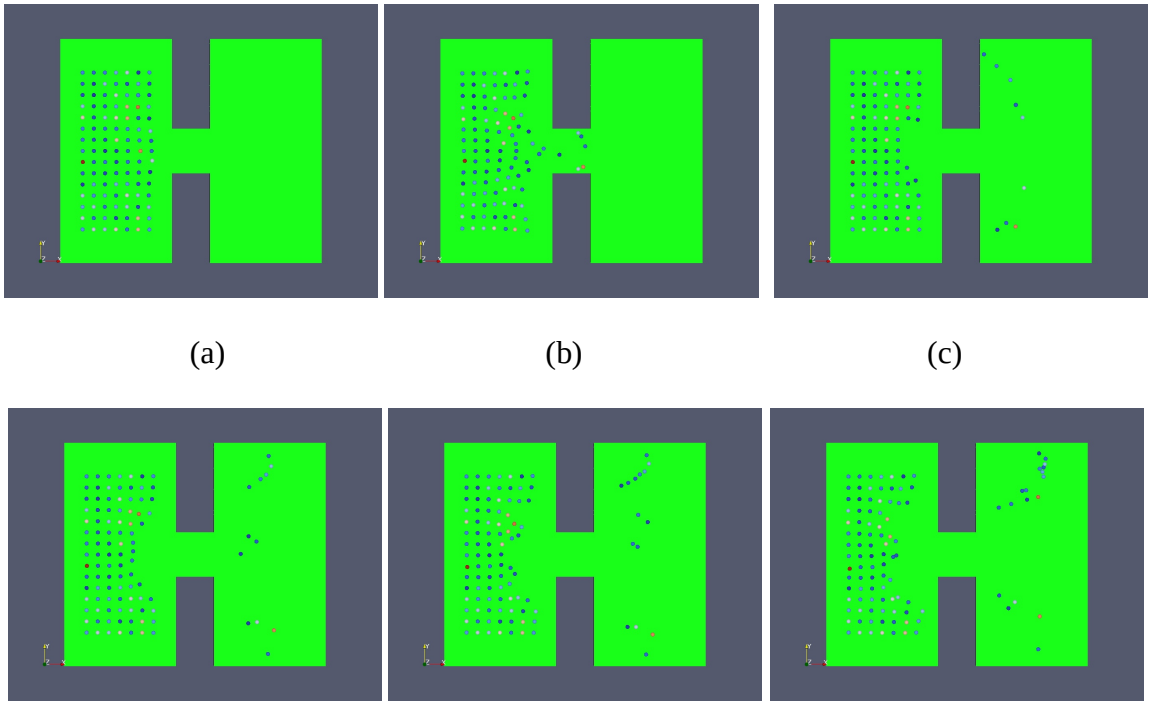

Figure 5.10. Snapshots from simulations of colloids that are far away from the entrance across a traveling wave membrane with surface electrodes at (a) t=0 s, (b) t=0.1ms, (c) t=0.5ms, (d) t=5ms, (e) t=10ms, (f) t=40 ms.

5.7. Modified Microfabrication Process

For the modified scheme of the traveling wave membranes with surface electrodes, the modified fabrication flow is shown in Figure 5.11. The assembly with two embedded electrodes and three insulator layers from the previous process was coated with chrome and gold. Then interdigitated electrodes were patterned on top of the chrome/gold electrode. The electrical resistance was measured to ensure that any electrode is not shorted to another. Then, aluminum was deposited on the patterned electrode, and patterned to form arrays of 3 µm diameter openings that aligned to the center of the interdigitated electrodes. The purpose

for the aluminum was to act as a mask in an ICP etching process after the photoresist was removed. After hardbaking, the assembly was then etched by a plasma etching with SF_6 5 sccm and O_2 50 sccm at 30 mTorr, 800W power supply. Images of fabricated membrane after etching through were shown in Figure 5.12.

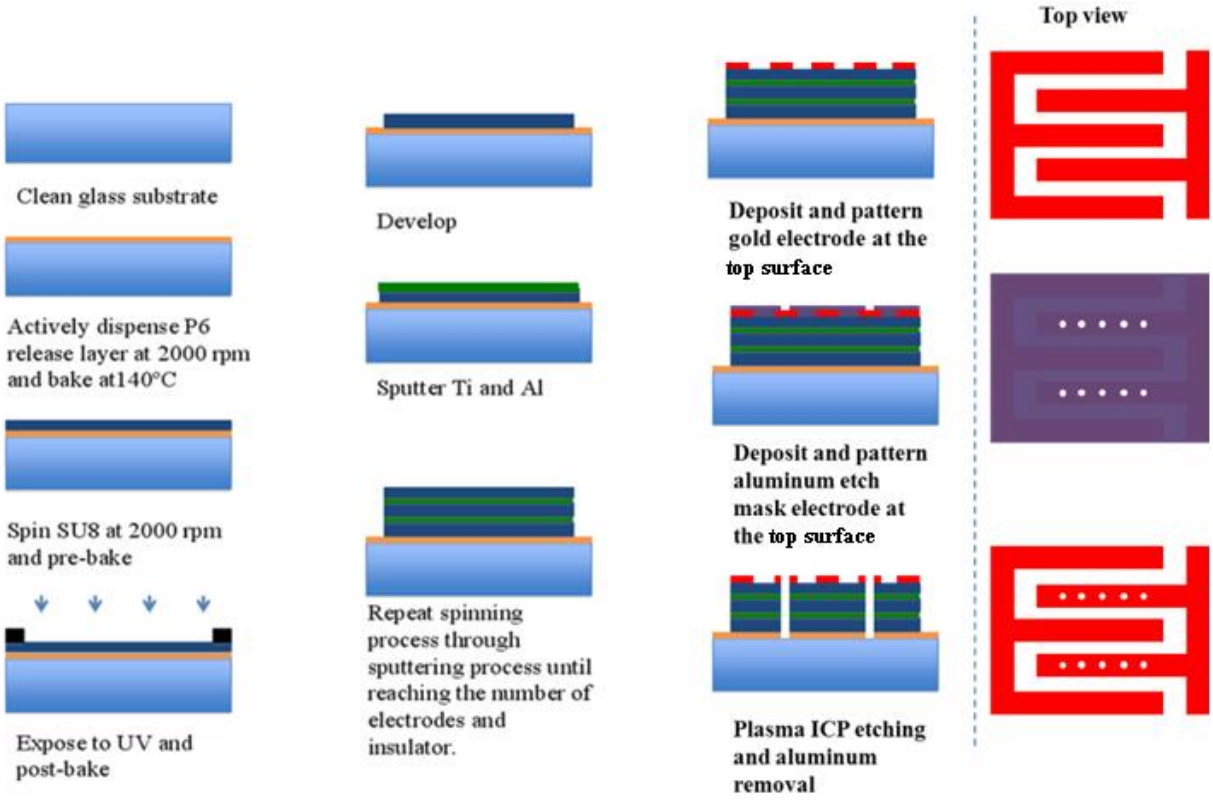

Figure 5.11. A microfabrication process for a traveling wave membrane with surface electrodes.

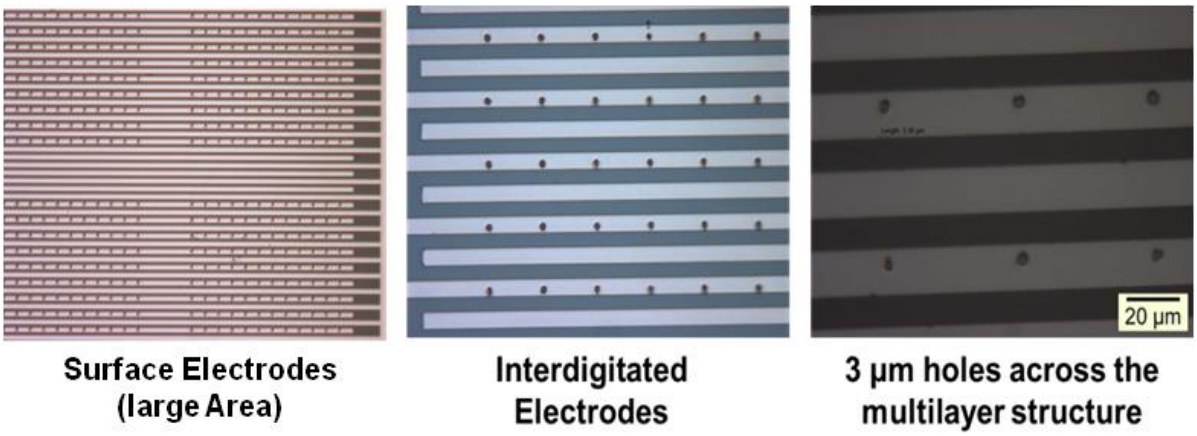

Figure 5.12. A fabricated membrane with surface electrodes.

An anti-stiction coating is also one of the main challenges to improve the membrane performance. Due to a high electric field at the edge of electrode, charged particles are probably concentrated at the maxima of the electric field. Previous work on anti-stiction coatings in microfluidic device were studied with many materials such as, poly(3,4, dihydroxyl-l-phenylalanine) or Poly(DOPA), polyethyleneglycol (PEG), polydopamine, poly vinylidene fluoride or PVDF, thiol, and Teflon coatings. For our testing, we examined a Teflon coating produced by an Inductively Coupled Plasma Reactive Ion Etcher (ICP-DRIE). The process is compatible with, and follows, the etching process in the previous section. After finishing the etching, the membrane was protected by photoresist in areas where no coated is desired. Then, the membrane was deposited with Teflon for 10 seconds and the photoresist was removed by photoresist stripper.

The traveling wave membrane was then transferred from the glass substrate to the top microchannel through an epoxy bonding and water release process. The device was then connected to flexible tubes for inlet/outlet by using a two-part-epoxy and ready for testing.

5.8. Results and Discussion

The experiment was set up with the same equipments as discussed previously. For the device with surface electrodes, similarly, nanoscale particles were shown to be concentrated at the pore exit when the traveling waveform voltages were supplied to the electrode as shown in Figure 5.13, although not all the microchannels demonstrated colloid transport in the previous sample. Another observation was along the membrane surface on the clean side, where we observed a line of colloids between the adjacent electrodes as shown in Figure 5.14. However, the colloids at these lines and microchannel holes were in a different plane and depth of focus in the microscope and we could not capture the behavior of colloidal transportation at both places at the same time. Also, after removing the traveling waveform voltage, particles would still stick to the membrane without orientations. Majority of them are at the end of the microchannel as shown in Figure 5.15. Hence, a better coating is required for this type of membrane. Moreover, after 3 minutes of supplied voltage at 2 V, the electrolysis of electrodes was observed as shown in Figure 5.16. This reaction greatly shortened the operating life of the device. Investigating the surface electrodes after the experiment also showed that the electrodes were partially etched away at this voltage.

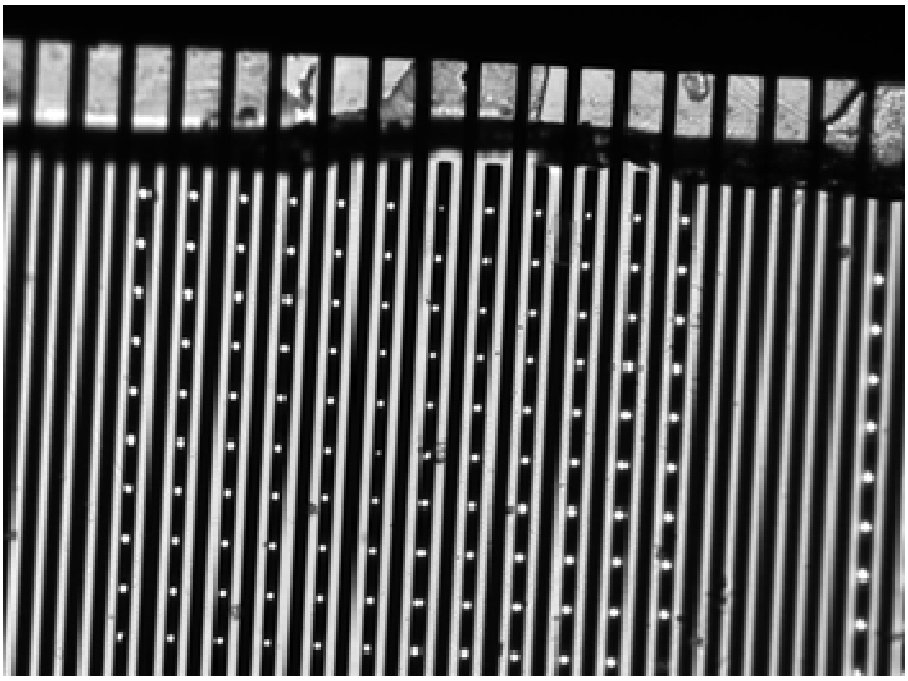

Figure 5.13. A tested membrane with an inverted fluorescent microscope

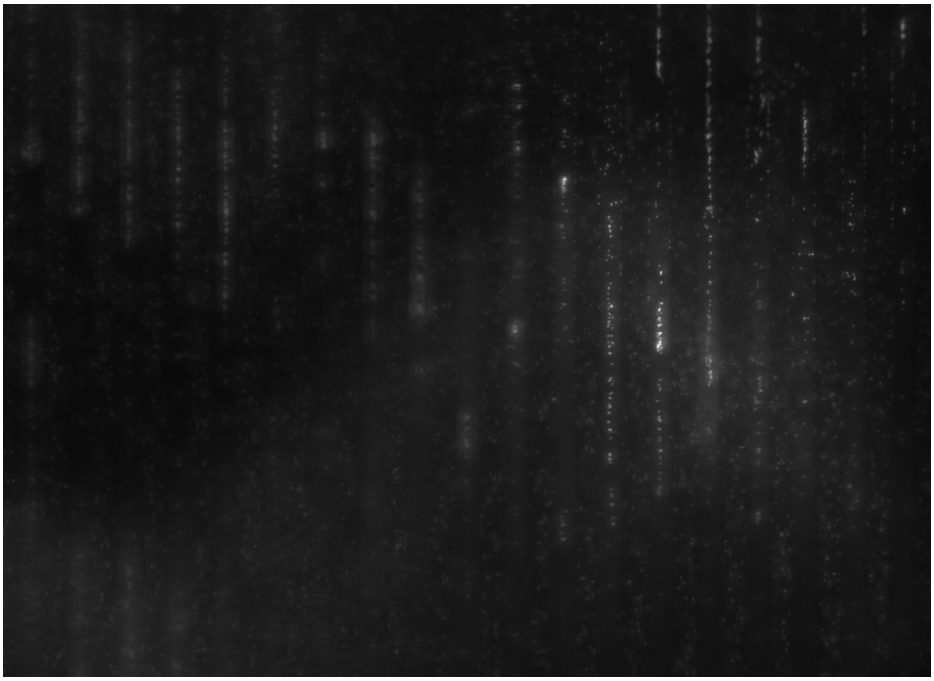

Figure 5.14. Nanoscale colloids are concentrated between two sets of surface electrodes

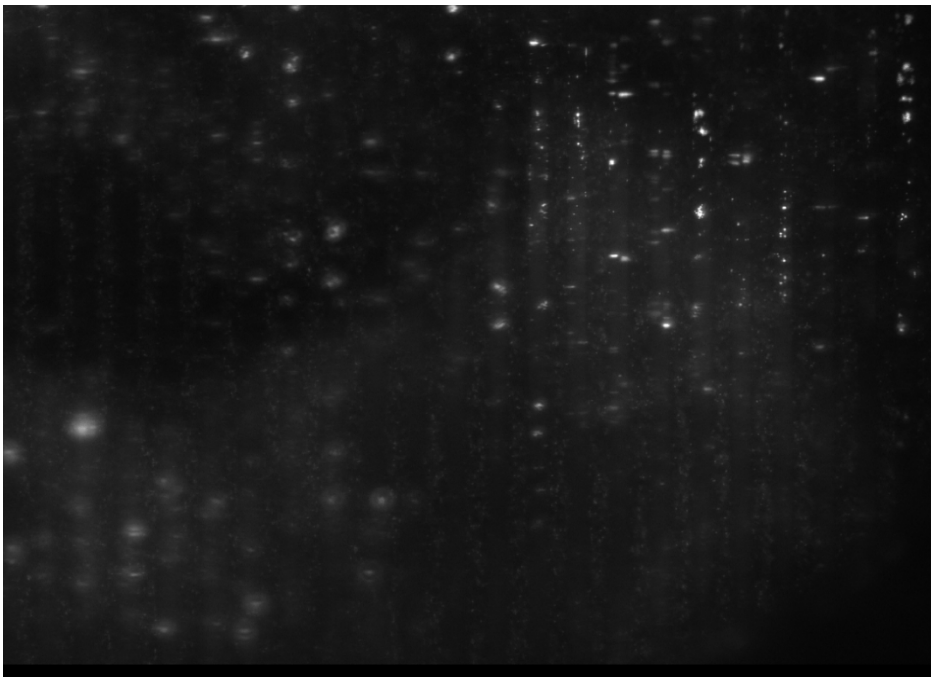

Figure 5.15. After the traveling waveform voltage is removed from the sidewall electrodes. Some of colloids tend to stick to the membrane.

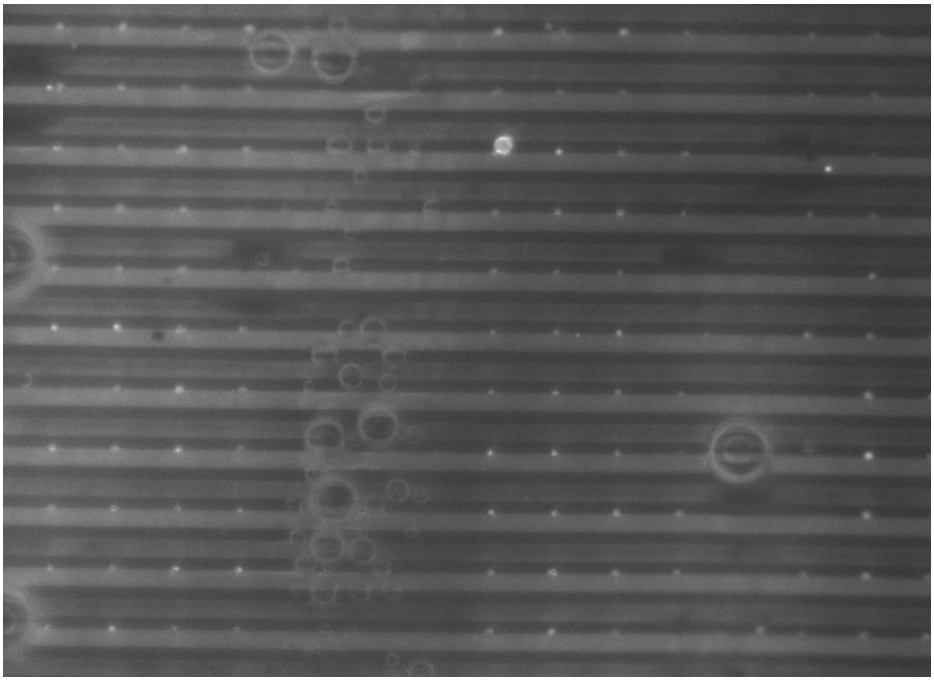

Figure 5.16. At a higher voltage (~2V), bubbles erupt in the system between sidewall electrode, due to an electrolysis reaction.

The value of colloidal transport efficiency is calculated by the ratio of the amount of colloids that are passed through the traveling wave membrane to the amount of colloids in the feed stream. By using the Image-Pro Plus® 5.1 software as a data recording and the ImageJ® software as an image processing, the normalized fluorescent intensity change of our membrane with surface electrodes for 93 nm colloids in water is about 20% with the surface electrodes as shown in Figure 5.17. Compared to the membrane without the surface electrodes (normalized fluorescent intensity is 2.5%), the removal efficiency is about an order of magnitude higher.

From simulations as shown in Figure 5.10, we also observed the particles at the entrance can be transported through the pore in a few milliseconds. However, the duration that particles travels inside the pore is slightly different from the simulation. It can take longer for some particles to get transferred across the pore. This could occur because of the confinement of the pore. Additionally, the movement of multiple particles in the system can be slightly different from a single particle due to a complexity of interactions between the particles. Furthermore, a diffusion model can be used to estimate the change of the colloid concentration in the chamber. The flux of the colloid in the chamber is mainly due to diffusion, which is given by Equation 5.10, where c is the concentration of the colloid, D is the diffusion coefficient of the colloid. The change of the colloid concentration is governed by Equation 5.11.

$$\Gamma = -D\nabla c \tag{5.10}$$

$$\frac{\partial c}{\partial t} = D\nabla^2 c \tag{5.11}$$

In the simulation, the flux at the microchamber wall is assumed to be zero. The flux at the exit of the chamber (the entrance of the pore) is calculated from Equation 5.12, where α is the percentage of the opening. In our experiment, the percentage of the opening is about 2%. From this calculation, we can calculate the change in concentration of particle across this traveling wave membrane. In comparison, the simulation with diffusion showed similar trend as shown in Figure 15, where a solid and dashed line for the performance of the traveling wave membrane with and without the voltage supplies.

$$\Gamma_o = u_p \alpha c \qquad (5.12)$$

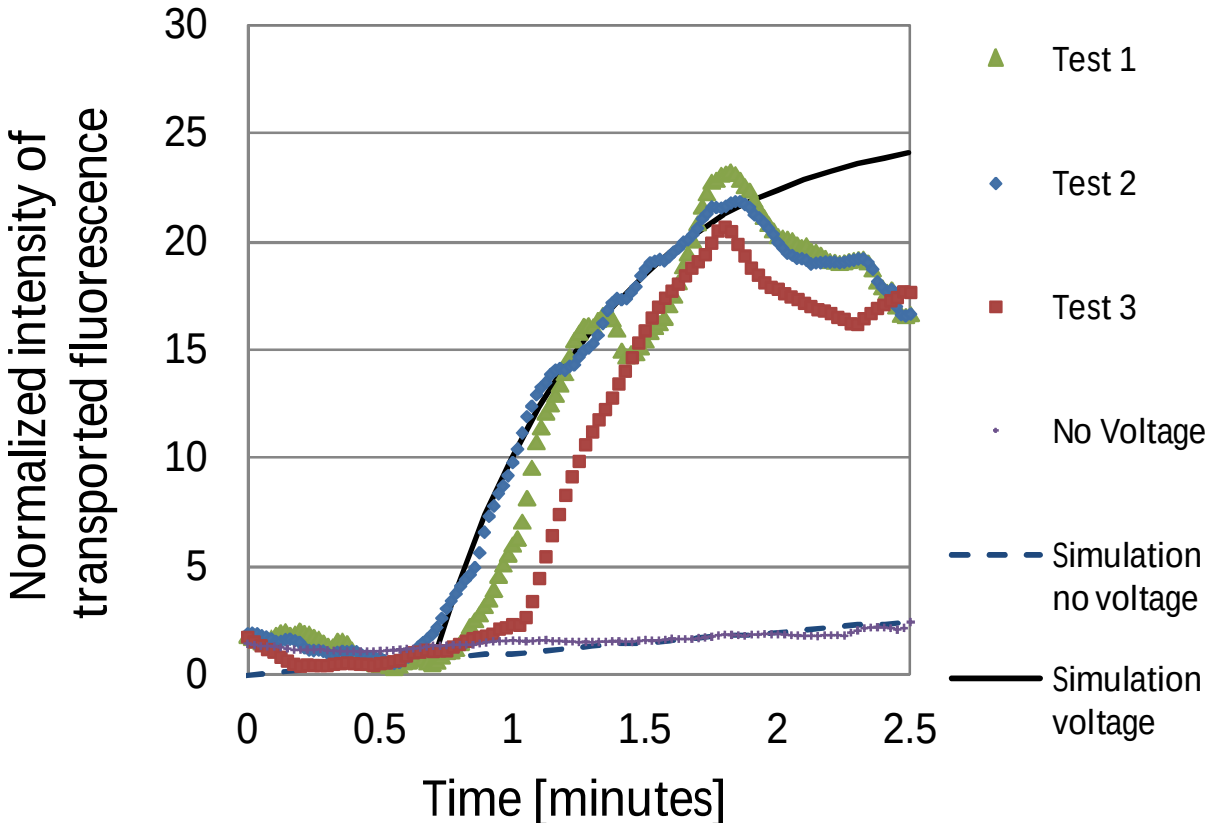

Figure 5.17. Relationship between percentage of particle removal and time in minute.

5.9. Future Work

The statement of work for this membrane includes the following development;

- **Developing technology for smaller particle separation and ion separation**

We will also expand the range of colloids to include a full range of colloidal substances found in water, from clays (silicoaluminates) to lipids and proteins. For different range of size and charge on the silica colloids, this membrane can be implemented and tested with the modified dimension. Also, frequency response of the colloids as a function of size and charge can be adjusted.

Another challenges for nanoscale transportation is for ion separation. Ionic liquid or electrolyte is small in size and has a wide range of concentration and components. Different ionic constitutes can be found in source water and sea water. Seawater has a high conductivity of 4.8 S/m and a relative permittivity of 35. Ultimately, at the end of the project, source waters with salinity and high SDI to determine will also conduct with this type of AC electrokinetics. In the process of desalination process, these ions are removed from the system. In the setup, the phosphate buffer saline can be used to examine for the behavior of ions with AC electrokinetics. Last, the ultimate goal is to test the traveling wave membrane with original sea water from different sources to investigate the performance of this membrane.

- **Developing fabrication techniques using nanochannel with charged sidewall for smaller colloids and ion separation**

With advantages of smaller dimension, higher electrical field can enhance the performance of colloidal separation. In literature, carbon nanotubes and grapheme are widely

studied for water transportation. Also, selective transportation of ion is different for each species across the small diameter of nanochennel created in the material.

With our specialists on fabrication of porous silicon membrane with a diameter of 3-5 nm, the scheme of AC signal can be used to investigate the ion and colloidal transportation across the membrane. Based on our previous work [58], we have implemented a technique of anodization to create nanochannels on silicon that can be implemented for the proton exchange membrane (PEM) for the micro fuel cell project as shown in Figure 5.18. Similarly, the same membrane can be fabricated with the coating of metal to the sidewall. First investigation is to coat this wall with conductively layer throughout the pore and sidewall. Then, the sidewall is supplied with AC traveling waveform voltage. This can result to the selectivity transportation of nanoscale colloids and ions. Next, the multi-layer of traveling waveform with electrical insulator can be designed to evaluate ion separation and colloids smaller than 100 nm in size for an ultimate result.

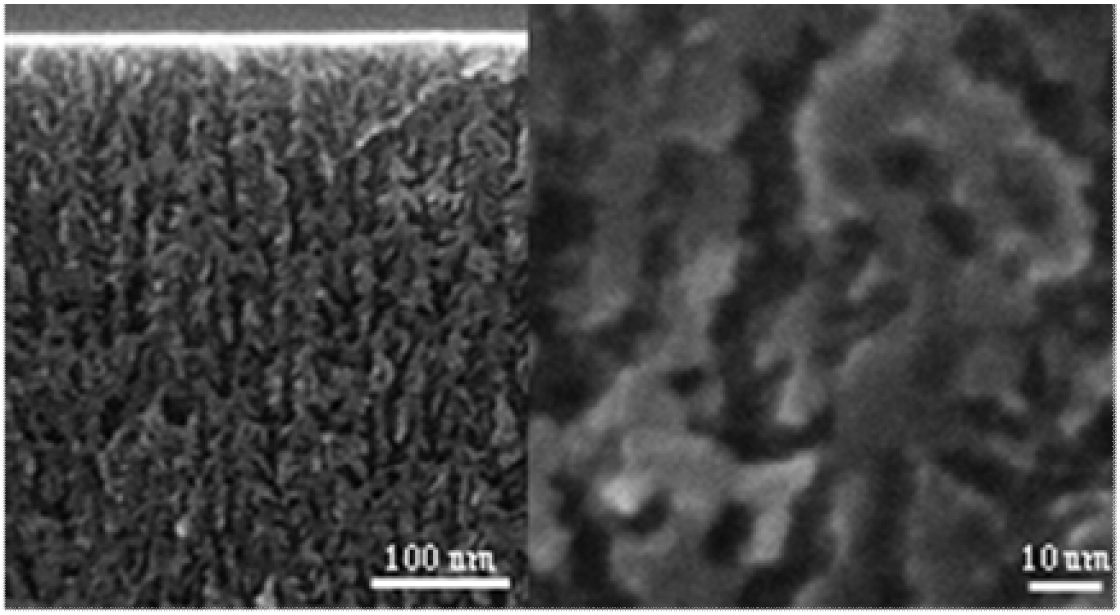

Figure 5.18. Cross-section of the porous silicon membrane fabricated by a HF anodization process that can be studied for colloidal separation with nanometer scale.

- **Developing suitable technique of colloidal and ion detection**

The current technique of fluorescent microscopy is only valid for the range of 100 nm colloids. There are some difficulty to focus on the depth of focus for the testing and inconsistent for the intensity of fluorescent illumination. The following techniques are outstanding and promising for detecting nanoscale colloids and ionic transportation.

i. Titration Techniques (Halide Determination)

One of the techniques for determining the concentration of halide is titration. In this method, the concentration of chlorine, bromine, and iodine are titrated to determine the concentration by detecting a total change in color. This analysis can be calculated for the amount of solution that used in the process. However, colored compounds can be difficult to work with as they obscure the end point and make the determination less precise.

ii. Ion-selective Electrodes

A certain type of ion-selective electrodes can be purchased with the analysis system. The electrode is specified and calibrated to detect a concentration of ion in a unit of part per million (ppm). The challenge of this method is the amount of solution that is required for testing and the total price of the entire system.

iii. Silt Density Index (SDI) Test

Although the values do not directly correlate to the fouling potential of a specific water, the Silt Density Index (SDI) test is considered to be an industry standard for measuring the colloidal fouling potential of spiral wound membranes. For SDI test results to be accurate, the feed line to the kit must be connected to the raw water line representative of the feedwater to the RO system. The major membrane manufacturers typically recommend maintaining an SDI value of 3.0 to 5.0 for feedwater to a reverse osmosis system. A typical SDI for surface waters is always greater than 6 and for a seawater desalination plants utilising reverse osmosis systems also need very efficient filtering due to the typically high but variable SDI of seawater.

- **Optimizing power consumption and external apparatus for the operating system of portable water purification device**

The final delivery of this project will be a set of design rules for AC electrokinetics permselective pumping of colloids. The target specification for the AC electrokinetics is for

purification of colloids for different ranges of diameter. In Phase I, optimize design and operation is to achieve 70% recovery of product water without colloidal substances greater than 100 nm in size. In the final device, the ultimate energy budget is expected to be <3 W/gph. The water recovery is up to 70% with an output flow rate of 10 gph. The water quality is consider at SDI <5 and salinity <1000 ppm TDS. Integrate permselective membranes in microchannel chamber can be also tested to separate colloids in a continuous streamwise operation and characterize performance. The range of operation time is upto 72 hours continuously. The ultimate goal is to build an integrated prototype system with a weight < 10 lbs and volume < 5 cubic feet for a portable water purification device.

- **Considering other applications of the membranes and transferring technologies into a commercial product**

Particularly in the chemical separation, this type of traveling wave membrane can induce transport of particle in liquid electrolyte. Examples of targeted applications include drug delivery system, gel chromatography, etc.

With adjustments on flow rate, AC voltage supply, AC frequency, medium conductivity, particle surface charge density, particle size, permittivity of medium, a separation process is optimized by a rejection rate of colloids. For example, particle conductivity will affect the values of Clausius-Mossotti function. Further investigation is to observe a motion of fluorescent particles in the testing assembly by using an inverted fluorescent microscope in future work. With this technique, a separation of 93 nm fluorescent latex colloids is expected for a better performance and removal efficiency. With these developments, the travelling wave membranes can be scaled and adjusted to benefit several

applications for separations of different colloids such as bio-particles, blood cells, viruses, proteins, and yeasts in further study. There are several challenges to build this device. Key challenges that need to be overcome to develop this type of membrane include

- To finalize the parameters (medium conductivity, particle conductivity, particle size, voltage supply, frequency, and number of electrodes) that are optimized for a transportation of colloids in microchannel.
- Understanding the adjustable parameter for colloidal transport, for example, zeta potential, Debye length, concentration, double layer, diffusion layer, Dunkhin number, surface conductance, etc. The structure can also be used to investigate nanoscale colloidal transportations and properties of particles
- Learning how to apply the traveling wave AC supply to the membrane in order to form a colloidal concentration and separation across the membrane
- Maximizing the amount of colloids collecting at the other end of microchannels
- Increasing the efficiency of separation associated with the fluidic motion
- Improving the design and electrical isolation
- Decreasing the volume of external devices required to operate this membrane
- Developing technology to compatible with commercial membrane.

5.10. Conclusion

In this study, we developed the techniques for the AC traveling wave membrane for subnanometer colloidal separation. With this technique, a separation of 93 nm fluorescent latex colloids was shown. A microfabrication process enables the development of this

membrane by using a thin film deposition, evaporation, and plasma etching to create a microfluidic path of 3 μm in diameter through the multi-layer of insulators and alternating electrodes. These fabricated membranes are connected to the traveling waveform generator with different phase that can induce a motion of colloids across the membrane. This type of traveling wave membrane can be scaled and adjusted for transport of particles in liquid electrolyte, particularly in the chemical separation. Examples of targeted applications include drug delivery system and gel chromatography.

Key properties of our MEMS-based traveling wave membrane include:

- Membrane structure with embedded electrodes,
- Biasing scheme to enhance the nanoscale colloidal separation,
- Three-dimensional structure of traveling wave membrane,
- Stationary coating layer for anti-stiction of charged particles,
- And, improving the efficiency of nanoscale separation.

5.11. References

[1] M. A. Shannon, "Water desalination: Fresh for less," *Nature Nanotechnology,* vol. 5, pp. 248-250, 2010.

[2] B. K. Gurtler, T. A. Vetter, E. M. Perdue, E. Ingall, J. F. Koprivnjak and P. H. Pfromm, "Combining reverse osmosis and pulsed electrical current electrodialysis for improved recovery of dissolved organic matter from seawater," *J. Membr. Sci.,* vol. 323, pp. 328-336, 2008.

[3] Q. Liu, C. C. Parrish and R. Helleur, "Lipid class and carbohydrate concentrations in marine colloids," *Mar. Chem.,* vol. 60, pp. 177-188, 1998.

[4] M. L. Wells and E. D. Goldberg, "Occurrence of small colloids in sea water," *Nature,* vol. 353, pp. 342-344, 1991.

[5] A. Yamasaki, H. Fukuda, R. Fukuda, T. Miyajima, T. Nagata, H. Ogawa and I. Koike, "Submicrometer particles in Northwest Pacific coastal environments: abundance, size distribution, and biological Origins," *Limnol. Oceanogr.,* vol. 43, pp. 536-542, May, 1998.

[6] P. M. Dove and C. M. Craven, "Surface charge density on silica in alkali and alkaline earth chloride electrolyte solutions," *Geochim. Cosmochim. Acta,* vol. 69, pp. 4963-4970, 2005.

[7] J. Voldman, "Electrical forces for microscale cell manipulation," *Annu. Rev. Biomed. Eng.,* vol. 8, pp. 425-454, 2006.

[8] O. Kuksenok, J. M. Yeomans and A. C. Balazs, "Creating localized mixing stations within microfluidic channel," *Langmuir,* vol. 17, pp. 7186-7190, 2001.

[9] M. P. Hughes, "AC electrokinetics: applications for nanotechnology," *Nanotechnology,* vol. 11, pp. 124, 2000.

[10] B. P. Lynch, A. M. Hilton, C. H. Doerge and G. J. Simpson, "Dielectrophoretic force microscopy of aqueous interfaces," *Langmuir,* vol. 21, pp. 1436-1440, 2005.

[11] A. Ramos, H. Morgan, N. G. Green and A. Castellanos, "Ac electrokinetics: a review of forces in microelectrode structures," *J. Phys. D,* vol. 31, pp. 2338, 1998.

[12] P. K. Wong, T. Wang, J. H. Deval and C. Ho, "Electrokinetics in micro devices for biotechnology applications," *IEEE/ASME Trans. Mechatronics,* vol. 9, pp. 366-376, 2004.

[13] N. G. Green, A. Ramos and H. Morgan, "Ac electrokinetics: a survey of sub-micrometre particle dynamics," *J. Phys. D,* vol. 33, pp. 632-641, 2000.

[14] U. Lei, C. W. Huang, J. Chen, C. Y. Yang, Y. J. Lo, A. Wo, C. F. Chen and T. W. Fung, "A travelling wave dielectrophoretic pump for blood delivery," *Lab-on-A-Chip,* vol. 9, pp. 1349-1356, 2009.

[15] S. Masuda, M. Washizu and I. Kawabata, "Movement of blood cells in liquid by nonuniform traveling field," *IEEE Trans. Ind. Appl.,* vol. 24, pp. 217-222, 1988.

[16] H. Morgan, N. G. Green, M. P. Hughes, W. Monaghan and T. C. Tan, "Large-area travelling-wave dielectrophoresis particle separator," *J Micromech Microengineering,* vol. 7, pp. 65, 1997.

[17] R. Hagedorn, G. Fuhr, T. Müller and J. Gimsa, "Traveling-wave dielectrophoresis of microparticles," *Electrophoresis,* vol. 13, pp. 49-54, 1992.

[18] Y. Huang, X. B. Wang, J. A. Tame and R. Pethig, "Electrokinetic behaviour of colloidal particles in travelling electric fields: studies using yeast cells," *J. Phys. D,* vol. 26, pp. 1528-1535, 1993.

[19] M. H. Lean, H. B. Hsieh and A. R. Volkel, "Particle simulation of traveling wave gel electrophoresis," *IEEE/EMBS Special Topic Conference on Microtechnology in Medicine and Biology,* pp. 356-359, 2005.

[20] N. G. Green and Morgan H., "Dielectrophoretic separation of nano-particles," *J. Phys. D,* vol. 30, pp. L41, 1997.

[21] N. G. Green and H. Morgan, "Dielectrophoretic investigations of sub-micrometre latex spheres," *J. Phys. D,* vol. 30, pp. 2626, 1997.

[22] F. F. Becker, X. B. Wang, Y. Huang, R. Pethig, J. Vykoukal and P. R. Gascoyne, "Separation of human breast cancer cells from blood by differential dielectric affinity," *Proceedings of the National Academy of Sciences,* vol. 92, pp. 860-864, 1995.

[23] X. B. Wang, Y. Huang, F. F. Becker and P. R. C. Gascoyne, "A unified theory of dielectrophoresis and travelling wave dielectrophoresis," *J. Phys. D,* vol. 27, pp. 1571, 1994.

[24] H. Morgan, A. G. Izquierdo, D. J. Bakewell, N. G. Green and A. Ramos, "The dielectrophoretic and travelling wave forces generated by interdigitated electrode arrays: analytical solution using Fourier series," *J. Phys. D,* vol. 34, pp. 1553-1561, 2001.

[25] N. G. Green, A. Ramos and H. Morgan, "Numerical solution of the dielectrophoretic and travelling wave forces for interdigitated electrode arrays using the finite element method," *J. Electrostatics,* vol. 56, pp. 235-254, 2002.

[26] H. Du, W. H. Li, D. F. Chen and C. Shu, "Manipulation of bioparticles using traveling wave dielectrophoresis: numerical approach," *Intl. J. Mechanics and Materials in Design,* vol. 1, pp. 115-130, 2004.

[27] M. Urdaneta and E. Smela, "Multiple frequency dielectrophoresis," *Electrophoresis,* vol. 28, pp. 3145-3155, 2007.

[28] N. G. Green and H. Morgan, "Dielectrophoresis of submicrometer latex spheres. 1. experimental results," *J. Phys. Chem. B,* vol. 103, pp. 41-50, 1999.

[29] P. R. C. Gascoyne and J. V. Vykoukal, "Dielectrophoresis-based sample handling in general-purpose programmable diagnostic instruments," *Proceedings of the IEEE,* vol. 92, pp. 22-42, 2004.

[30] P. R. C. Gascoyne and J. Vykoukal, "Particle separation by dielectrophoresis," *Electrophoresis,* vol. 23, pp. 1973-1983, 2002.

[31] A. Ramos, H. Morgan, N. G. Green, A. Gonzalez and A. Castellanos, "Pumping of liquids with traveling-wave electroosmosis," *J. Appl. Phys.,* vol. 97, pp. 084906, 2005.

[32] A. Ramos, A. González, P. García-Sánchez and A. Castellanos, "A linear analysis of the effect of Faradaic currents on traveling-wave electroosmosis," *J. Colloid Interface Sci.,* vol. 309, pp. 323-331, 2007.

[33] L. Olesen, H. Bruus and A. Ajdari, "ac electrokinetic micropumps: the effect of geometrical confinement, Faradaic current injection, and nonlinear surface capacitance," *Phys. Rev. E,* vol. 73, pp. 056313, 2006.

[34] M. L. Y. Sin, V. Gau, J. C. Liao, D. A. Haake and P. K. Wong, "Active manipulation of quantum dots using AC electrokinetics," *J. Phys. Chem. C,* vol. 113, pp. 6561-6565, 2009.

[35] B. P. Cahill, L. J. Heyderman, J. Gobrecht and A. Stemmer, "Electro-osmotic streaming on application of traveling-wave electric fields," *Phys. Rev. E,* vol. 70, pp. 036305, 2004.

[36] M. Mpholo, C. G. Smith and A. B. D. Brown, "Low voltage plug flow pumping using anisotropic electrode arrays," *Sensors Actuators B: Chem.,* vol. 92, pp. 262-268, 2003.

[37] A. Ajdari, "Pumping liquids using asymmetric electrode arrays," *Phys. Rev. E,* vol. 61, pp. R48, 2000.

[38] V. Studer, A. Pepin, Y. Chen and A. Ajdari, "An integrated AC electrokinetic pump in a microfluidic loop for fast and tunable flow control," *Analyst,* vol. 29, pp. 944-949, 2004.

[39] J. Urbanski, T. Thorsen, J. Levitan and M. Bazant, "Fast ac electro-osmotic micropumps with nonplanar electrodes," *Appl. Phys. Lett.,* vol. 89, pp. 143508, 2006.

[40] M. M. Gregersen, L. H. Olesen, A. Brask, M. F. Hansen and H. Bruus, "Flow reversal at low voltage and low frequency in a microfabricated ac electrokinetic pump," *Phys. Rev. E,* vol. 76, pp. 056305, 2007.

[41] B. Storey, M. Kilic and M. Bazant, "Steric effects on ac electro-osmosis in diluted electrolytes," *Phys. Rev. E,* vol. 77, pp. 036317, 2008.

[42] P. Garcia-Sanchez, A. Ramos, N. G. Green and H. Morgan, "Traveling-wave electrokinetic micropumps: velocity, electrical current, and impedance measurements," *Langmuir,* vol. 24, pp. 9361-9369, 2008.

[43] P. Garcia-Sanchez, A. Ramos, N. G. Green and H. Morgan, "Experiments on AC electrokinetic pumping of liquids using arrays of microelectrodes," *IEEE Trans. Dielectr. Electr. Insul.,* vol. 13, pp. 670-677, 2006.

[44] I. Ermolina and H. Morgan, "The electrokinetic properties of latex particles: comparison of electrophoresis and dielectrophoresis," *J. Colloid Interface Sci.,* vol. 285, pp. 419-428, 2005.

[45] R. W. O'Brien and L. R. White, "Electrophoretic mobility of a spherical colloidal particle," *J. Chem. Soc. , Faraday Trans. 2,* vol. 74, pp. 1607-1626, 1978.

[46] J. Lyklema and M. Minor, "On surface conduction and its role in electrokinetics," *Colloids Surf. Physicochem. Eng. Aspects,* vol. 140, pp. 33-41, 1998.

[47] C. Grosse, S. Pedrosa and V. N. Shilov, "On the influence of size, ζ potential, and state of motion of dispersed particles on the conductivity of a colloidal suspension," *J. Colloid Interface Sci.,* vol. 251, pp. 304-310, 2002.

[48] C. Grosse, S. Pedrosa and V. N. Shilov, "Corrected results for the influence of size, ζ potential, and state of motion of dispersed particles on the conductivity of a colloidal suspension," *J. Colloid Interface Sci.,* vol. 265, pp. 197-201, 2003.

[49] M. Rasmusson and S. Wall, "Surface electrical properties of polystyrene latex: 1. electrophoresis and static conductivity," *J. Colloid Interface Sci.,* vol. 209, pp. 312-326, 1999.

[50] Somasundaran P, Ed., *Encyclopedia of Surface and Colloid Science.* Boca Raton, FL: CRC Press, Taylor & Francis Group, 2006.

[51] E. R. Parker, B. J. Thibeault, M. F. Aimi, M. P. Rao and N. C. MacDonald, "Inductively coupled plasma etching of bulk titanium for MEMS applications," *J. Electrochem. Soc,* vol. 152, pp. C675-C683, 2005.

[52] B. R. Flachsbart, K. Wong, J. M. Iannacone, E. N. Abante, R. L. Vlach, P. A. Rauchfuss, P. W. Bohn, J. V. Sweedler and M. A. Shannon, "Design and fabrication of a multilayered polymer microfluidic chip with nanofluidic interconnects via adhesive contact printing," *Lab-on-A-Chip,* vol. 6, pp. 667-674, 2006.

[53] N. G. Green, A. Ramos, A. Gonzalez, H. Morgan and A. Castellanos, "Fluid flow induced by nonuniform ac electric fields in electrolytes on microelectrodes. I. Experimental measurements," *Phys. Rev. E,* vol. 61, pp. 4011-4018, 2000.

[54] N. G. Green, A. Ramos, A. Gonzalez, H. Morgan and A. Castellanos, "Fluid flow induced by nonuniform ac electric fields in electrolytes on microelectrodes. III. Observation of streamlines and numerical simulation," *Phys. Rev. E,* vol. 66, pp. 026305, 2002.

[55] M. Z. Bazant, M. S. Kilic, B. D. Storey and A. Ajdari, "Towards an understanding of induced-charge electrokinetics at large applied voltages in concentrated solutions," *Adv. Colloid Interface Sci.,* vol. 152, pp. 48-88, 2009.

[56] M. Z. Bazant and T. M. Squires, "Induced-charge electrokinetic phenomena," *Current Opinion in Colloid & Interface Science,* vol. 15, pp. 203-213, 6, 2010.

[57] A. Ramos, H. Morgan, N. G. Green and A. Castellanos, "AC electric-field-induced fluid flow in microelectrodes," *J. Colloid Interface Sci.,* vol. 217, pp. 420-422, 1999.

[58] S. Moghaddam, E. Pengwang, Y. Jiang, A. R. Garcia, D. J. Burnett, C. J. Brinker, R. I. Masel and M. A. Shannon, "An inorganic-organic proton exchange membrane for fuel cells with a controlled nanoscale pore structure," *Nature Nanotechnology*, vol. 5, pp. 230-236, 2010.

CHAPTER 6:

CONCLUSION

6.1. Summary of Work

In chapter 2, development of micro fuel cells is reported. The enabling technology for this work is to combine hydrogen generator by hydrolysis reaction, control valve for fuel delivery system, and membrane electrode assembly. Development of a millimeter-scale fuel cell with on-board fuel and a passive control mechanism is presented in this study. Fabrication of this unique power source is enabled through development of a new self-regulating micro-hydrogen generator. This design of power source has a total volume of 9 μL, which makes it the smallest fully integrated fuel cell reported in the literature. This power sources can operate only when the hydrogen is required and stop when it is not working, manipulated by deflecting of membrane. By this mean, metal hydride can react with water vapor to generate hydrogen. When hydrogen contact to the membrane electrode assembly, the current can be draw from the circuit. As a result, the device can deliver an energy density of ~244-280 Wh/L. The ability to store/deliver power with high energy densities in this millimeter-scale power source can enable a new class of MEMS devices.

In chapter 3, improvements on hydride-based micro fuel cell with on-board hydrogen source continue from the first generation. Microfluidic paths are modified for different diameters and gaps between the polyimide membranes and the bottom of the water reservoir. Hydrogen generation rate of 0.44 μL s^{-1} with five rows of opening windows with 30 μm diameter and the height of 40 μm. With this design, we reported an increase of a power

density of 10 WL^{-1} to a power density of 97 WL^{-1}. The devices' energy density with $LiAlH_4$ is 263 WhL^{-1}. Another development is to implement a metal seal layer for storage of metal hydride and water in the device. The assembly was kept for more than 14 days for a designed layer of copper/silver/copper with a thickness of 80 nm/80 nm/200 nm. After dissolving the seal layer at 0.8 V for 3 minutes, the device operates without any loss in energy density. It deliver the overall energy density of 280 WhL^{-1}.

Ideally, availability of a robust inexpensive MEA that does not require conditioning can significantly expand the use of fuel cells. We present a silicon-based PEM with several advantages over Nafion (the best performing PEM in hydrogen fuel cells), in terms of higher and nearly humidity-independent proton conductivity, lack of volumetric size change with changes in temperature and humidity, higher temperature stability, and facility of MEA construction and silicon process integration to enable use for powering many microsystems and portable electronics. The key to achieving these Si-PEM advantages over Nafion is fabricating ~5 nm diameter relatively straight pores uniformly within a 25 microns thick silicon membrane and to self-assemble functional molecules on the pores' wall. We then constructed an approximately 2 nm thick silica layer on both sides of the membrane using plasma-defined atomic layer deposition (PD-ALD) to transition to smaller pore size at the finished surfaces of the membrane in order to maintain pore hydration at low humidity. The membrane maintains its proton conductivity at humidity levels down to 10-20%. A MEA constructed using the developed PEM delivered 332 W/cm^2 peak-power density (an order of magnitude higher than the previous reports) with dry hydrogen feed and air breathing cathode at room temperature. These fabricated membranes, their characterizations, and performances are presented in Chapter 4.

In chapter 5, the development in alternating current electrodialysis (ACED) is proposed for the colloidal separation in water purification process. This membrane occupies multiple traveling electrodes that are connected to different phase of AC voltage. The preliminary testing results also show a concentration of 93 nm colloids across the traveling wave membrane. With further investigation and simulations on different schemes, this type of membrane can be further scaled and investigated to manipulate nanoscale particles and ions.

6.2. Future Work

Microsystems, microfluidic devices, and MEMS can be enhanced by development in membrane technology. Applications of membranes are widely broad for the development of micro and nanotechnology. In general, different membranes are suitable for different applications. However, fundamentals of microfabrication processes are expandable for microsystems at different scales.